University of Milano–Bicocca
Department of Earth and Environmental Sciences
Doctoral School of Environmental Science – XXVIII cycle

ATMOSPHERIC AEROSOLS PHASE TRANSITIONS:

MEASUREMENTS AND IMPLICATIONS

Luca D'Angelo

Dissertation submitted for the degree of Philosophiæ Doctor (Ph.D.)

Supervisor: Prof. Ezio Bolzacchini

February, 2016

This work was supported by Fratelli Confalonieri Foundation, which provided a scholarship to the author.

"Dico, l'azzurro in che si mostra l'aria, non essere suo proprio colore, ma è causato da umidità calda, vaporata in minutissimi e insensibili atomi, la quale piglia dopo sé la percussion de'raggi solari e fassi luminosa sotto la oscurità delle immense tenebre della regione del fuoco, che di sopra le fa coperchio."

"I say that the blue showed in the air cannot be its own color but it is caused by the warm moisture evaporated in minute and insensible atoms, which catches the solar rays fall and becomes bright under the infinite darkness of the fire region, which acts as cover".

Leonardo da Vinci (1452 – 1519 *A.D.*)

ABSTRACT

The hygroscopicity is one of the main investigated properties of atmospheric aerosols. A number of works demonstrated that this property has a role in clouds formation, Earth's radiation budget, atmospheric visibility and multiphase chemistry. The ability of atmospheric aerosols to adsorb and absorb water is strictly linked to their physical state. Once they are directly emitted or formed from gaseous precursors, aerosols experience a variety of aging processes and different air thermodynamic conditions. When the relative humidity (RH) of the surrounding air increases, deliquescence can occur and the water-soluble fraction of the aerosol particle changes its phase from solid to liquid. On the contrary, a decrease in RH can lead to the reverse process, i.e. crystallization.

These two transitions affect a number of processes. The aim of this work is to investigate the implications of the aerosols physical states. Although many methods were developed in order to infer them, most of the authors focus on the phase transitions of simplified aerosol systems, such as pure compounds or simple mixtures, in order to improve available models but still neglecting the real ones which are extremely complex in chemical composition. In addition, the available techniques allow to investigate single aerosol particles or narrow size ranges. This leads to a loss of information about their overall behavior.

For this purpose, in this work an improved method based on the conductive properties of real atmospheric aerosol particles – collected as $PM_{2.5}$ fraction in Milan (Po Valley, Italy) – allows the identification of the RH at which deliquescence and crystallization occur. Since no other method was able to provide similar information on real samples, a gravimetric method was used as comparison and to estimate the growth factor due to water uptake.

The most interesting result is the observed hysteresis which characterize the phase transitions: deliquescence occurs at higher RH with respect to the crystallization and a variability in RH average seasonal values of both these processes is identified and explained according to the chemical composition of the studied system.

Three chapters of this work are dedicated to show the implications of the aerosols physical states and their hysteresis. It is demonstrated that a wrong parameterization of the hygroscopic growth factor leads to substantial errors in remote sensing data retrieval – such as particle concentrations within the planet boundary layer – and in a further wrong parameterization of the most common parameters used in cultural heritage risk assessment.

Moreover, a study of the effects of aerosol contaminations on electronic circuits is described highlighting that corrosion and electrochemical migration of conductive metals occur far below the water condensation conditions and the influences of surrounding air temperature and RH changing rate are pointed out. These effects give the reason to take into account the corrosive

role of aerosols in the air cooling systems design, especially in data centers where energy saving by external air forced convection and corrosion prevention are needed.

CONTENTS

INDEX OF FIGURES

INDEX OF TABLES

LIST OF ABBREVIATIONS

In this work some acronyms were used. Here, the main are reported.

AEC	aerosol exposure chamber
AN	ammonium nitrate
AS	ammonium sulfate
CRH	crystallization relative humidity
DFC	direct-free cooling
DRH	deliquescence relative humidity
E-AIM	Extended-Aerosol Inorganic Model
ECM	electrochemical migration
FA	fall
GDC-ENI	ENI (Italian oil and gas company) Green Data Center
IC	ion chromatography
IT	information technology
PCB/PCBA	printed circuit board/ PCB assembly
PM	particulate matter
PTFE	poly-tetra-fluoro-ethylene
PUE	power usage effectiveness
RH	relative humidity
ROTOR	rotating impactor
SIR	surface insulation resistance
SP	spring
SU	summer
T	temperature
WI	winter
WS	water-soluble

CHAPTER I – INTRODUCTION

In this chapter a brief overview of the phase transition processes of water-soluble compounds forming atmospheric aerosols is given. Firstly, an introduction elucidates the main characteristic of atmospheric aerosols including their sizes (Sect. 1.1) and chemical composition (Sect. 1.2). Then, the aerosols phase transitions are defined according to the scope of this work (Sect 2) and a brief overview of the main models (Sect. 3) and the measurement techniques (Sect. 4) are then presented.

SECTION 1 – THE ATMOSPHERIC AEROSOLS

1.1 Definition and sizes

The term *aerosol* is commonly associated to the ancient Greek word for *hydrosol* (i.e. water suspension) to identify a suspension of particles in a liquid media. *Aerosol* refers to an assembly of liquid or solid particles suspended in a gaseous medium long enough to be observed or measured[1]. Commonly, in aerosol science the term *aerosol* can be substitute by *atmospheric particles* or *particulate matter* (PM). Seinfeld and Pandis (2006)[2] highlighted the importance in defining an aerosol particle as a single continuous unit of solid or liquid matter which is formed by many molecules held together by intermolecular forces; in addition, a single particle can consists of many of this unit structures kept together by interparticle adhesive forces.

The size range of atmospheric particles spans from very few nanometers (ultrafine mode or nucleation mode, i.e. 3-20 nm)[3] to coarse mode (larger than tens of micrometers up to several hundreds of micrometers). Whereas many orders of magnitude differentiate ultrafine from coarse particles, the majority of the works is focused on the investigation of the properties of the fine and ultrafine particles, both because of their very different concentration within the troposphere (from ten to several thousand per cm^3 for particles smaller than 1 μm and less than 1 particle cm^{-3} for particles larger than 1 μm) and because of the much more relevant effects of smaller particles on many field of interest such as health[4,5] and climate forcing[6].

Atmospheric aerosols size distribution can be roughly divided in four modes. The smallest mode, *nucleation mode*, is due to aerosol particles formed from condensation of gaseous species and their nucleation processes to form new particles. Numerically, aerosols forming nucleation mode and Aitken nuclei mode (20-90 nm)[3] are much more than the other particles but, due to their small size, they contribute to the aerosols mass very little[2]. Once they are formed, these particles are lost since they easily aggregate or coalesce on bigger particles. The *accumulation mode* is due to particles typically sized from 90-100 nm to 2.5 μm and can be originated both directly by different sources and due to atmospheric reactivity between aerosols, moisture or gaseous species already present in the atmosphere (i.e. secondary origin). The name of this mode

is due to the fact that such sized aerosols have a longer residence time in the atmosphere than the other modes, since the removal mechanisms (wet and dry) are less efficient for them and this causes their accumulation. On the contrary, the *coarse mode* is constituted by large particles which are removed by settling mechanisms and they are easily removed from rainfall. They are mostly formed by mechanical processes such as soil erosion, abrasion, resuspension, sea-spray and other natural sources.

1.2 Aerosols chemical composition

The chemical composition of aerosols is strongly affected by the meteorological conditions and by both natural and anthropological sources which directly emit particles (primary particles) or gaseous precursors. Once in the atmosphere, these chemicals can react and generates new particles or change their chemical compositions. In the latter cases, these particles are usually termed *secondary*.

For example, many common gaseous species, such as NO_2 can solubilize in an aqueous droplet:

$$2NO_{2(g)} + H_2O \rightarrow HNO_{2(g)} + HNO_{3(g)}$$

Nitric acid can react with ammonia, forming ammonium nitrate (AN), one of the most widespread inorganic ionic compounds in the fine fraction of atmospheric aerosols:

$$HNO_{3(g)} + NH_{3(g)} \rightarrow NH_4NO_{3(s)}$$

A similar path is followed by gaseous SO_2 that can first undergo oxidation and form sulfuric acid, then it can easily react with ammonia leads to ammonium sulfate (AS):

$$H_2SO_{4(g)} + 2NH_{3(g)} \rightarrow (NH_4)_2SO_{4(s)}$$

Therefore, AN and AS are both mainly secondary aerosols and they are among the most abundant contributing species of the fine fraction mass. Measurements of $PM_{2.5}$ fraction, especially in urban ambient, stated that their mass percentage can represents up to about 40% of the total mass[7].

Atmospheric aerosols contain thousands of different chemical species. The most widespread and more important species (in term of mass fraction) are sulfates, nitrates and ammonium. On the other hand, the inorganic fraction only can be formed by a variety of chemical species and elements depending on its source. For example, *dust* fraction is crustal material constituted by Al, Si, Ca, Ti, Mg, Fe, Na, Sc and K, while *road dust* and resuspension matter can also present Cu, Pb, Cr, Co, Cd and V[8]. Sea-spray contains Cl^-, Na^+, K^+, Mg^{2+} and SO_4^{2-}, in addition to many organic compounds (and other inorganic species)[9,10].

As it was highlighted by Jacobson and co-authors (2000)[11] a complete inventory of the carbonaceous compounds forming the aerosols was never carried out, since they can cover a wide range of chemical species. One of the most abundant is elemental carbon, i.e. amorphous or graphitic carbon, mainly produced in combustions processes. The discussion about definitions and differences among *elemental carbon, black carbon, soot* and *soot carbon* in Andreae et al.

(2006)[12], demonstrates that carbonaceous aerosols are a very active topic. Organic compounds include low molecular weight hydrocarbons, carboxylic acids, amines, polycyclic aromatics, humic-like substances, biopolymers, etc. For for organic compounds as well, the presence and the relative abundance of each compounds is strongly affected by the source of atmospheric aerosols or their precursors. For example, amines are emitted by many processes, both anthropic and natural. Their importance in atmospheric chemistry is due to the fact that amines are the only organic species able to neutralize aerosols acidity[13]. Ammonia, methyl-amine, diethyl-amine and trimethyl-amine are often emitted by vegetation; other sources are fish processing, tobacco smoke, bacteria culture, incinerator, waste and sewage, biomass burning, automobiles, animal husbandry.

It is therefore obvious that atmospheric aerosols chemical composition changes in space both horizontally, since different sources characterized different sampling sites[14–18], and vertically due to aging processes and distance from direct sources. In addition, the contribution of the same sources are not constant in time and the chemical reactivity can change due to different meteorological and climatic conditions[19,20]. An example of aerosols chemical variability is showed by Perrone et al. (2012)[21], who characterized the fine fraction ($PM_{2.5}$) in three different site in the North of Italy: Milan (urban), Oasi Le Bine (rural) and Alpe San Colombano (remote) during winter (WI) and summer (SU) seasons. $PM_{2.5}$ fraction is constituted by aerosols with an aerodynamic equivalent diameter (equivalent to the diameter of a spherical particle with density of 1 g cm^{-3} and with the same settling velocity) below the threshold of 2.5 μm, collected with an efficiency of 48% (for particles with diameter of 2.5 μm). The importance of this fraction is due to the fact that within polluted atmospheres, it represents the most abundant contributor to aerosols mass. In addition, this fine fraction is able to deeply penetrate into the respiratory tract[22]. Perrone et al. (2012)[21] stated that elemental carbon accounted for 15.1% (weight/weight) and 10.9% in Milan during SU and WI, respectively, and decreased to 4.9% (SU) and 3.1% (WI) for the rural site and to 1.8% (SU) and 1.4% (WI) for a remote site. Conversely, the reactivity of aerosols led to a more oxidized states of the organic compounds in remote sites if compared to urban sites. In addition, whereas at Alpe San Colombano site (2280 m a.g.l.) sulfate fraction was seen to represent the major components of the inorganic fraction both during WI and SU, in Milan and Oasi Le Bine (located in the Po Valley) the prevalence of sulfate ions was recorded only during SU seasons while in WI nitrates prevailed. This is due to the fact that Alpe San Colombano site is above the mixing layer all year long and it is less influenced by NO_x reactivity, strongly emitted by combustion sources. On the contrary, wintertime meteorological conditions in the Po Valley leads to stagnant conditions of the mixing layer, that is the layer in which aerosols are diluted due to air convection. The absence of wind, low precipitations and very low mixing height[23] lead to high PM concentrations and high amount of nitrate ions in the fine fraction.

SECTION 2 – THE HYGROSCOPIC BEHAVIOR OF AEROSOLS

Within the atmosphere water can be present in gaseous phase as moisture, liquid when forming clouds droplets, fogs, rain and when it is condensed in aqueous aerosols, or in solid state as ice cirrus clouds, for example. The maximum content of water vapor in an air volume is termed as saturated vapor pressure and it is T-dependent.

A very important parameter in aerosol science is the saturation ratio of water in an air volume. In other word, the *relative humidity* (RH):

$$RH = \frac{p_w}{p_w^*(T)}\% \qquad \textit{(Eq. 1.1)}$$

where p_w and p_w^* are the partial pressure and saturated vapor pressure of water vapor, respectively.

Many atmospheric processes strongly depend on the presence and on the concentration of water in the atmosphere. The chemical reactivity of atmospheric aerosols is mainly affected by the presence of water within the atmosphere since many reactions can occur or they are more efficient in the aqueous phase (acid-base reactions, redox, etc.). In this regards, Kuwata and Martin (2012)[24] observed that at low RH conditions the uptake of ammonia by solid and semisolid adipic acid is negligible whereas it increases at high RH, when an aqueous phase is present.

Moreover, it is a matter of fact that moisture affects the optical properties of aerosols. This is due to the fact that when air moisture is adsorbed to an aerosol particle it increases its size and changes its refractive index, which is a complex number that describes the light scattering (real part) and the absorption (imaginary part) efficiencies of a compound. For example, Michel Flores and co-authors (2012)[25] measured the refractive index of a particle composed by AS and nigrosine (1:1 molar ratio) in dry condition (RH<3%) and at 80% RH. They found that both scattering and absorption efficiencies decreased at high RH (1.595+i0.154 and 1.469+i0.073, respectively).

The capability of atmospheric aerosols to uptake air moisture is called *hygroscopicity*. The amount of water adsorbed depends on the RH and temperature of the surrounding air and on the chemical composition of the aerosols. As it was explained in the previous section, atmospheric aerosols are composed by many chemicals species: many of them present a hygroscopic behavior whereas others are hydrophobic.

Thus, the hygroscopic property are usually described with two parameters, i.e. the *hygroscopic growth factor* (HGF) and the *hygroscopicity parameter* κ.

The latter one was proposed by Petters and Kreidensweis (2007)[26] in order to express the particle water content in the subsaturated regime with a unique parameter and to predict the conditions for cloud droplet activation.

In subsaturated conditions, i.e. RH<100%, the HGF is the parameter commonly used due to its easy calculation: it is based on the ratio between the measurement at a given RH condition

and the measurement in dry condition. Suppose that a particle diameter (d) measurement is carried out; the dHGF at a given RH would be calculate as follows:

$$dHGF(RH) = \frac{d(RH)}{d_{dry}} \qquad (Eq.\ 1.2)$$

where *d(RH)* is the particle diameter measured at a chosen RH and d_{dry} is the one measured in dry condition. Usually, dry conditions are supposed at RH<40%[27].

A variety of different techniques were developed in the last decades in order to investigate the hygroscopic behavior of particles with different chemical compositions.

The hygroscopic tandem differential mobility analyzer (HTDMA) is one of the most widespread used techniques. This method allows to choose the dry electrical mobility diameter (equal to a spherical particle having the same mobility in an electric field) of interest from an polydisperse aerosol population to a monodisperse one forcing aerosols within a cylindrical capacitor (DMA). The monodisperse aerosol flow is then humidified and passed through a second DMA. The particle size distribution of the outlet flows from DMAs is usually observed coupling a condensation particle counters (CPC) to HTDMA. This allows to obtain a growth factor probability density function. Generally, the integral properties of the probability density function are reported discerning the modes identified, i.e. not, less or more hygroscopic particles. The increase in particle diameter is assumed to be due to the water vapor condensation on particles. The HTDMA technique allows the observation the hygroscopic growth of submicrometric particles from about 10 nm up to 900-1000 nm in electrical mobility diameter by ramping the DMA voltage with a time resolution of 20 min – 1 hour.

Another main technique consists in using an electrodynamic balance (EDB). This instrument is able to levitate a single particle in the range 1 – 100 μm balancing the gravitational force with an alternating electrical field. The variation in the mass of a levitated particle, which corresponds to a change in the gas phase RH, can be determined from the adjustment of the direct current electrical field that is needed to keep the particle levitated. Conversely to the HTDMA, the EDB technique allows to scan a chosen RH range (both increasing and decreasing) since the particle can be levitated for long time but, since only one particle can be analyzed, atmospheric particles can not be investigated.

The nephelometer method consists in measuring the light scattering coefficient of ambient aerosol. Also in this case, the air flow is firstly preconditioned at low RH and scattering coefficient is determined by nephelometer once. Then, the airflow is humidified at a chosen RH and again analyzed by nephelometer. With this technique a scattering hygroscopic growth factor is therefore obtained.

Other methods investigate the hygroscopic behavior of deposited particles with optical, infrared, environmental electron and transmission microscopy, attenuated total reflection Fourier transform infrared spectroscopy techniques, filter analysis gravimetry and tandem optical particle counters[28–34].

The majority of the studies for single or mixture of hygroscopic compounds (such as AS, AN and sodium chloride) observed that an abrupt change in the investigated signal occurs both during increasing and decreasing RH conditions. These changes are associated to a change of physical state of the studied compounds.

2.1 – The aerosols phase transitions

In Figure 1 a schematic representation of the hygroscopic behavior of a single salt is shown. When a pure salt particle is exposed to increasing RH conditions, the Gibbs free energy of its solid state decreases. Until Gibbs energy for solid state is lower than that of the liquid phase, the particle remains solid (Figure 1,1). The RH value at which these free energies are equal is called deliquescence relative humidity (DRH) and the deliquescence process occurs, leading to the formation of a saturated aqueous solution (Figure 1,3). Before deliquescence, one or few water layers are adsorbed onto a solid particle (Figure 1,2)[32]. From DRH point, hygroscopic growth, i.e. water condensation, is allowed and the particle size increases in response to an increase of RH of the surrounding air (Figure 1,4). Therefore, the aqueous solution concentration decreases.

Table 1 Phase transitions relative humidity values at 298 K for salts commonly found in atmospheric aerosols.

Salt	DRH (%)	CRH (%)
$(NH_4)_2SO_4$	80±1	35±2
NH_4NO_3	61±1	not observed
NaCl	75	45
$NaNO_3$	70-74	40
$2NH_4NO_3 \cdot (NH_4)_2SO_4$	56.4	not observed
Na_2SO_4	84±1	55-57

Many authors[31,35–39] experimentally demonstrated that a mixture of different compounds can affect the hygroscopic properties of an internally mixed particle reducing its DRH. This is due to the fact that the activity of water decreases when another electrolyte is added to the system and the resulting DRH is always lower than the DRH of the individual salts in the particle[2].

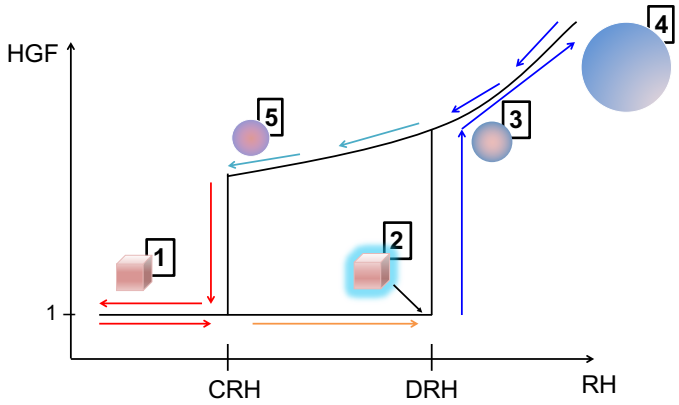

Figure 1 Simplified representation of a pure hygroscopic aerosol response to change in RH conditions.

Once that a particle deliquesces, a decrease in RH condition leads to a water evaporation in order to maintain the equilibrium with the gas phase. At the DRH value, the aqueous solution reaches the saturation. On the other hand, the dissociated salt does not crystallize in these conditions. In an aqueous solution, ions randomly move and they continue to associated and dissociated. In order to create a stable cluster, the surface energy associated with this has to be lower than the energy for dissociation. Especially, small clusters are not favourited[40]. On the contrary, if a sufficiently large cluster forms by random collision, the energy decreases and a nucleation germ is formed leading to a crystallization process. Therefore, a high supersaturation (Figure 1,5) is needed. These conditions do not occur at DRH but at lower RH, termed crystallization relative humidity (CRH). In a pure solution a very high supersaturation is needed and this process is called homogeneous nucleation. Conversely, heterogeneous nucleation is promoted by the presence of solid surfaces in contact with the aqueous medium. The activation barrier for the nucleation is therefore lower and the phase transition can proceed faster and at lower supersaturation conditions. Han and Martin (1999) investigated the heterogeneous crystallization of ammonium sulfate and inclusions of Al_2O_3, TiO_2 and ZrO_2. They observed that these insoluble inclusions increase the CRH of ammonium sulfate at 298 K from 35% RH up to 57%, 65% and 59% RH, respectively. In addition, the results from Onasch et al. (2000) showed that the presence of a 500 nm inclusion of $CaCO_3$ increases the CRH of a 15 µm AS droplet up to 50% RH. Martin et al. (2001)[41] explored the dependence of the mineral inclusions size of hematite (α-Fe_2O_3) and corundum (α-Al_2O_3) on the crystallization of AS particles at 298 K. The authors observed that a 450 nm sized hematite inclusion can increase the crystallization of AS up to 60% RH due to heterogeneous nucleation (Figure 2). In a recent paper, Davis and co-authors (2015)[42] investigated the crystallization process induced by a single contact between a supersaturated aqueous droplets and a solid inorganic crystal. One of the most relevant results is the demonstration that AN aqueous particles can crystallize even at very few RH points below

its DRH (61% RH). This result is of great importance since it suggests that AN crystallization can easily occur within the atmosphere, whereas no observation is provided about its homogeneous crystallization.

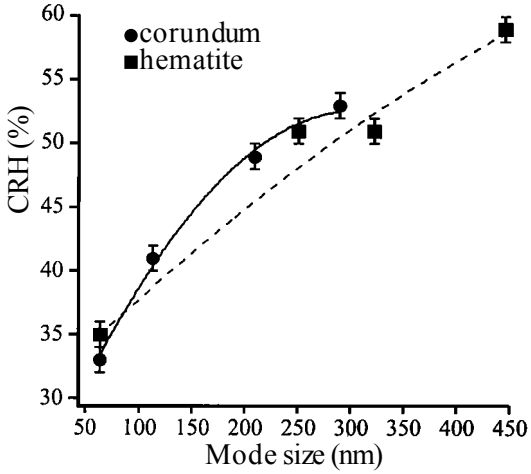

Figure 2 Ammonium sulfate heterogeneous nucleation induced by mineral inclusions. Figure adapted from Martin et al. (2001).

Since deliquescence and crystallization do not occur at the same RH point, an hysteresis loop is observed (Figure 1). This fact has important implications for many processes. In this work, some of them will be shown.

2.1.1 Temperature dependence of phase transition processes

Wexler and Seinfeld(1991)[43] and then Tang and Munkelwitz (1993)[39] investigated the effect of the temperature on the DRH. When a salt is in equilibrium with its liquid phase, the heat of condensation of water vapor is equal to the negative value of its heat of vaporization ($-\Delta H_v$), while the solubilization of the salt absorb a heat equal to the enthalpy of solubilization ΔH_s. Because of this, the overall enthalpy change by the reaction of water condensation and the one of salt solubilization is:

$$\Delta H = k\Delta H_s - \Delta H_v \qquad (Eq.1.3)$$

where k is the solubility of the salt in water expressed in moles of solute per mole of water. The Clausius-Clapeyron equation provides the change in water vapor pressure (p_w) over a solution with temperature, therefore the Eq. 1.3 becomes:

$$\frac{d\ ln\ p_w}{dT} = \frac{\Delta H_v}{RT^2} - k\frac{\Delta H_s}{RT^2} \qquad (Eq.1.4)$$

For pure water, Clausius-Clapeyron equation is:

$$\frac{d\ ln\ p_w^0}{dT} = \frac{\Delta H_v}{RT^2} \qquad (Eq.1.5)$$

where p_w^0 is the saturation vapor pressure at a given T. Substituting the Eq. 1.3 in Eq 1.4, it is:

$$\frac{d\ ln \frac{p_w}{p_w^0}}{dT} = -k\frac{\Delta H_s}{RT^2} \qquad (Eq.1.6)$$

At DRH, p_w/p_w^0 is the water activity of in solution, i.e. *DRH/100*. Thus:

$$\frac{d\ ln(DRH/100)}{dT} = -k\frac{\Delta H_s}{RT^2} \qquad (Eq.1.7)$$

Since the solubility k can be written in a polynomial form function of T (where coefficients A,B and C are tabulated for many salts), the T-dependence of DRH can be expressed with the equation provided by Tang and Munkelwitz (1993)[39]:

$$DRH(T) = DRH(298) \cdot exp\left\{\frac{\Delta H_s}{R}\left[A\left(\frac{1}{T} - \frac{1}{298}\right) - B\ ln\frac{T}{298} - C(T - 298)\right]\right\} \qquad (Eq.1.8)$$

Table 2 Example of T-dependence of DRH. Data taken from Seinfeld and Pandis (2006)[2].

	DRH (%)		
Salt	273.15 K	288.15 K	303.15 K
$(NH_4)_2SO_4$	81.8	80.6	79.5
NH_4NO_3	76.6	68.1	58.5
$NaNO_3$	80.9	76.9	73.0

As it is shown in Table 2, DRH of AS is affected by a very weak T-dependence. On the contrary, DRH of AN shows a strong decrease when T of the surrounding air increases.

Since crystallization is a kinetically controlled process, no thermodynamic model predicts the T-dependence of CRH. Few authors investigated this relation[44–46], observing a similar behavior of CRH in respect of DRH, i.e. a increase in CRH at lower T (see Sect. 4), since the supersaturation of most solids at fixed water activity increases under cold conditions[47].

SECTION 3 – MODELLING AEROSOLS HYGROSCOPICITY AND PHASE TRANSITIONS

As it is highlighted in Sect. 2.1, the deliquescence process is thermodynamically controlled. Therefore, several models were developed in order to predict the repartition between gas and aerosol phases of an inorganic systems. The most used are the *Extended-Aerosol Inorganic Model* by Clegg et al. (1992, 1998)[48,49] and ISORROPIA by Nenes (1998, 2007)[50,51]. Both these models allow to calculate the amounts of condensed water absorbed by the aerosol system as a function of the surrounding air T and RH. This leads to an estimation of the DRH of the considered system.

Conversely, the crystallization process is kinetic-controlled and no models were found in literature, except for the empirical one proposed in Martin et al. (2003)[47], based on experimental findings.

In this work, the experimental data obtained with the used method (described in Chapter II) are compared with the results of E-AIM II (Sect. 3.1) and of Martin's model (Sect. 3.3) for DRH and CRH, respectively. Therefore, the aim of this section is to provide the basic information about the models used for comparison.

3.1 – The Extended-Aerosol Inorganic Model (E-AIM) II

The E-AIM model was developed in order to predict the repartition among gas, solid and liquid phases of inorganic compounds in an aerosol system but its estimations are valid in a bulk one as well. The model is available online (http://www.aim.env.uea.ac.uk/aim/aim.php) and a further improvement (E-AIM II) considers a system composed by H^+–NH_4^+–SO_4^{2-}–NO_3^-–H_2O in a temperature range between 200 K and 328 K. The model calculates the activity of aqueous phase, its equilibrium with the gas phase by means of Henry's law and the one between liquid and solid phases by means of the equilibrium constant. The E-AIM II calculates the total Gibbs free energy at constant pressure and at given T and RH conditions by means of the estimation of the equilibrium constants of the phase transitions, changes in enthalpy and heat capacity.

In order to calculate the partitioning of the different chemical species in the three phases, the model needs as input the moles of the inorganic ionic ions at the charges neutrality:

$$\sum j \cdot n = 0 \qquad \textit{(Eq. 1.9)}$$

where n is the mole amount of ionic species with charge number j.

The E-AIM II was developed in order to calculate the repartition of the inorganic fraction. In addition, the models consider the presence of some carboxylic organic compounds (such as glutaric and succinic acids). The user can also add other organic species into the considered aerosol system inserting some thermodynamic properties of them (like surface tension, volatility, molar volume, etc.). The organic compounds are therefore distributed within an aqueous and organic hydrophobic liquid phase.

3.2 – The ISORROPIA II model

This model was developed by Fountoukis and Nenes (2007)[51] from ISORROPIA [50]. ISORROPIA II demand RH, T and concentrations of NH_3, H_2SO_4, Na, HCl, HNO_3, Ca, K and Mg and calculates the ratio of the cation species with sulfate ions, discerning a "crustal species ratio" (considering Ca^{2+}, Mg^{2+} and K^+), "crustal species and sodium ratio" and "total sulfate ratio". Once that the possible salts are determined, the model calculates the equilibrium reaction constants, the activity coefficients and, at the end, the concentration of the different species in gas, solid or liquid phases. The model neglects organic compounds.

3.3 – An empirical model for homogeneous crystallization

Martin et al. (2003)[47] studied the homogeneous crystallization for particles system composed by SO_4^{2-}, NO_3^-, NH_4^+ and H^+ at 293 K by means of an IR method[41]. On the basis of their measurements, the authors proposed a model optimized considering two parameters: ammonium fraction (X) and sulfate fraction (Y) calculated as follow:

$$X = \frac{[NH_4^+]}{[NH_4^+] + [H^+]} \qquad \textit{(Eq. 1.10)}$$

$$Y = \frac{[SO_4^{2-}]}{[SO_4^{2-}] + [NO_3^-]} \qquad \textit{(Eq. 1.11)}$$

Martin and co-authors proposed two equations to calculate the CRH valid for [X,Y] such that CRH(X,Y)≥1%:

$$CRH_{start}(X,Y) = -697.908 - 15.351X + 0.43X^2 - 22.11Y + 33.882XY - 1.818X^2Y + 0.772Y^2 - 1.636XY^2 + \frac{17707.6}{25 + (X - 0.7)(Y - 0.5)} \qquad \textit{(Eq. 1.12)}$$

$$CRH_{end}(X,Y) = 3143.44 + 63.07X + 0.114X^2 + 87.97Y - 125.73XY + 0.586X^2Y + 0.95Y^2 - 1.384XY^2 + \frac{79692.5}{25 + (X - 0.7)(Y - 0.5)} \qquad \textit{(Eq. 1.13)}$$

where Eq. 1.12 and Eq. 1.13 provides the starting and the ending CRH values, which it means that crystallization is estimated to occur within a RH range.

SECTION 4 – DELIQUESCENCE AND CRYSTALLIZATION MEASUREMENTS IN LITERATURE

During the last decades, a growing attention was focused on the study of aerosols hygroscopicity and their phase transitions. Due to the fact that atmospheric hygroscopic compounds are mainly composed by AS, NaCl and AN, the majority of the works investigated with a number of techniques the HGF of these compounds. Usually, these investigations scanned RH ranges from low RH up to 85-90% RH mostly. This leads to an observation of most of the studied compounds.

For example, Hu et al. (2011)[52] used a HTDMA to investigate the hygroscopicity of AS in the size range of 40-200 nm during increasing RH conditions from 20% to 86% RH. They experimentally observed the DRH point observing a sharp increase in HGF between 80% and 82% RH. Ebert et al. (2002) used an environmental scanning electron microscopy technique to observe the DRH of NaCl, AS, Na_2SO_4 and AN at different T. Electrodynamic balance was used in many works, such as in Lightstone et al. (2000)[53],Choi et al (2002)[54] and Sjogren et al. (2007)[55], in order to measure the hygroscopic behavior of some inorganic salts and mixtures with organic compounds, observing the phase transitions as well. Xu et al. (1998)[45] used a single-levitated

particle method to derive a temperature-dependent phase diagram for of a binary $(NH_4)_2SO_4/H_2O$ system from 40 to -50°C. They found a slightly increase in efflorescence condition with a decrease in temperature. Onasch et al. (1999)[56] used a FTIR technique to evaluated the efflorescence of pure $(NH_4)_2SO_4$ aerosols in the temperature range of 234-295 K, showing an inverse relationship between crystallization point and temperature. Zeng et al. (2014)[32] identified a positive relation between CRH and T opposite to a negative one for sodium methansulfonate but no explanation about this different trend between the two compounds was found by the authors.

In the last ten years, electrical methods were developed[57–61] able to identified the phase transitions relative humidity without quantifying the hygroscopicity of the investigated compounds. Yang et al. (2006)[57] measured the impedance drop of a conductivity cell constituted by porous paper saturated with a pure or mixture salt solution. Once the solution was completely dried, the surrounding RH was changed. Their results suggest a good applicability of the method since they found at 323 K a DRH of 86±1.5% RH for Na_2SO_4 salt in agreement with the one found in literature (i.e. 84±1% RH at 298 K)[40]. Similar measurements were developed for tests in which deliquescence of hygroscopic contaminants can promote metals corrosion. Schindelholz et al. (2014)[58] dried a microdroplets on an interdigitated array microelectrode and measured the impedance response while varying the exposure RH conditions. They observed a sharp decrease in the modulus of impedance at 75% RH when the array was contaminated with a NaCl droplet. They also observed that the impedance increased during decreasing RH conditions and an abrupt increase was recorded at 50% RH, showing an hysteresis loop.

A growing number of papers reports the DRH and CRH aerosol systems with higher chemical complexity[31,36,37,62–66]. Smith et al. (2012)[67] used a dual arm HTDMA to investigate the DRH and CRH of aerosol system composed by AS mixed with isoprene-derived secondary organic material from photo-oxidation of isoprene. They found that DRH of the aerosol system decreased from 80% RH for pure AS aerosols to 40% for aerosols with 0.9 organic volume fraction, while CRH decreased from 35% RH for pure AS to RH lower than 20% RH for 0.6 organic volume fraction. Cruz and Pandis (2000)[68] performed hygroscopic measurements with HTDMA on aerosol systems composed by NaCl or AS with pinonic and glutaric acids with no observed effects of the last two on the DRH of the inorganic salts. Gupta et al. (2015)[35] studied mixtures of NaCl-$NaNO_3$ particles as surrogates of sea-salt aerosols. They showed that depending on the mixing ratio of the solution, particles can exhibit one or two distinct deliquescence processes. Ling and Chan (2008) studied the phase-transitions of systems formed by $(NH_4)_2SO_4$ and malonic acid, glutaric acid and succinic acid evidencing that the organic acids affect the deliquescence of the system, leading to a gradual dissolution of the solid particles. Miñambres et al. (2013) highlighted the effects of organic dicarboxylic acids in an early water uptake for a complex system of ammonium sulfate-dicarboxylic acids and the gradual deliquescence of the mixture.

Dougle et al. (1998) studied the effect of soot in crystallization of NH_4NO_3-$(NH_4)_2SO_4$ system and stated that it has no effect on this process.

Despite an abundance of measurements carried out for simplified aerosols systems, few papers focused on real atmospheric ones. On the other hand, a growing number of data is available by means of many online techniques, basically using HTDMAs and nephelometer equipment.

Ten Brink and co-authors (1996)[69] performed a measuring campaign in The Netherlands in November and December 1993. They coupled a thermodenuder analyzer in order to quantify the presence of AN and AS and a humidity controlled nephelometer measuring the aerosol light-scattering at different RH level. A heater-cooler system was applied in order to scan the lower branch of the hysteresis loop and increase the RH of the aerosol airflow. The airflow was firstly dried heating it, then it was forced to pass within a humidifier chamber in which distilled water was sprayed and the temperature was increased or decreased in order to change the RH of the airflow. The upper branch of the hysteresis loop was also scanned heating the airflow. The authors considered negligible the ammonium nitrate loss due to high temperature since they avoid temperature higher than 313 K. Increasing the humidity from 20% to 90% RH and reverse, they reported an example of an ambient hysteresis loop occurred on 17 November 1993 when two DRH were observed (Figure 3): the first at 62% RH (associated to AN) and the second one at 80% (associated to AS), whereas no crystallization was observed since the scattering HGF did not reached the unity value even at low RH.

Other authors developed some techniques in order to identify the hydration state of atmospheric aerosols at ambient RH. Rood et al. (1989)[70] used a similar method to the one of Ten Brinks in three urban and rural sites. The sampled airflow was ramped from ambient temperature to 623 K in 4 minutes and then cooled to ambient T while a nephelometer measured the light-scattering of the aerosols. The authors observed that metastable droplets occurred for more than 50% of the time for ambient RH values in the range 45-75% RH. These results were considered of great importance by the authors since ambient RH was between this range for about 38% of the measuring time.

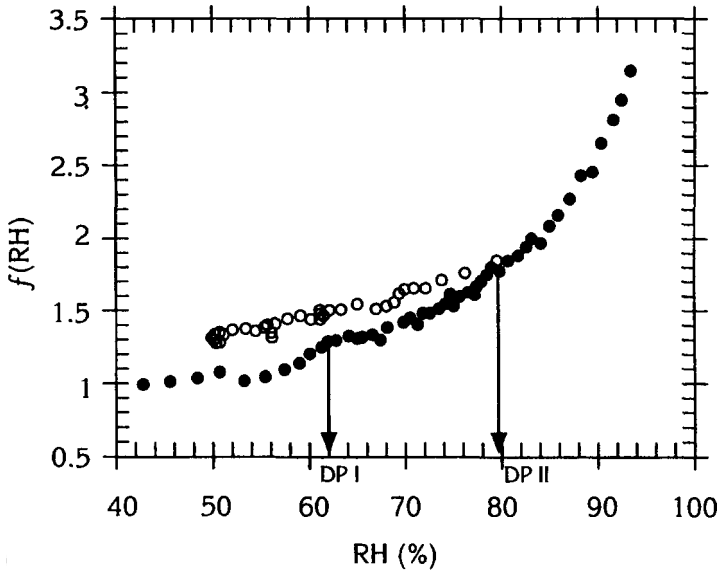

Figure 3 Aerosol light-scattering growth factor f(RH) as a function of relative humidity. The graph was published in Ten Brink et al. (1996) [69].

In Santarpia et al. (2004)[71], Martin et al. (2008)[72] and Taylor et al. (2011)[73] multiple DMAs were used to create a monodisperse aerosols airflow together a humidifying and drying systems in order to force the aerosols airflow to experience the hysteresis loop. Santarpia (2004)[71] observed that in College Station (Texas, U.S.) ambient aerosols (with dry size of 160 and 320 nm) were mainly in the metastable state between 53% and 69% RH. Taylor (2010)[73] found in eastern Tennessee that 12% of the sampled aerosols were within the hysteresis loop on the upper branch during SU season. On the contrary, during WI the hysteresis loops conditions occurred for 49% of the time and the aerosols occupied the upper branch for 65% of this time. They also observed that DRH occurred between 45% and 75% RH, with a maximum in frequency between 65% and 70% RH. Similarly, CRH was identified most of the time at RH<30% but it was observed even between 55% and 60% RH. This results regards particles with dry sizes below 200 nm.

These methods present a very high time resolution but no chemical characterization is often coupled, since only few instruments are able to perform it with such a high time resolution, such as an aerosol time-of-flight mass spectrometer. In addition, all of these devices are extremely costly.

In most atmospheric phenomena, the effects of the atmospheric aerosols are due to their overall physical and chemical dynamics. Therefore, although the comprehension of small sized

range of particles is needed, an investigation of increasing sized and chemically complex aerosol system can lead to the observation and characterization of different integrated effects.

An example of this is shown in Song et al. (2013)[61]. In this paper the investigation of the corrosive effects of unsized particles contaminants on electrical circuits was carried out. The authors contaminated a printed circuit board (PCB) with a coarse deposit brushed off the surfaces of a multi-level outdoor garage in an urban area of Tianjin (China) and measured the impedance at increasing RH conditions and at different T. Coupling impedance measurements and ion chromatography technique, Song and co-authors highlighted that these parameter are useful to classify the risk of corrosion associated to particles contaminations.

SECTION 5 – CONCLUSIONS

In this chapter the main features of atmospheric aerosols were summarized in order to introduce the topic of this thesis. As it was shown, atmospheric aerosols are extremely complex open-systems affected by mass transfer, chemical reactivity and changes in thermodynamic air conditions. The role of water, considered as moisture and in the liquid phase, in the aerosols dynamics was highlighted. In this regards, the knowledge of the aerosols response to changes in relative humidity can improved the comprehension of many atmospheric phenomena, such as clouds formation and radiative forcing, and the interactions between aerosols and human activity.

In particular, in order to improve the understanding of these last interactions, the aerosols behavior has to be considered as an integrated behavior of different particles in size and in chemical composition.

In this work, the lack of a standardized method able to identify the phase transitions and the hygroscopic properties of a broad size range of real atmospheric aerosols was overcome by means of an off-line method based on the analysis of the electrical properties of the fine fraction (i.e. $PM_{2.5}$) exposed to different RH conditions with a high resolution. The use of this off-line method allows to relate the transitions with the chemical composition of real aerosol samples. Since the response to the applied method is due to the overall behavior of the aerosols, the system is considered formed by internally-mixed aerosols.

The following chapters describe the electrical conductance method and its agreement with a gravimetric method (Chapter II); both of them were used to characterized the DRH and CRH of atmospheric aerosols sampled in Milan (Po Valley, Italy) and a discussion with their seasonal chemical composition is provided (Chapter III). In addition, an estimation of aerosols physical state and their hydration time in the atmosphere was carried out (Chapter III).

The aim of this work is to provide a contribution relating to the implications of aerosols physical states with human activities.

In Chapter IV, the hysteretic response of aerosols to RH changes is related to $PM_{2.5}$ concentration monitoring by means of remote sensing techniques. It is shown that neglecting the hysteresis leads to substantial error in estimations. In the same chapter, aerosols physical states are considered in order to develop two parameters useful in cultural heritage climatology risk assessment.

Finally, the effects of aerosols contamination on materials were investigated in relation to corrosive behaviors on printed circuit boards assembly (Chapter V) and the application of this investigation was exemplified in the corrosion prevention in free-cooled data centers (Chapter VI).

CHAPTER II – METHODS

1 – THE EXPERIMENTAL APPROACH

The lack of a method that allows the study of a broad size range of atmospheric aerosols is here overcome with the conductance method, which is here described. Actually, similar methods were found also in Yang (2006)[57], Song (2013)[61] and Schindelholz (2014)[58]; nevertheless, Yang and Schindelholz focused their attention on the applicability of the electrical method on pure salts, whereas Song studied the corrosion effects of 'two natural dust samples' brushed off the surfaces from a height of two meters above the ground. Recently, D'Angelo et al. (2016)[74], Casati et al. (2015)[75] and Ferrero et al. (2015)[76] used the conductance method in order to investigate the phase transitions of the fine fraction of the real atmospheric aerosols, i.e. $PM_{2.5}$, sampled directly from the atmosphere. The present chapter provides an extended description of the conductance method used in these lasts three papers.

1.1 Aerosol sampling

In order to guarantee the simple applicability of the method, aerosols were collected as $PM_{2.5}$ fraction on the most widespread filters media, that are PTFE filters (Pall, Teflon filter, PMP support ring, ∅=47 mm) and quartz fiber filters (Millipore, ∅=47 mm). Sampling was carried out by means of a gravimetric low-volume sampler FAI-Hydra Dual Channel Sampler (2.30 m^3 h^{-1}), according to EN-14907.

The aerosols collection was set in term of duration with the scope to obtain comparable masses among the different sampling periods. The sampling campaigns were carried out in Milan at Torre Sarca site (Po Valley, Italy, 45°31'19"N, 9°12'46"E), a site located close to a high vehicle busy road in the northern side of Milan, the most populated city of the whole Po Valley.

In this valley, that is a famous air-polluted hot spot[77], particulate matter (PM) concentration is strongly influenced by meteorological conditions. Winter seasons are characterized by very low mixing height caused by strong atmospheric stability. As reported in Ferrero et al. (2014)[78], measuring campaigns with tethered-balloon over Milan showed an average mixing height of 272±50 m above ground level in the late morning. This thin mixing layer causes a high $PM_{2.5}$ concentration as reported by the local agency for the environmental protection (ARPA Lombardia) whose data show an average $PM_{2.5}$ concentration of 32.66±1.90 μg m^{-3} at ground level in Milan in WI. On the other hand, in the summertime the mixing height was found to be higher than 600 m above ground level before 09:00 UTC (Ferrero et al., 2011)[79] and $PM_{2.5}$ concentrations at ground level are significantly lower than in winter (18.98±3.29 μg m^{-3}).

Therefore, in order to consider the variability in aerosols concentrations, the wintertime campaigns were carried out setting a sampling time at 24 h whereas it was set at 48 h during summertime.

As recommended in EN-14907, filters were hold in dry conditions (RH<10%) before weighting and sampling. The weighting was carried out by means of a weighting precision balance Sartorius SE-2F (precision 0.1 μg, maximum load 2.1 g) and was repeated at least three times accepting a variability of less than 1% both before and after the sampling. The removal of electrostatic charges was allowed by means of an ozone generator. After the aerosols collection, filters were stored in the darkness in order to avoid photochemical reactivity, at low temperatures (~277 K) to avoid semi-volatile compounds volatilization and low RH (<10%) for 48 h. The collected $PM_{2.5}$ mass were estimated subtracting blank filter mass to sampled ones.

$PM_{2.5}$ samples were collected between 2006 and 2014 and stored in the Filter Bank of the University of Milano-Bicocca, where filters were preserved at 253.15 K in the darkness.

Prior to perform further analyses, the filters were placed in a PTFE holder and cut perfectly in two halves with a die cutter. The uniform distribution of PM samples on filters has been demonstrated in Owoade et al. (2006)[80]. After this, the samples were again stored for 48 h at low RH conditions (<10%) at room temperature.

1.2 The Aerosol Exposure Chamber and RH cycles

For each sample, a half filter only was used to characterized the phase transitions RH. For this scope, an Aerosol Exposure Chamber (AEC) was specifically designed allowing the exposure of the aerosol samples to different RH conditions (Figure 4). The AEC is a 1 m^3 hermetically sealed chamber equipped with inert PTFE bypasses enabling measuring and phasing operations to be performed in the presence of moist or dry air. Up to six aerosol samples may be housed inside the AEC: they were positioned on special PTFE supports, and provided with a pair of electrodes (at a calibrated distance, i.e. 2.5 mm) each (Figure 4a).

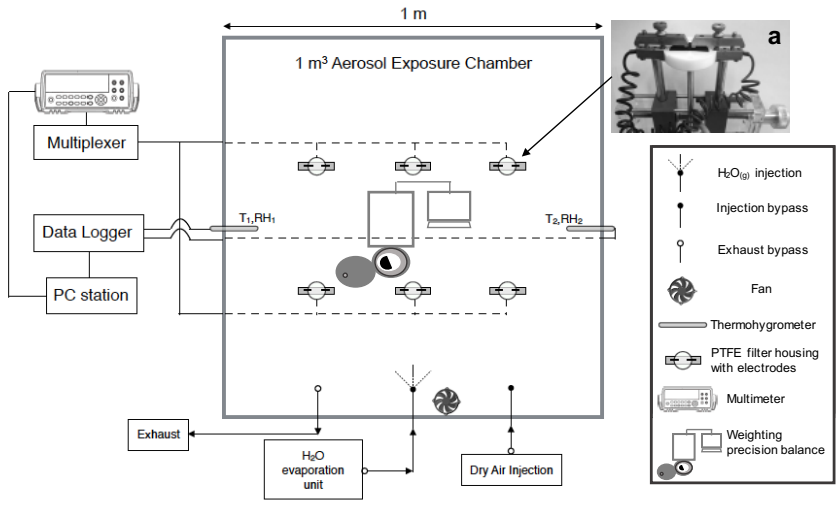

Figure 4 Schematic experimental setup.

Thermodynamic conditions within the chamber were monitored by means of two thermo-hygrometric sensors (DMA572 and DMA672, LSI-LASTEM, with a resolution of 0.25% for RH and of 0.035 °C for temperature, accuracy ±1% RH and ±0.1 K) with 10 s time resolution. The RH conditions were manually varied by 1% at a time. The increase in RH (humidification) was obtained slowly phasing in water vapor generated heating ultra-pure water (Milli-Q®; 18.2 MΩ·cm at 25 °C; Water Purification System, Millipore, Bedford, MA, USA) mixed with pre-filtered pure air (Aria Zero®, Sapio) into the AEC; conversely, pre-filtered pure air was phased in to reduce the RH (de-humidification). The averaged RH variation rate was 0.5% RH min^{-1}. In this regards, it was pointed out that small changes in RH conditions results in short equilibration time[81]. On the other hand, except for the time-of-equilibration experiments (see Sect. 2.1), measures were supplied after a waiting time of 2 minutes.

The hereinafter called RH cycle (humidification following by de-humidification) consisted in a step-by-step increasing and then decreasing RH ramp between 30% RH and 90% RH. Prior to start the RH cycle, the filters were housed in the chamber, blocked with the electrodes on the PTFE supports and held them at 30% RH for 30 minutes in order to reach the equilibrium with the surrounding air.

Experiment were carried out at room temperature (298±2 K) for the entire duration of the RH cycle; fluctuations in temperature were recorded but never greater than 1 K.

1.3 Conductance measurements and developments

For each RH step, electrical resistance of each sample was measured five times. The measurement system was controlled by NI LabVIEW software which was designed to automatically calculate electrical conductance as the resistance reciprocal.

At the beginning of the experimental activity, aerosols were collected with a sampling surface of 11.94 cm^2 on filters. The resistance measurements were carried out using a 3421A Data Acquisition Unit (Hewlett-Packard, range 0-30.1 MΩ) and electrodes gap was set at 5.0 mm.

On the other hand, as it is discussed in Paragraph 2.2.1, the sampling and the electrical measurement configuration were modified in order to increase the electrical signal. The sampling surface on filters was reduced to 1.07 cm^2 and the electrodes distance to 2.5 mm. In addition, the resistance measurements were carried out by means of an Agilent 34411A multimeter (DC, $6^{1/2}$ digits, resistance range 0Ω-1.43GΩ), connected to the cells by means of an Agilent L4421A 40-channels armature multiplexer.

Except for the data discussed in Paragraph 2.2, the results will be presented with the improved measurement configuration. Both two instruments allowed to scan six channels linked to six different samples exposed to the same RH cycle. For each RH step, 5 measurements of conductance were carried out. Within this work, the averaged electrical conductance values are presented without standard deviations that are always below 5% of the measures. In additions, a cubic spline was applied in order to estimate the conductance value at an accurately fixed RH. The associated error was considered negligible since the interpolation was operated within the precision range of the thermo-hygrometric sensor.

1.4 Aerosol chemical characterization

As it was previously highlighted, the chemical composition of atmospheric aerosols strongly influences the hygroscopic behavior and the phase transitions RH. For this reason, the second half of the $PM_{2.5}$ samples used in the AEC were chemically analyzed to determine the aerosol chemical composition by means of ion chromatography.

Cations (Na^+, NH_4^+, K^+, Mg^{2+}, Ca^{2+}) and anions (F^-, Cl^-, NO_3^-, SO_4^{2-}, acetate, formate, propionate, glutarate, succinate, malonate, oxalate) were analyzed using two coupled chromatography systems served by a shared auto-sampler (AS3000, Dionex, Sunnyvale, CA, USA) and controlled by the same PC (software Chromeleon 6.8, Dionex). Cations were determined using a Dionex ICS-90 Ion Chromatography System equipped with a pre-column (DionexIonPacCG12A-5 µm Guard 3x30 mm) and an analytical column (DionexIonPacCS12A-5 Analytical 3x150 mm); an isocratic elution was performed with methanesulfonic acid (MSA, 20 mM, Fluka 64280) at a flow rate of 0.5 mL min^{-1}. The eluent signal was suppressed using a chemical suppressor (Dionex CMMS III 4 mm MicroMembrane Suppressor, regenerant: tetrabutylammonium hydroxide, TBA-OH, 0.1 M, Fluka 86854). Anions were analysed by a Dionex ICS-2000 equipped with the Ion Pac AG11 4x50 mm Guard and Analytical AS11 4x250

mm columns, gradient eluent of KOH (0-50 mM), flow rate was 1 mL min^{-1}. The eluent signal was suppressed by means of an electrochemical suppressor (Dionex AMMS III 2 mm MicroMembrane Suppressor CR-ATC, continuously regenerated anion trap column).

Quantification was achieved by means of the external standard method. Standard solutions were made starting from solutions of each single ion (1000 mg/L, Fluka). Chemical analysis was carried out within 24 h following extraction. Extraction efficiencies have already been investigated in a previous work[4].

2 – RESULTS AND DISCUSSION

2.1 Equilibration time

The electrical response was monitored for 30 minutes at constant RH within the AEC in order to observe the time needed to reach the equilibrium in conductance measures. Figure 5 shows a typical equilibration time experiment. During 30 minutes, the RH conditions resulted to be constant with a fluctuation of less than 0.5% RH and this produced a constant electrical response (Figure 5b). In Figure 5a the RH exhibits an increasing trend during two RH steps, i.e. at 56% and 58% RH. Figure 5c shows that whenever RH is not constant the electrical conductance answers in perfect agreement (R^2=0.915). On the other hand, in this work no discussion about the conductance values is carried since it is used to identified the formation and crystallization of the electrolyte solution only and no quantitative relationship with the electrical signal was established.

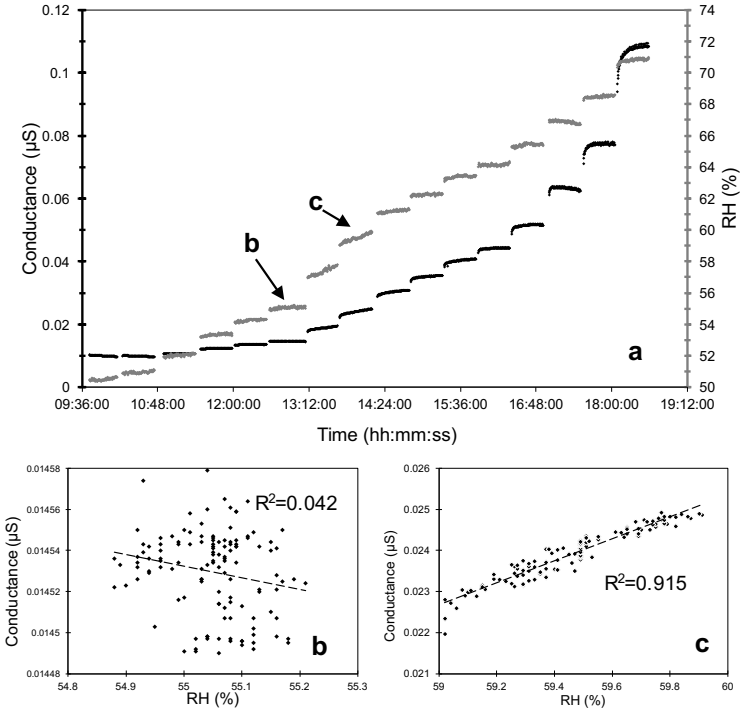

Figure 5 Electrical conductance during an increasing RH ramp (a). In grey markers are shown the RH measurements, in black the electrical conductance data.

Since the shape of the curves did not change considering the conductance values obtained at different time (Figure 6), the equilibrium was supposed to be reached by the system in few seconds. Because of this, the conductance measurements were carried out waiting two minutes after that the RH reached the target value.

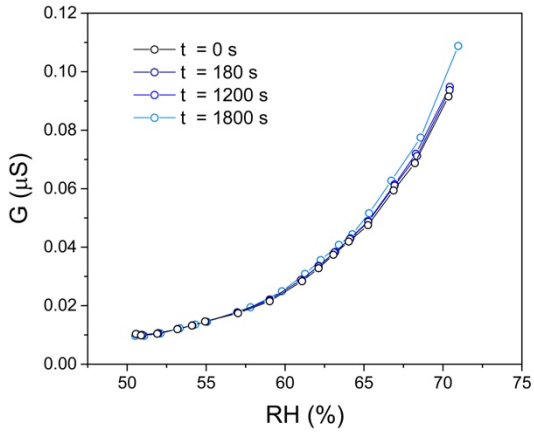

Figure 6 Conductance for each RH steps at 0 s, 180 s, 1200 s and 1800 s for the sample showed in Figure 5a.

2.2 Minimum aerosol loading

In the previous paragraph it was shown that the conductance measures are in equilibrium at each RH step. Aerosol hygroscopicity allows the water vapor adsorption and ions motions towards the electrodes as a consequence of a continuum electrolyte solution formation. On the other hand, the first investigated dataset of 55 samples showed that 18% of them (10 samples) provided no electrical response, i.e. their resistance was higher than the detection limit of 3421A Data Acquisition Unit, i.e. 30.1 MΩ (0.033 µS). Thus, the minimum aerosol loading required in order to perform conductance measurements was examined.

As a matter of fact, such behavior was not previously reported either in Yang et al., (2006)[57] or in Song et al., (2013)[61]. However, the experimental measurements of both the aforesaid studies were conducted in saturating conditions of aerosols on the investigated media, namely: Whatman filter paper soaked with saturated ionic solution[57], and an electric coupon test with 150-600 µg cm^{-2} of aerosol deposite[61], respectively.

Conversely, the total aerosol mass loading on the sampled filters varied with $PM_{2.5}$ ambient concentrations. The 55 $PM_{2.5}$ samples considered in this dataset spanned a range of atmospheric concentrations between 13.7 µg m^{-3} and 107.5 µg m^{-3}. These are typical values for the Po Valley, which is characterized by seasonally-modulated pollution[79,82]. Moreover, they turn into a similarly broad range of aerosol loading on the sampled $PM_{2.5}$ filters (24 h sampling time; flow 2.3 m^3 h^{-1}), from 63.2 µg cm^{-2} (0.755 mg on filters) to 496.6 µg cm^{-2} (5.932 mg on filters). Our range comprises values both below and above the minimum surficial aerosol deposition used by Song et al. (2013)[61].

Following this observation, the aerosol mass load on such filter samples, together with the total ionic fraction content, were investigated in order to determine minimum aerosol loading, so as to ensure detection of conductance changes while varying the RH in the AEC.

The average aerosol loading on the 45 $PM_{2.5}$ samples subset revealing electrical conductance responses was 221.9±13.5 μg cm^{-2} (2.651±0.161 mg on filters), a figure slightly higher than the lower surficial dose used by Song et al., (2013)[61]; conversely, the 10 $PM_{2.5}$ samples subset that did not show any electrical conductance response, displayed a statistically lower (t Student at α=0.01) aerosol mass loading, with a value of 127.1±7.8 μg cm^{-2} (1.518±0.094 mg on filters). Due to the important role of the aerosol ionic fraction in determining electrical signal conduction, the average ion loading on both $PM_{2.5}$ sample subsets was also addressed: 85.7±9.2 μg cm^{-2} (1.023±0.110 mg on filters) for those samples that showed electrical conductance responses to RH changes, and 53.1±6.5 μg cm^{-2} (0.634±0.077 mg on filters), for those that did not.

A value similar to the latter one can be derived by linearly correlating the ionic surficial loading of the $PM_{2.5}$ sample subset displaying an electrical conductance response (y), with conductance measurements (x) at 80% of RH; the intercept of the linear regression thus obtained (y = 1.8x + 50.0; not shown) permits estimation of the minimum ionic surficial mass below which no electric signals were detected: 50.0 μg cm^{-2}. It is worth noting that the ionic surficial loading for the 10 filters that did not show any signal, is not far off the theoretical value (24.2 μg cm^{-2}) estimated by Weschler (1991)[83] for pure 520 nm NH_4HSO_4 particles on the basis of the percolation theory[84,85]. However, as Tencer (2008)[86] reported, the value at which the aerosol starts to conduct the electrical signal and at which a bridging process commences, may vary according to the geographical region and the related aerosol properties (chemistry and size).

Thus, by following the aforementioned approach, but considering the whole $PM_{2.5}$ mass rather than the ionic fraction mass only, as the "y" variable, the minimum $PM_{2.5}$ mass for detection of an electrical signal proved to be an average daily $PM_{2.5}$ concentration of 27.5 μg m^{-3} in Milan. Data from ARPA-Lombardia (the Lombardy regional branch of the Italian Regional Environmental Protection Agency) show that this concentration is exceeded in Milan on more than 70% of winter days, and on 34% of all days throughout the year.

In order to overcome the minimum aerosol loading limit, some modifications were introduced starting from sampling to measurement configurations.

2.2.1 Sampling modifications

Firstly, the sampling time was set with the aim to collect a sufficient aerosol load. Whereas this load would be easily reached during winter seasons since $PM_{2.5}$ concentrations are mostly higher then 27.5 μg m^{-3}, during summertime low concentrations rarely get the minimum estimated concentration. Thus, aerosol sampling time was set different for winter seasons and summer seasons, i.e. 24 h and 48 h, respectively.

In addition, the electrical signal was supposed being higher with the decreasing of sampling area. For these reasons, the original sampling diameter of 39.0 mm was reduced to 30.0 mm (Figure 7).

The electrical behavior was then examined in order to observe the effect of this sampling configuration on conductance response. Four sampling pairs were exposed to RH cycle and electrical conductance was recorded.

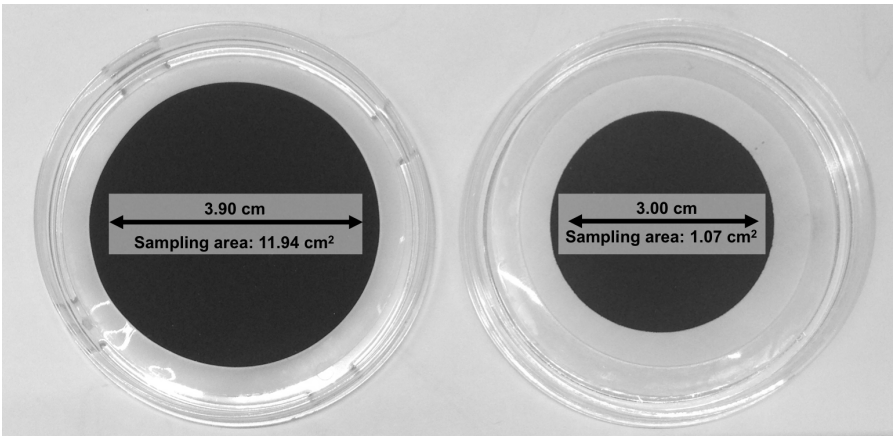

Figure 7 Original (left) and reduced (right) sampling area.

Figure 8 shows an example of the conductance profiles for both standard sampling area (11.94 cm^2) and reduced one (1.07 cm^2). For both increasing (a) and decreasing (b) RH ramp, an increase in conductance due to the increasing in $PM_{2.5}$ mass density was recorded without shape variations for the reduced spot profiles. The good agreement between the two sampling configuration is clearly shown in Figure 9.

On the other hand, a constant increase in conductance was not observed for the samples. Indeed, high R^2 coefficients were found (0.972±0.024 for increasing RH ramp and 0.928±0.068 for the decreasing one) but the slope values – which indicates the order of magnitude of the increasing conductance signal – was not comparable among the samples, which spanned from an almost negligible increase to several order of magnitudes.

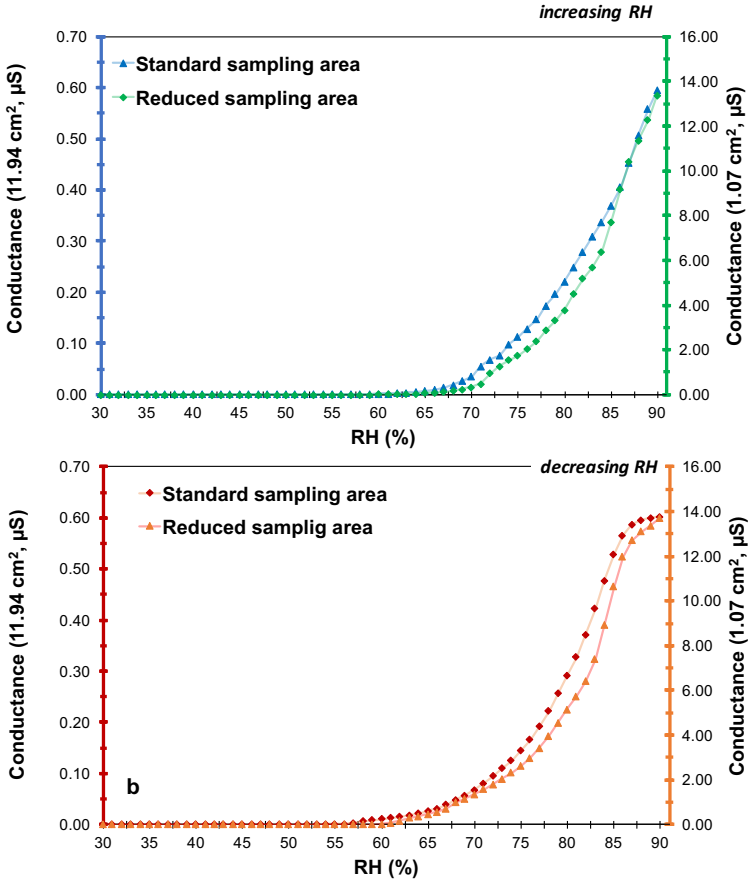

Figure 8 Conductance profiles for $PM_{2.5}$ fraction on standard and reduced sampling spot area during increasing (a) and decreasing (b) RH ramp.

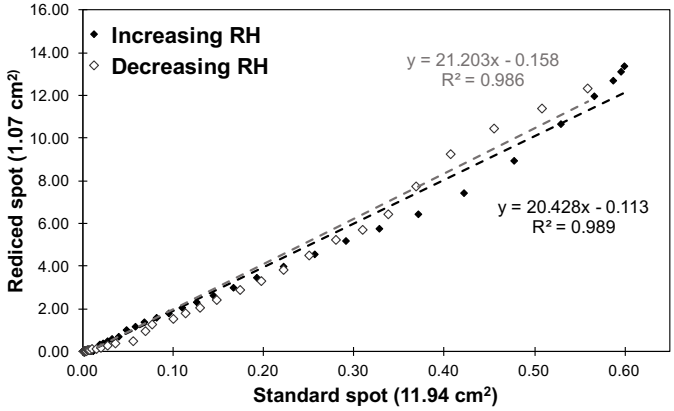

Figure 9 Standard and reduced sampling area correlation.

2.2.2 Measuring setting modifications

In order to further increase the electrical signal and, especially, the detection limit of the measuring system, a new digital multimeter (Agilent 34411A multimeter) coupled with a multiplexer (Agilent L4421A) was then used. Thus, the detection limit decreased from 0.03 μS (30.1 MΩ) down to 0.0007 μS (1.43 GΩ).

In addition, the electrodes distance was reduced from 5.0 mm to 2.5 mm (Figure 10). For this modification an increase in signal was observed as well. In this regards, the profile shape was found to be unchanged while an increase in conductance of 1.961±0.902 and 1.823±0.537 for humidification and de-humidification (averaged slope and dispersion from the averaged value) was recorded. The standard deviation values of slope highlighted that the increase in conductance was not similar among the seven sample pairs used for the comparison of the two configurations.

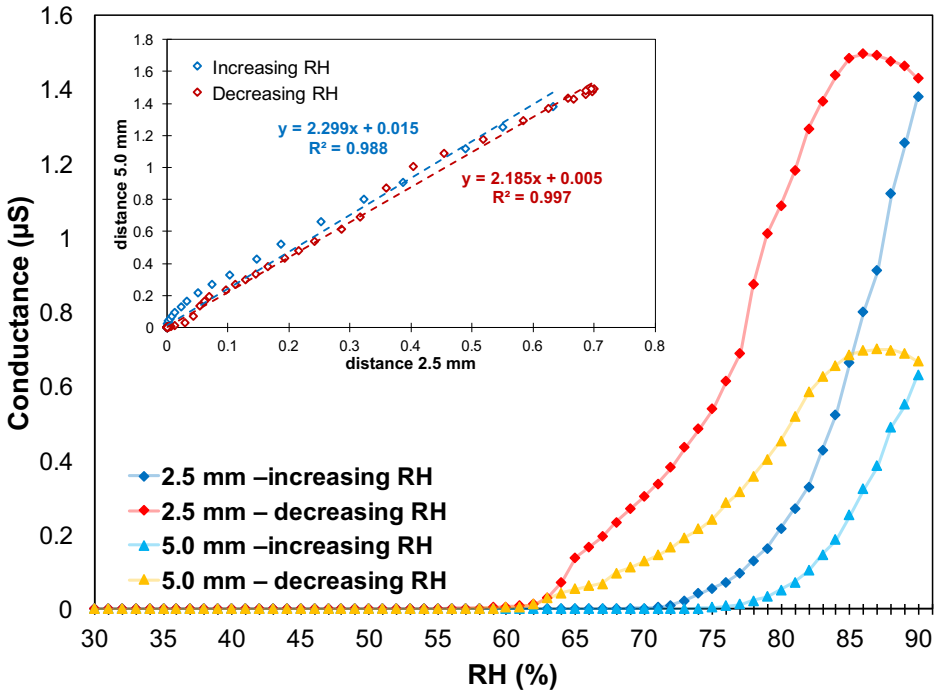

Figure 10 Example of conductance profiles with standard (5.0 mm) and reduced (2.5 mm)electrodes distance with the correlations during increasing and decreasing RH ramps.

While it was expected that conductance would have doubled, the results clearly showed that the increase in electrical signal was not. This fact could be due to some parameters which was neglected (such as the electrodes active surface geometry and their roughness, the geometry of the conductive path and the cell constant) or which was not under the user control.

The data which are shown in the remainder part of this work were obtained by means of the improved sampling and measuring configurations: aerosol samples were collected on 1.77 cm^2 surface area and conductance profiles were carried out by means of Agilent 34411A digital multimeter coupled with Agilent L4421A multiplexer setting 2.5 mm as electrodes distance.

2.3 Filter media effect

PTFE filters and quartz fiber filters are the most used filter media to collect ambient particles. They are mainly used because of they moderately costs and the advantages for chemical characterizations of inorganic fractions (PTFE) and carbonaceous fractions (quartz fiber). In order to evaluate the best substrate for hygroscopic particles studies, conductance analyses were carried out on these media. Eom et al. (2014)[29] studied the influence of six different media on

hygroscopic measurements. Their results highlight the importance in using hydrophobic substrates such as parafilm-M or TEM grids instead of hydrophilic ones. This because water condensation and spread over the media occur with an increasing interfacial energy between them. Thus, Eom and co-authors identified lower DRH values comparing with literature data. On the contrary, for crystallization processes Ag foils seemed to increase CRH due to the formations of seeds for heterogeneous crystallization composed by AgCl and $AgSO_4$ when they studied Cl^- or SO_4^{2-} containing solutions.

Awakuni and Calderwood (1971)[87] studied the water vapor adsorption on quartz fiber wafer and PTFE films. In their work, the authors reported the contact angle of PTFE as 104° while it is nearby 0° for clean glass surface. These properties agreed with the estimation provided by Awakuni and Calderwood who highlighted that close to saturation conditions, PTFE adsorbed three monolayers of water molecules while quartz fiber adsorbed seven monolayers. These findings gave reasons about the different conductivity behaviors observed by the authors which was noted to be higher for quartz fiber in respect of the PTFE.

In order to observe the difference conductance response to the RH conditions, the analyses were carried out for 38 $PM_{2.5}$ samples collected both for PTFE and quartz substrates. The conductance profiles for PTFE substrates highlighted different behaviors in function of RH level. In particular, the majority of samples showed an abrupt change in electrical signal during increasing and decreasing RH ramps at non coincident RH conditions, thus a hysteresis was clearly observed (Figure 11). In addition, high standard deviations in the averaged normalized profiles confirmed that the samples had different behavior in conductance. On the contrary, the conductance profiles for quartz fiber filters showed an exponential growth and decrease without hysteresis (Figure 12) and low standard deviations.

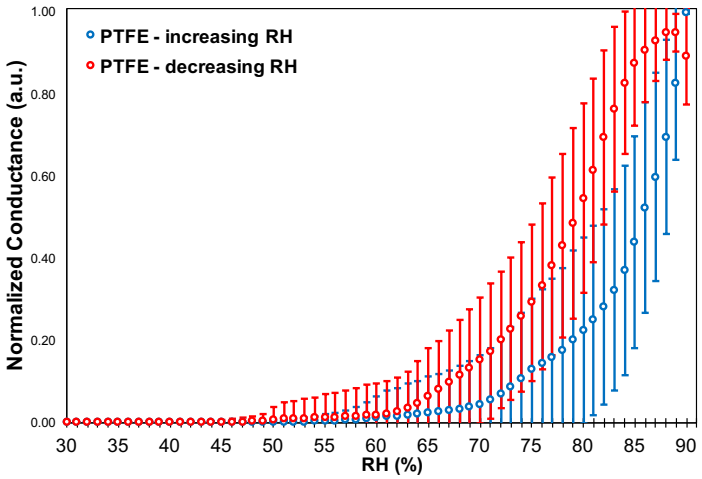

Figure 11 Averaged normalized conductance profiles for $PM_{2.5}$ samples collected on PTFE filters.

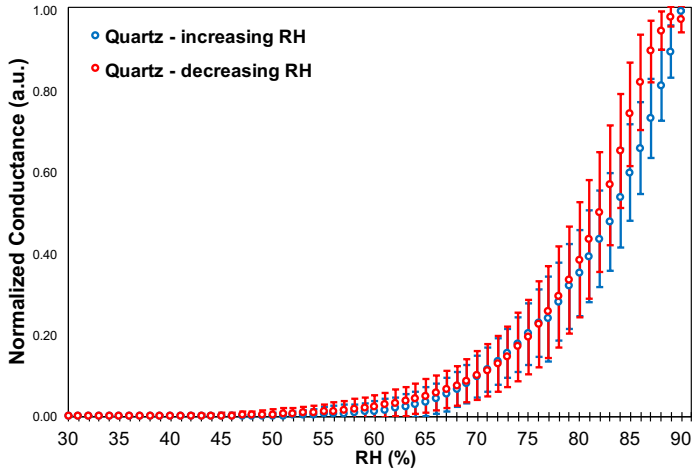

Figure 12 Averaged normalized conductance profiles for $PM_{2.5}$ samples collected on quartz fiber filters.

These different trends suggested that quartz fiber filters have a role in the electrical response likely due to their hydrophilic properties. Conversely, PTFE filters indicated that the obtained different profiles were due to electrical conduction of aerosols deposited on them. Thus, in order to investigate the aerosol phase transitions, PTFE filters were chosen as the best filtering substrate and it was used for further analyses.

2.4 Repeatability

The conductance measurements were repeated twice for 18 $PM_{2.5}$ samples collected on PTFE filters. In Figure 13 it is shown an example of a sample exposed to two RH cycles. After the first one, the air within the AEC was kept constant at 30% RH for 1 h before starting the second cycle.

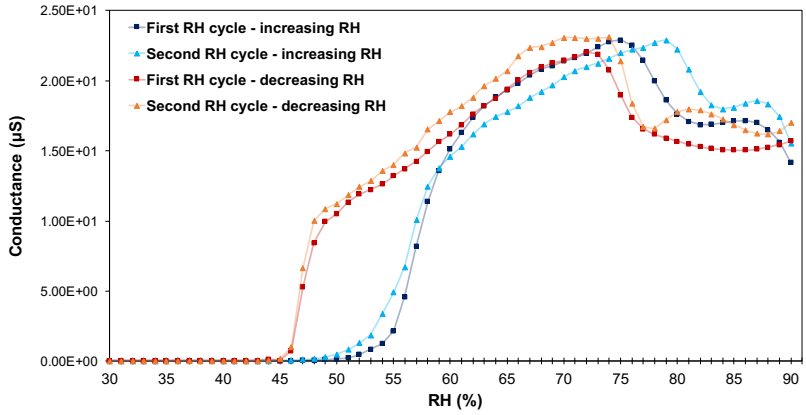

Figure 13 Repeatability test for conductance profiles.

The profiles highlighted a good repeatability of the measurements until the conductance values reached the maximum. On the other hand, Figure 13 shows that at high RH conditions, the electrical signal decreased with the increase of RH. This effect was observed for 25.9% of the profiles (i.e. 51 samples, considering the whole data set of samples). A possible explanation could be that a conductive electrolytic solution was formed on filter (suggested by high conductance values) and high RH conditions lead to its dilution. In fact, the continuous water condensation brings to a continuous dilution of ions that at the end leads to an electrical conductance decrease as well. This behavior is reported also in Anderko and Lencka(1997)[88] and in Gregor et al. (1960)[89].

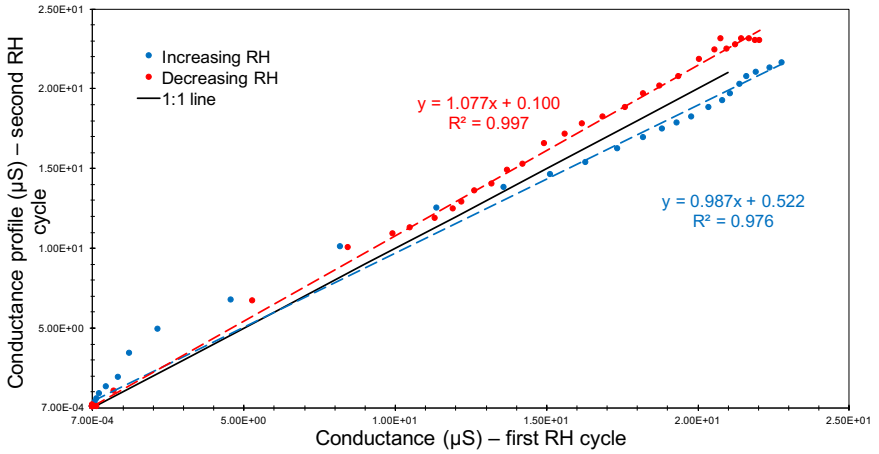

Figure 14 Correlation of conductance values between repeated RH cycles.

Figure 14 shows the correlation between the conductance measurements for the two cycles during both increasing and decreasing RH ramp below 75% RH. High R^2 values and slopes close to 1 indicate that the conductance measurements are repeatable.

2.5 Phase transition identification and repeatability

The conductance profiles were used to estimate the RH conditions of solid to liquid transition and *vice versa*. This method considers the variation of the electrical signal: when an electrolytic solution develops on a non conductive surface it is expected an increase in conductive properties of the media, i.e. PTFE filter + $PM_{2.5}$. On the contrary, a re-crystallization of a solution has the effect of suppress the electrical signal.

Thus, when RH is ramped up within the AEC, a sharp growth in electrical conductance measured implies that the WS compounds forming the deposited aerosols pass from a solid to liquid phase, i.e. deliquescence occurred. Similarly, an abruptly decreased in conductance during the reduction of RH suggests the crystallization of the WS fraction.

These simple principia were used by other authors as review in Chapter I, Sect. 4. On the other hand, atmospheric aerosols investigated in this work did not provided clear and unique DRH and CRH points. As it is shown in Figure 15 and Figure 16, the sharp variations in conductance occur within RH ranges. For this reason, when a phase transition process was identified, three RH values were used to characterized the transition ranges: the RH point in which the dramatic change in conductance was firstly detected, the ending change point and the RH in which the first derivative value reached the maximum. Concerning the deliquescence range, the three points were called DRH_{start}, DRH_{end} and DRH_{grad}. The last one was so called in order to indicate the identification by means of the gradient method. Similarly, the crystallization range was identified using CRH_{start}, CRH_{end} and CRH_{grad}. It is necessary to point out that $CRH_{start} > CRH_{end}$: this is because the crystallization transition occurs when RH is decreasing.

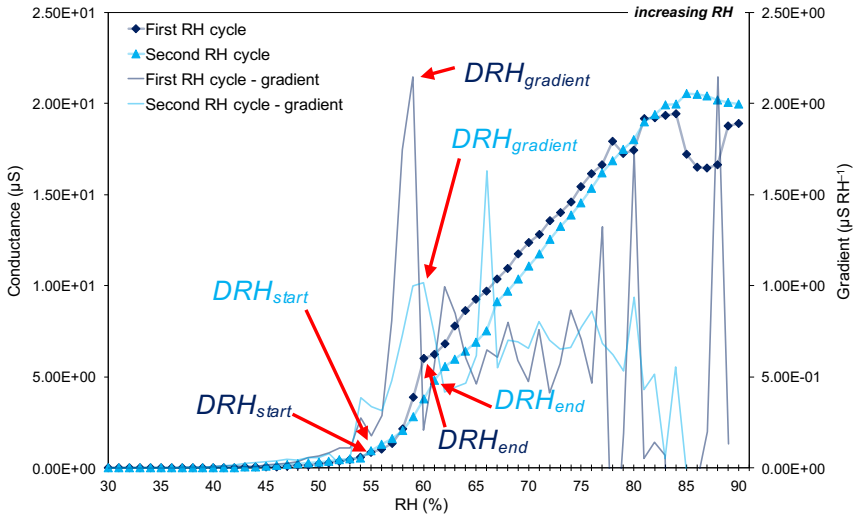

Figure 15 Deliquescence relative humidity by means of the conductance method.

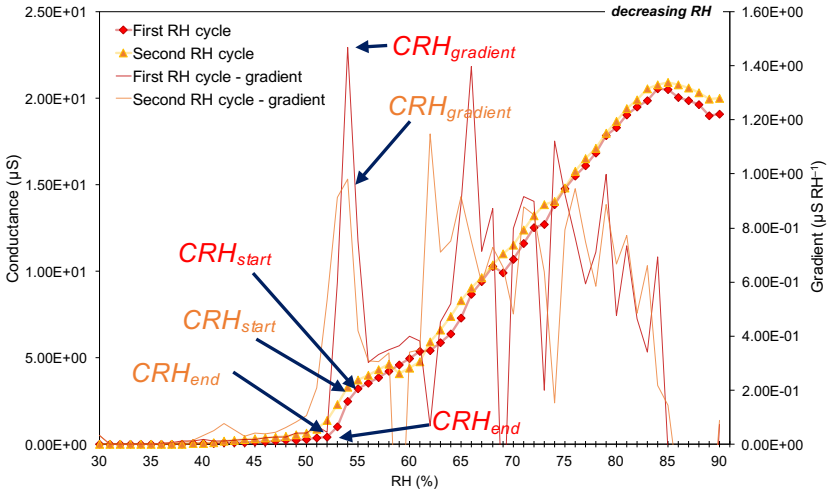

Figure 16 Crystallization relative humidity by means of the conductance method.

Figure 15 and Figure 16 show a RH cycle repeated twice for a sample. As it is clearly showed, both DRH and CRH ranges for the two RH cycles were found to be repeatable. In fact, the abrupt growth in conductance was detected within 56 – 60% RH range for the first cycle and within 56 – 62% RH for the second cycle. The gradient method showed that DRH gradient occurred at 59% RH during the first cycle and at 60% RH during the second one. Similarly, CRH range was identified between 55% RH and 52% RH (first cycle) and within 54 – 51% RH conditions (second cycle). The gradient method provided a value of 54% RH for both the cycles.

With the method described in this section, a conductance profile (and gravimetric, see Paragraph 2.6) is able being divided in three regions. Concerning the increasing ramp, below the DRH range, the sample adsorbs moisture and this weakly increase the electrical signal; then, when an abrupt increase in conductance is recorded, the solubilisation of WS compounds occur: this is the deliquescence range. Further increase in RH within the AEC causes a further increase in electrical conductance, therefore a hygroscopic region is observed. The reverse behavior is seen when RH is reduced: firstly, an evaporation period occurs, then a sharp decrease in conductance indicates a reducing mobility of charges due to crystallization of WS compounds: this is the crystallization range. Finally, the weak decrease in signal is associated to the late desorption of water caused by the slow diffusivity due to highly viscous organic compounds (as it will discuss in the later).

2.6 Comparison between conductance and gravimetric method for DRH and CRH

In order to validate the results provided by conductance method, a gravimetric method was also used for a sub-dataset of 20 $PM_{2.5}$ samples.

The half filter destined to the chemical characterization was previously exposed to an RH cycle within the AEC. The sample was housed in the vessel of Sartorius SE-2F precision weighing balance, which was placed inside the AEC. When the RH was changing, the vessel was kept open in order to allow the interaction of aerosols with the air and its moisture level. Once the target RH was reached, the vessel was closed and the mass measurement was obtained.

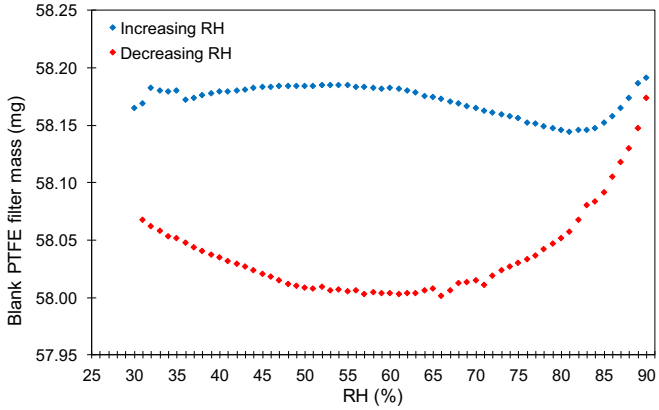

Figure 17 PTFE filter mass in function of RH.

Firstly, the gravimetric behavior of a blank PTFE filter was obtained exposing it to a RH cycle (Figure 17). A hysteresis in gravimetric profile was observed between the values during increasing and decreasing RH conditions. In order to take it into account, a correction factor was estimated in function of RH condition and of the RH ramp. This was calculated as the ratio of the measured mass at a target RH and the one obtained at 30% RH.

An example of gravimetric corrected profile is shown in Figure 18. This sample was collected during winter 2014 and the measured $PM_{2.5}$ fraction accounted for 1.755 mg. The increase in RH caused a weak growth in weight of the sample due the moisture adsorption caused by the hygroscopic properties of aerosols deposited on filter (green crossed markers). At 45% RH, the increasing rate growth as also shown by the gradient profile (green line). Thus, the range 45 – 53% RH was considered as DRH. Above this range, the hygroscopic growth became barely exponential and sample mass increased up to 2.637 mg. Thus, the mass increased more then three times due to hygroscopicity. Similarly, the weighting balance recorded a reduction in mass measurements during the drying of the chamber (yellowish cross markers). The water evaporation decreased the sample mass in a very similar way of the exponential increasing mass during the humidification. At 47% RH, the decreasing rate increased with a maximum at 46%

RH down to 43% RH. This range (47 – 43% RH) was assigned as CRH range. Below this range, mass values did not reach the corresponding values of the humidification curve. This fact was attributed to the effect of the organic matter.

Many authors[90–94] pointed out the effect of glassy and highly viscous organic matter in timescales water desorption within the particle bulk. For example, Shiraiwa and co-authors[91] studied the timescale partitioning for an aerosol system consisting in a α-pinene secondary organic aerosols (SOA) core-shell and an $(NH_4)_2SO_4$ aqueous core. The authors found that the SOA-rich phase is liquid above RH≥80%, semi-solid within 30-80% RH and semi- solid or amorphous solid below 30% RH. The time needed to reach the equilibrium is on the order of minutes below 90% RH but increased with the decrease in RH. Indeed, the timescale was estimated to be on order of hours to days below 40% RH, depending on bulk diffusivity. Mikhailov[92] and other authors[95] showed a gradual continuous growth (diminish) due to increase (decrease) in RH on aerosols systems containing hydrophilic organic compounds. Thus, the presence of water within the bulk organic matrix was supposed below the CRH.

This paragraph showed an example of a comparison between a gravimetric and conductance profiles applied to the same $PM_{2.5}$ sample, while a comparison between the results extended to the whole 20 samples dataset is provided in Chapter III, Section 2.5.

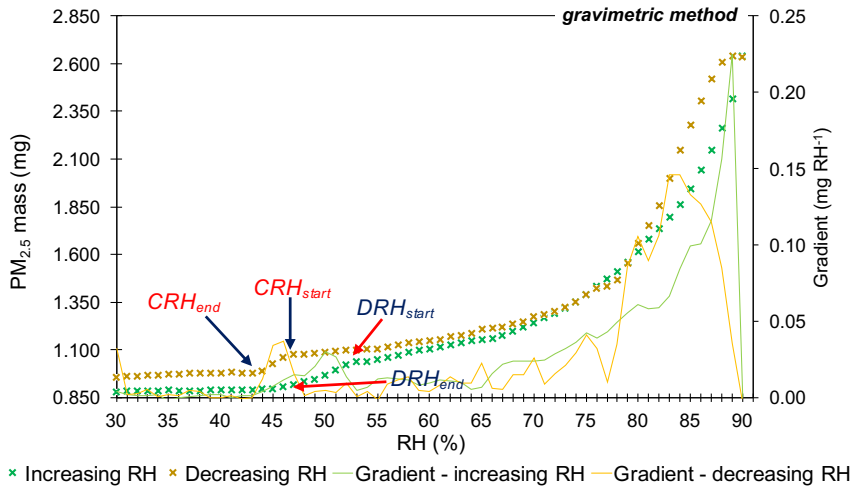

Figure 18 Example of $PM_{2.5}$ mass profile in function of RH conditions.

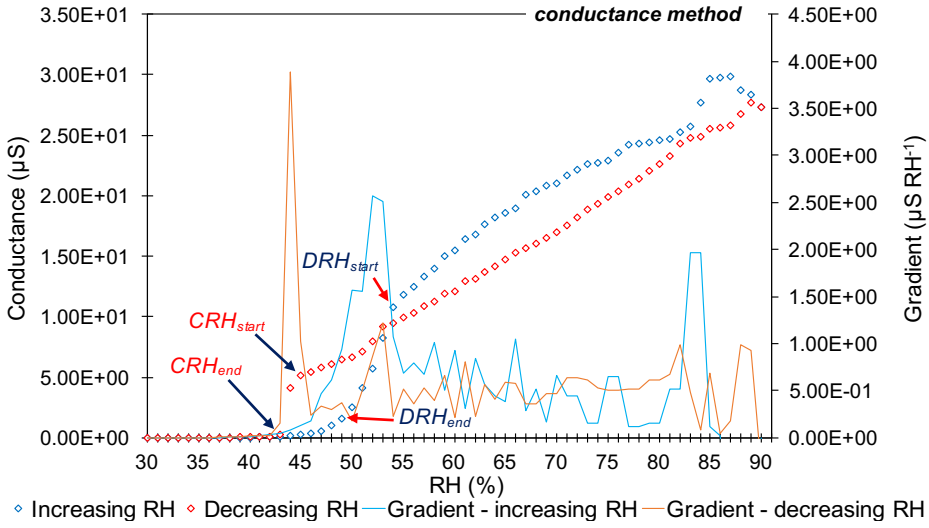

Figure 19 Conductance profile of the sample showed in Figure 18.

3 – Conclusions

In this chapter, the reliability of both conductance and gravimetric methods is descripted and demonstrated for real atmospheric aerosol samples. These methods provide easy interpretable results of the relative humidity at which deliquescence and crystallization occur. In the present

work, these methods are used for $PM_{2.5}$ fraction but it can be applied to different fractions as well. It is necessary to highlight that the obtained results are those due to the interactions of thousands of chemical compounds which form the real atmospheric aerosols. Because of this, it can be assumed that these methods characterize the hygroscopic behavior of an internally mixed aerosols.

Although the gravimetric method allows to measured the water mass gained by the aerosols samples (Chapter III, Sect. 2.6) leading to an estimation of the mass hygroscopic growth factor (Chapter IV), the conductance method results to be the preferred one. In fact, the RH cycle lasts about 4 h 30 min and for each RH cycle only one gravimetric profile could be performed. On the contrary, the conductance method allows to record the behavior of 6 aerosol samples at time, reducing the time needed to create a broad dataset. For these reasons, only 20 gravimetric profiles were carried out.

CHAPTER III – SEASONAL BEHAVIOR OF $PM_{2.5}$ DELIQUESCENCE AND CRYSTALLIZATION IN MILAN (PO VALLEY)

1 – SEASONAL $PM_{2.5}$ CHEMICAL COMPOSITION

Aerosol chemical variability was investigated (Chapter II, Sect. 1.4) for inorganic WS compounds (F^-, Cl^-, NO_3^-, SO_4^{2-}, PO_4^{3-}, Na^+, NH_4^+, K^+, Mg^{2+} and Ca^{2+}) and mono- and di-carboxylic acids (acetate, formate, propionate, glutarate, succinate, maleate and oxalate).

Firstly, the aerosols samples clearly showed a great variability in chemical composition between the cold and the warm seasons, i.e. winter (WI) and summer (SU), respectively. Similarly to it was already stated by many authors[96–98], three ionic species account for 88±1% (% weight/weight) of the WS fraction (NH_4^+, NO_3^- and SO_4^{2-}). NH_4^+ is the most abundant cation species and it is responsible of the neutralization of the negative charges, mostly represented by NO_3^- and SO_4^{2-}. Whereas the percentage amount of NH_4^+ remains almost unchanged between WI and SU seasons, NO_3^- and SO_4^{2-} presents an opposite trend due to the different thermodynamic conditions of the boundary layer. In fact, it is well known that NH_4NO_3 (AN, ammonium nitrate) and $(NH_4)_2SO_4$ (AS, ammonium sulfate) are mainly two secondary inorganic aerosols: they are formed by neutralization of $HNO_{3(g)}$ and $H_2SO_{4(g)}$ due to $NH_{3(g)}$[2]. While preferentially ammonia reacts with sulfuric acid, an excess of its it leads to react with nitric acid. On the other hand, the reaction equilibrium is affected by T and RH and particle-phase is promoted at low T and high RH conditions[99–101]. For these reasons, during WI the thermodynamic air conditions and high NO_x emissions – coupled with high air stability that avoid emissions dispersion – allow a prevalence of AN particle-phase in respect of the gaseous one. On the contrary, higher T and lower RH promote the evaporation of AN. The consequences of this are low AN concentrations in particle-phase during SU and high concentrations of that during WI.

In Figure 20 and Figure 21 are summarized the results of chemical characterization highlighting the seasonal variability. As previously discussed, nitrate ions represented the highest WS fraction (22.4±3.1%) in respect of sulfate (6.3±1.2%) and ammonium (8.0±0.9%) during WI (Figure 20a). On the opposite, during SU seasons sulfate prevailed (16.0±1.6%) in respect of nitrate (3.9±1.1%) and ammonium (6.9±0.7%).

Spring (SP) and fall (FA) can be defined as transitional seasons[102]: this is due to the fact that thermodynamic conditions are driven from a cold (warm) to a warm (cold) season, therefore T shows an increasing (decreasing) trend (Figure 22). A trend in temperature of the lower layers of the troposphere causes a trend in mixing height. From WI to SU, the mixing height shows an

increasing trend with a consequent increase in air dilution and lower aerosols concentrations. At the same time, the increase in temperatures promotes the gaseous-phase of AN. In addition, high fluctuations in ambient parameters (such as RH, rainfall, wind, etc.) can occurred affecting aerosol concentrations and chemical compositions. For these reasons, as it was expected, during SP and FA seasons nitrates and sulfates amounts reflect the transitional behavior, showing a nitrate/sulfate mass percentage ratio between those of SU and WI (Figure 20b). The 19% (4/21) of the chemically analyzed FA samples gave a ratio less then 1, whereas 60.6% (20/33) SP samples showed a ratio < 1. Thus, it is difficult to define a characteristic behavior – neglecting high fluctuations – as it is possible for WI (ratio>>1 for 93.2% of the samples) and SU (ratio<1 for 92.2% of the samples) and the chemical composition can be days-to-days associated to a similar WI or to a SU composition.

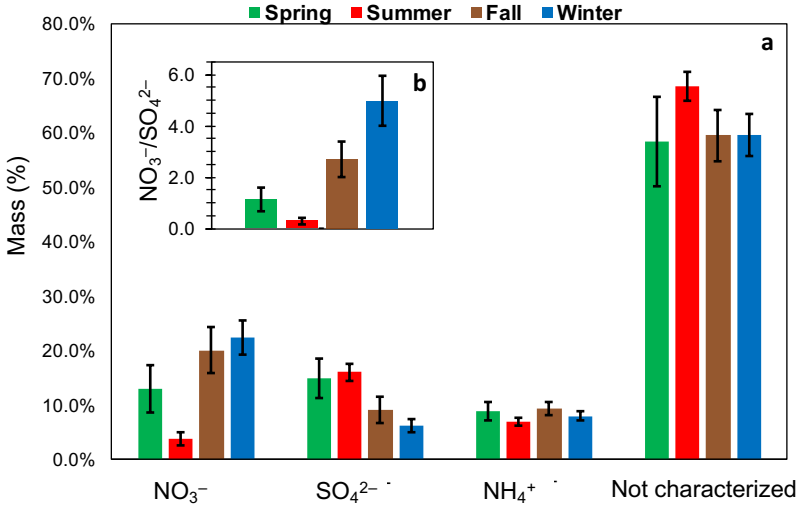

Figure 20 Seasonal variability of the main components and not characterized fraction expressed in percentage weight/weight. In panel (b) the nitrate/sulfate ratio is highlighted for the four seasons. The error bar represent the interval confidence (α=0.05).

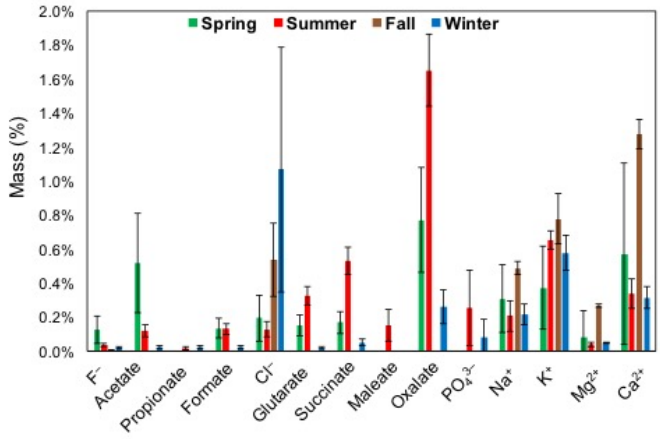

Figure 21 Seasonal averaged chemical composition of minor inorganic compounds and organic acids.

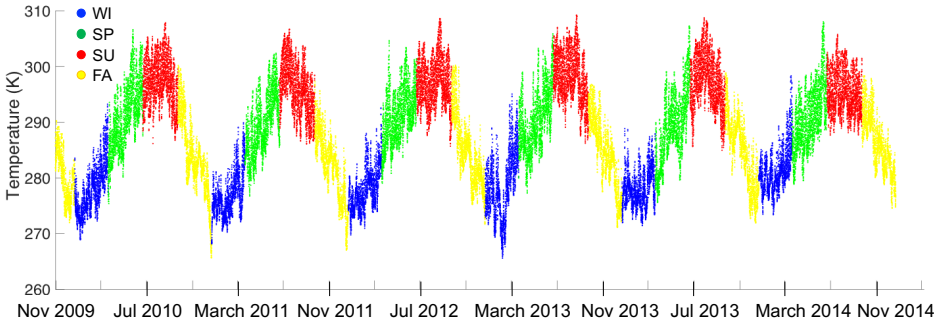

Figure 22 Air temperature data from 2006 to 2014 provided by ARPA (Regional Agency for Environmental Protection) Lombardia in Milan.

2 – SEASONAL DRH AND CRH

The phase transitions RH, i.e. DRH and CRH, were identified by means of the conductance method described in Chapter II. In addition, the gravimetric method (Chapter II, Sect. 2.6) was applied on a sub-dataset of 20 samples.

In this section, conductance and gravimetric profiles are shown for samples collected during winter (WI, Sect. 2.1), summer (SU, Sect.2.2). For spring (SP) together with fall (FA) seasons (Sect. 2.3) no gravimetric profile was performed. Finally, a discussion of the dependence of DRH and CRH on chemical variability is provided in Sect. 2.4.

2.1 Winter samples

Figure 23 reports a typical WI conductance behavior at increasing and decreasing RH for WI $PM_{2.5}$ sample (dry PM mass = 3.134 mg). The main feature is the sharp increase in conductance (from 0.94 µS up to 19.13 µS) in the region 51-59%. According to many author[57–59,61,76] and to the method presented in Chapter II, such a sharp increase is attributed to the dissolution processes of the water-soluble compounds. The gradient method showed that the DRH point can be assigned at 56.0% RH. A similar sharp increase in the aerosol mass (Figure 24) was observed within the 50-61% RH range. Before and after the DRH region, both the conductance and mass showed important features too that are described here below.

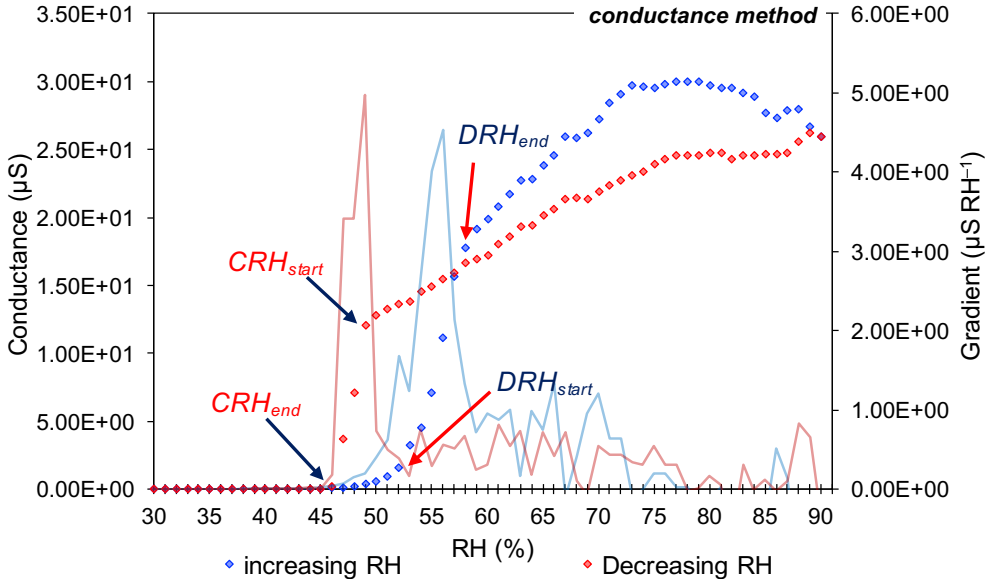

Figure 23 Conductance profile of a wintertime sample.

Before the DRH, the conductance signal weakly increased in the humidity range 30-50% RH. This growth of the electrical signal was attributed to an early absorption of moisture, as observed by Yang et al. (2006)[57], as also confirmed by the gravimetric measurements.

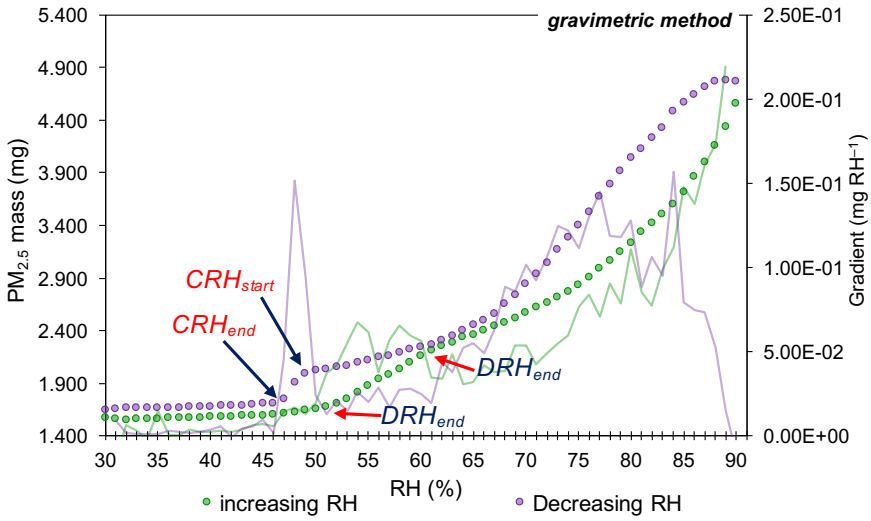

Figure 24 Gravimetric profile of a wintertime sample.

Above the DRH range, within the hygroscopic growth region, a further increase of both conductance and mass signal was observed due to the continuous condensation of water on the $PM_{2.5}$ samples. Whereas the mass gain rate increased after the DRH region, the conductance rate slowed and then weakly decreased. This behavior was attributed to the dilution of the electrolytic solution (Chapter II, Sect. 2.4)

During the dehumidification phase, water evaporation occurred and a decrease in the mass of the sample was observed from 90% to 51% RH. Similarly, conductance measures showed firstly a gradual decrease until 50% RH. Then, a sharp decrease for both conductance and mass was registered leading to the CRH range. The conductance dropped from 12.02 µS to 0.23 µS in the 49-46% RH range, which indicates the crystallization process. According to these findings, Figure 24 points out that the same crystallization range (50-47% RH) was shown by the gravimetric profile.

2.2 Summer samples

The following figures shows the behavior of a typical SU $PM_{2.5}$ sample (dry PM mass = 1.975 mg) for both conductance (Figure 25) and mass (Figure 26). The conductance profile showed first an early water uptake in the 30-63% RH range, characterized by a very low conductance increase. Starting from 64% RH, the conductance signal showed a rapid growth until 69%. DRH was defined as the RH with the maximum gradient: 68% RH.

During the decreasing RH ramp, a hysteresis behavior was observed as well. At first, the conductance signal decreased according to the hygroscopic part of the humidification profile,

then, within the 62-56% RH range, a significant drop in conductance occurred. The gradient method showed a maximum rate at 60% RH, that was identified as the CRH.

According to the conductance profile, a very weak mass increase was recorded up to 64% RH followed by a deliquescence region within the range 65 – 71% RH (Figure 26). The gradient method indicated that maximum occurred at 70% RH, weakly higher than it was found by the conductance profile (68% RH). Above the deliquescence range, further increase in RH exponentially increased the measured mass due to the hygroscopic growth of the aerosols. Conversely, ramping down the RH, an abrupt decrease in mass was recorded within 62 – 55% RH, perfectly in agreement with what was observed by means of the conductance methods, the CRH point was identified at 60 % RH.

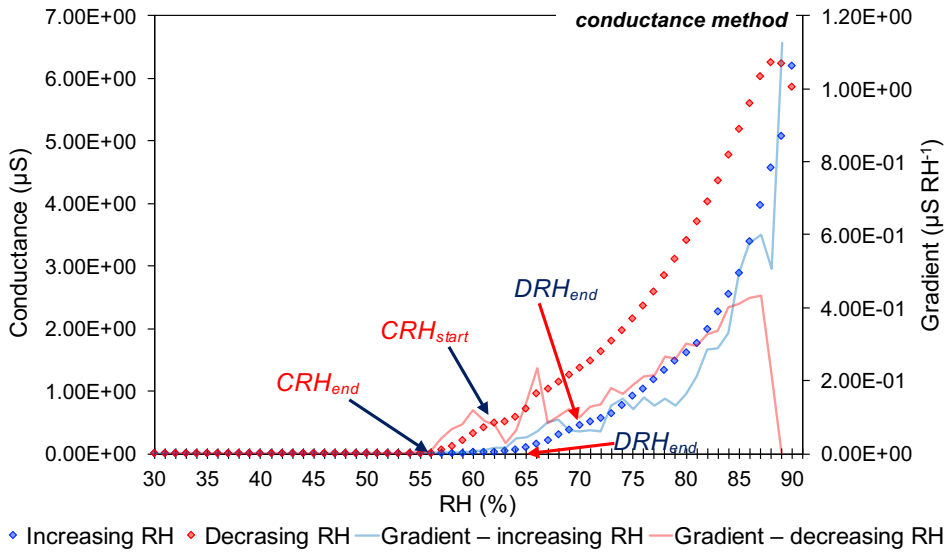

Figure 25 Conductance profile of a summer sample

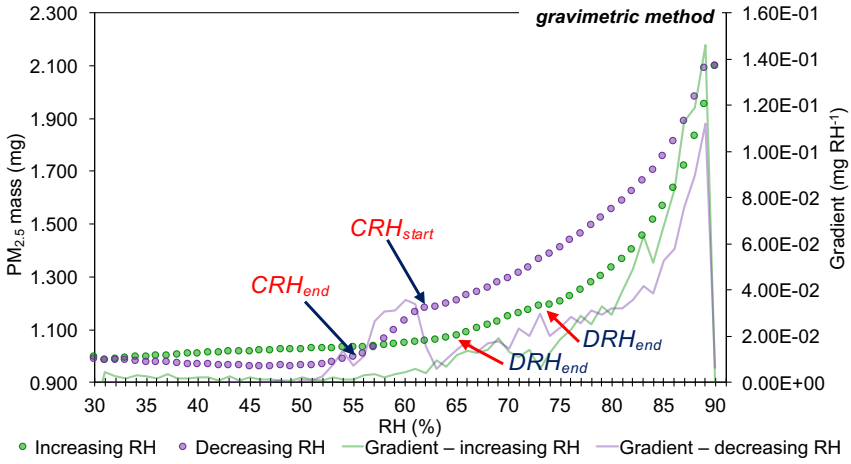

Figure 26 Gravimetric profile for a summer sample.

2.5 Spring and fall samples

Concerning the two transitional seasons, few samples were analyzed, i.e. 7 for SP and 10 for FA. As already discussed in Section 1, due to the great variability in day-to-day air thermodynamic conditions, it is difficult to define a representative behavior of aerosols samples both in chemical composition and regarding the phase-transitions relative humidity. On the other hand, the data presented within this paragraph are able to showed that the SP and FA samples phase transitions RH are between the WI and SU ones.

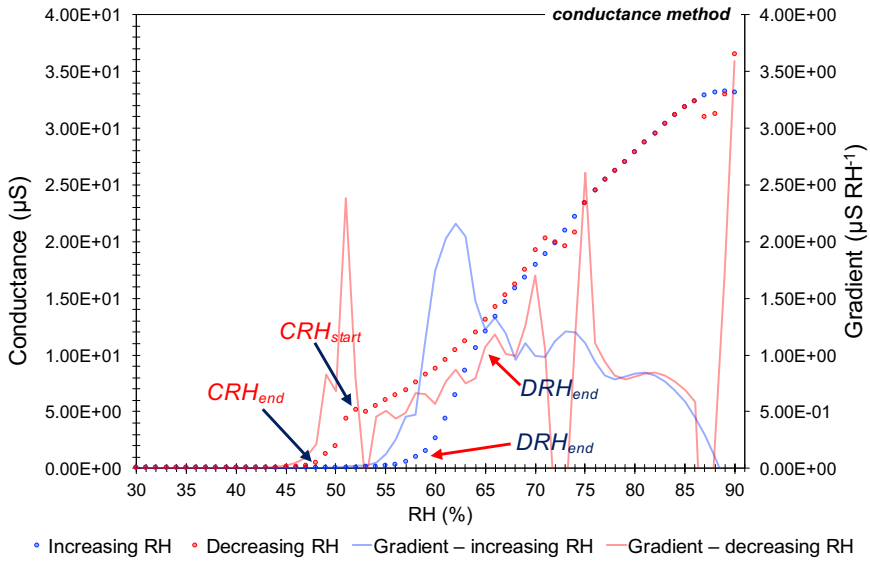

Figure 27 Conductance profile for a spring sample.

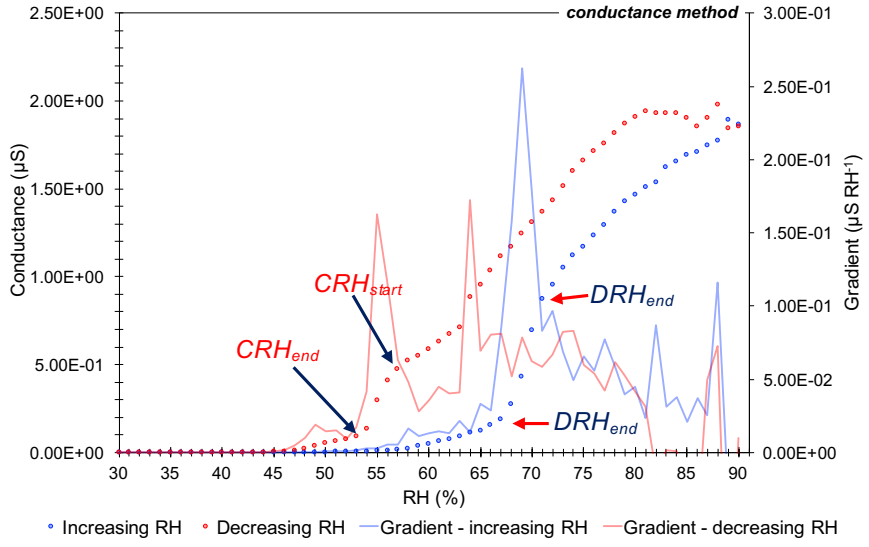

Figure 28 Conductance profile for a fall sample.

In fact, as it is shown in Figure 27 and Figure 28 for two examples of SP and FA profiles, DRH was observed within the range 56-63% RH for SP sample and 59-65% RH for FA one. Similarly, CRH for SP profile was identified between 53 and 50% RH and between 52 and 48% RH for FA sample.

SP and FA seasons are far from being exhaustively characterized. A chemical characterization carried out from the end of March, 2015 until the end of June, 2015 showed that, with important fluctuations, the nitrate/sulfate mass percentage ratio presented a decreasing trend in time. Thus, further analysis has to be performed. Nevertheless, the analyzed samples were chosen in order to temporally cover all over the SP and FA seasons. Therefore, the results shown in the present and in the following section can be considered as representative of the average behavior of aerosols within these seasons.

2.4 Seasonal behavior of DRH and CRH

The results of the DRH and CRH of aerosols collected as $PM_{2.5}$ are presented in function of the sampling season in Table 3. Firstly, the results show that DRH is always higher then CRH, confirming the hysteresis behavior of phase transitions for real atmospheric aerosols, as already found also in Martin et al. (2008)[72] and in other works. The hysteresis amplitude, considered as the distance between the RH values at which the two processes are completed (i.e. $DRH_{end} - CRH_{end}$), was estimated to be about 14% RH.

The lowest DRH was found to occur for WI samples whereas the highest one resulted for SU samples. As it was previously mentioned, SP and FA samples showed averaged DRH values and the same trend was also observed for the crystallization process (Table 3).

Despite the t test (α=5%) highlights that there is no statistical difference between the results obtained for the SP and FA seasons, DRH and CRH trends are in agreement with the ratio NO_3^-/SO_4^{2-} (% w/w), as it is stated in Table 4. This fact experimentally confirmed the influence of chemical composition of aerosol on the phase transitions relative humidity values.

Table 3 Seasonal DRH and CRH values identified by means of conductance method at 298 K.

		DRH_{start}(%)	DRH_{end}(%)	DRH_{grad}(%)	CRH_{start}(%)	CRH_{end}(%)	CRH_{grad}(%)
SP	mean	56.6	64.0	60.1	51.3	48.3	50.3
	$t_{(\alpha=5\%)}$	±1.3	±1.9	±1.6	±1.0	±1.4	±1.3
SU	mean	68.3	72.8	71.4	63.0	59.3	62.6
	$t_{(\alpha=5\%)}$	±2.1	±2.0	±2.1	±2.5	±2.7	±2.5
FA	mean	55.8	60.7	58.3	51.3	47.9	50.0
	$t_{(\alpha=5\%)}$	±2.1	±2.4	±2.1	±1.2	±1.3	±1.1
WI	mean	52.0	58.3	54.8	48.4	44.7	47.4
	$t_{(\alpha=5\%)}$	±1.5	±1.4	±1.4	±1.0	±1.2	±1.1

As it was already pointed out (Chapter I), DRH and CRH are affected by hygroscopic and hydrophobic compounds, both forming the atmospheric aerosols. In this work, the WS inorganic fraction mono- and di-carboxylic compounds were investigated only, therefore it is not possible to carried out a relation with the insoluble fraction and with other organic compounds. In this regards, it is well-known that organic compounds have a role in the overall hygroscopicity of atmospheric aerosols. Jimenez and co-authors (2009)[103] highlighted that the higher is the oxygen/carbon ratio of an organic compound, the higher is its hygroscopicity due to its higher polarity[104]. This suggests that organics can even reduce the overall water uptake in respect of a pure hygroscopic aerosols. Moreover, as it was pointed out in Shiraiwa et al. (2013)[91], semi-solid organic compounds decreased the bulk diffusion coefficient of water in the particle phases, especially at low RH conditions, leading to higher timescale of hygroscopic growth. The authors calculated the time for equilibration considering a core-shell aerosol composed by α-pinene and AS. For a electrolyte rich-shell, this time was estimated to be in the order of 10^{-5} s, whereas for a organic-rich shell this time can last up to 100 s for a 1 μm particle. This could partially explain the gravimetric profile showed in Figure 24. At RH conditions below the CRH, it was observed that the mass did not decreased at the value measured at the beginning of the RH cycle but remained at a fairly-constant mass distance of 0.10 mg. This means that at 30% RH, about 6% of the sample mass was due to water still absorbed.

This behavior seems different from the one found for the profile in Figure 25. In this case, the measured mass decreased below the mass measured at the beginning of the RH cycle at the end of the crystallization range and then came back to the starting value at 30% RH. Even with the correction factor calculated for the blank PTFE filter profiles, this effect was not sufficiently corrected. Although this effect does not invalidate the identification of the CRH range, the estimation of the massHGF (Chapter IV, Sect. 1) would be affected. For this reason, whenever this parameter resulted lower than 1, it was neglected.

Table 4 Average chemical composition of $PM_{2.5}$ samples, nitrate/sulfate ratio and degree of neutralization exposed to RH cycles. SP and FA samples not considered the organic acids.

		Chemical composition (% w/w)						Degree of neutralization	
		NH_4^+	NO_3^-	SO_4^{2-}	Other anions	Other cations	NO_3/SO_4^{2-}	slope	R^2
SP*	mean	10.2%	19.8%	11.0%	0.4%	1.1%	1.8	0.757	0.986
	±σ	3.4%	11.6%	4.4%	0.4%	0.5%	0.7	0.005	-
SU	mean	7.0%	4.2%	15.9%	3.5%	1.3%	0.3	0.900	0.834
	±σ	1.2%	2.7%	2.6%	0.9%	0.3%	0.3	<0.001	-
FA*	mean	10.4%	24.6%	7.9%	0.3%	1.0%	3.3	0.932	0.967
	±σ	0.6%	3.8%	1.6%	0.2%	0.2%	0.9	0.002	-
WI	mean	8.1%	24.6%	5.2%	1.2%	1.1%	5.9	0.916	0.960
	±σ	1.2%	4.7%	1.3%	0.3%	0.2%	1.6	<0.001	-

Table 4 shows the seasonal averaged chemical composition for the samples characterized for the phase transitions relative humidity only. The comparison between DRH and CRH with NO_3^-/ SO_4^{2-} confirmed the importance of these two ions: a high ratio leads to lower DRH and CRH. These seems in agreement with the data reported in literature for both pure AN and AS[40,52]. The first one deliquesces at 61% RH, a lower value in respect of AS which forms a saturated solution above 80% RH. Similarly, crystallization for AN was not reported even at very low RH[53,105] while CRH of AS is observed at 35% RH.

Potukuchi and Wexler (1995)[106] proposed a thermodynamic calculation for a H^+-NO_3^--SO_4^{2-}-NH_4^+ aerosol system considering the equilibrium constant between the crystal and the aqueous phases. Therefore, the sulfate fraction (Y) of the whole sulfate plus nitrate $Y=[SO_4^{2-}/(SO_4^{2-} + NO_3^-)]$ (Eq. 1.13), and the ammonium fraction (X) of the whole ammonium plus hydrogen $X=[NH_4^+/(NH_4^+ + H^+)]$ (Eq. 1.12) were calculated (Figure 29). Potukuchi and Wexler[106] pointed out that, for a given X, an increase in the Y (i.e., summer conditions) leads to higher DRHs, while for a given Y, a decrease in the X (acid conditions) leads to lower DRHs.

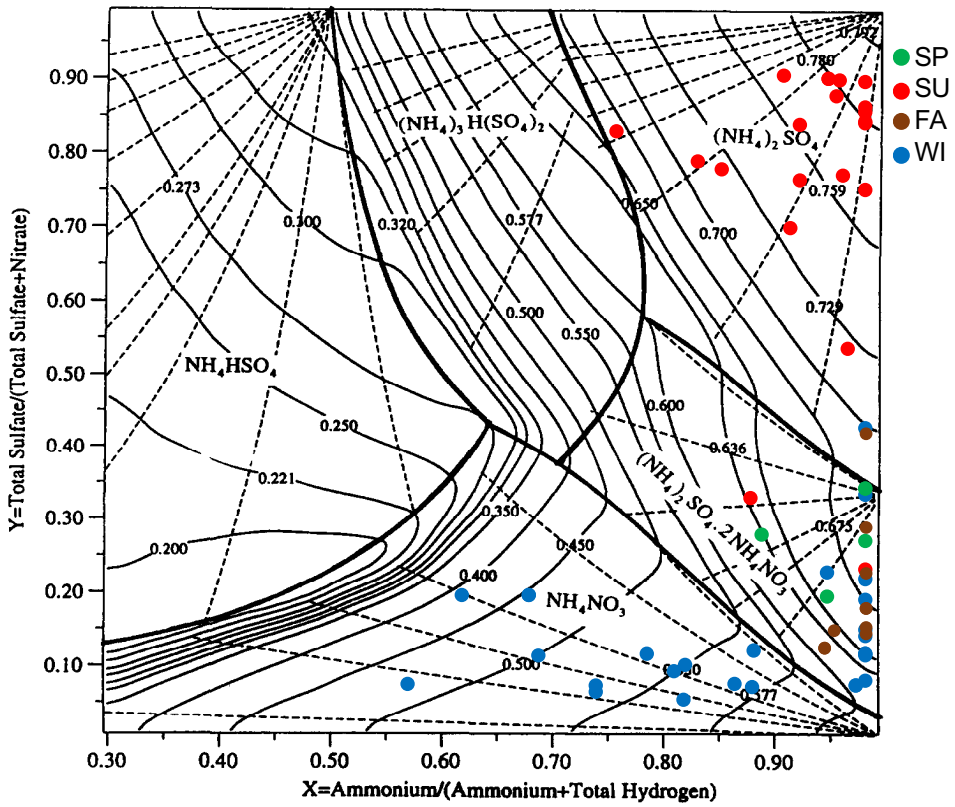

Figure 29 Chemical composition and DRH relation as proposed in Potukuchi and Wexler (1995)[106].

For WI aerosol, Y values were very low (0.13±0.03, average ± confidence interval at 5%) compared to SU (0.76±0.08) and, in addition to an almost complete neutrality evidenced by X (0.88±0.0.05 in WI), suggested that the prevalent salt species was similar to $2NH_4NO_3 \cdot (NH_4)_2SO_4$ and AN. Even here, this predominance in nitrate ions leads to lower DRH values if compared with SU ones. At the same time, Y for SP and FA seasons gives reasons of the intermediate results obtained for DRH (0.28±0.07 and 0.19±0.07 for SP and FA, respectively). Whereas the DRH trends are in agreement with the ones suggested by the Potukuchi and Wexler diagram, the experimental values are lower (except for the samples for which the charge neutrality was far, see Sect. 3). The reason of this is the simplified aerosol system modelled by Potukuchi and Wexler. As it was stated in Chapter I, the more the aerosol is complex in chemical composition the lower is the DRH[9,31,55,76,95]. A real atmospheric aerosol is formed by many compounds, thus a lower value of DRH was expected. A further comparison with a thermodynamic model, i.e. E-AIM II, is provided in Section 3.

Martin et al. (2003)[47] proposed an empirical model able to estimate the CRH of H^+-NO_3^--SO_4^{2-}-NH_4^+ particles (Chapter I). The domain of applicability is such that CRH(X,Y)≥1%. Thus, assuming X=1, this limit results in a minimum value of 0.25 for the Y parameter, whereas if Y=1, X has the lowest limit of 0.5. With this limitations, the algorithms reported by the authors were used to calculate the CRH.

Firstly, the method allowed the CRH estimation of 40% of the samples only. This because most of the WI and FA samples presents a Y parameter which is outside the domain of Martin's algorithms. In addition, conversely by the overestimation provided by Potukuchi and Wexler's diagram for DRH, Martin's algorithms underestimated the experimentally identified CRH in average of about 35% RH. This can be attributable to a lack of the consideration of the heterogeneous crystallization processes. Han and Martin (1999)[107] pointed out that the presence of metal oxides, such as Fe_2O_3, TiO_2 and ZrO_2, in the aerosol's particles can affect the CRH values, leading to an increase up to 32% higher compared to a pure saline aerosol because such oxides can act as crystallization nuclei driving heterogeneous nucleation. In this regards, historical data found in Perrone et al. (2012)[21] and Vecchi et al. (2004)[108] for both SU and WI seasons showed that heavy metals, mostly presented as oxides, are commonly present in atmospheric $PM_{2.5}$ fraction sampled in Milan, representing about 1% of the $PM_{2.5}$ mass. In this regards, as an indication only, an analysis carried out by means of energy dispersive spectrometer on a $PM_{2.5}$ sample revealed the presence of Cu, Zn and Fe.

Furthermore, the presence of organic material, such as glycerol or certain carboxylic acids, can also increase the aerosol's CRH[54]. Concerning the dataset used for the chemical characterization, the amount of organic acid was quantified at 2.9±0.4% of the mass for SU samples. In Po Valley, Decesari et al. (2001)[109] also found that WS organic compounds accounts for 38% and 50% of the total mass of organic carbon for WI and SU seasons, respectively, and the main fraction is represented by acidic compounds (mono- and di-carboxylic acids and polyacidic compounds). Therefore, an averaged gap between experimental CRH and calculated CRH of 32% RH seems to be explainable.

3 – EXPERIMENTAL AND E-AIM II DATA COMPARISON

The experimental results were then compared with the Extended-Aerosol Inorganic Model (E-AIM), module II by Clegg et al. (1998)[49] described in chapter I. This model allows to estimate the repartition at the equilibrium of the provided compounds among a solid-liquid-gaseous phases within a bulk system. As it was previously stated, a thermodynamic model is unable to predict the heterogeneous crystallization processes. Therefore, the comparison between experimental and modelled data was carried out for those obtained during the increasing RH ramp.

The E-AIM II model needs a condition of charges neutrality; therefore, a balance estimation was carried out (Eq. 1.9). The input database was built from a sub-dataset of 60 samples taking into account the mole amounts of the main inorganic ionic species (NH_4^+, NO_3^- and SO_4^{2-}). In order to obtain the charges neutrality, the excess of negative charges was compensated with H^+, therefore assuming that the balance is provided by the aerosol acidity. On the contrary, an excess of positive charges was corrected reducing the amount of NH_4^+. For WI and SU samples, the model was used both considering organic acids and inorganic ionic fraction only.

Table 4 suggests that most of the samples presented an excess of negative charges. For SU and WI samples, more than 60% of the inputs were corrected with an addiction of H^+, whereas for FA and SP this percentage amounts of less than a half.

The data provided by E-AIM II were used in order to identify the DRH by means of the increase in liquid water estimated within the aerosol bulk at different RH conditions and at fixed temperature of 298 K. The results are summarized in Table 5.

Data highlight that E-AIM II averaged estimations are able to model the trend of DRH observed (see Sect. 2.4), confirming that the main inorganic ionic ions (NH_4^+, NO_3^- and SO_4^{2-}) drive the conditions of deliquescence transition. On the other hand, except for DRH_{start}, which is sensitive to the presence of the added H^+ which act as strong acids, both the DRH_{end} and DRH_{grad} of the transition are overestimated by the model.

Table 5 Comparison among experimental DRH and estimates by E-AIM II model.

		DRH (%)								
		EXPERIMENTAL			E-AIM II (without organic acids)			E-AIM II (with organic acids)		
season		start	end	grad	start	end	grad	start	end	grad
SP	mean	55.8	64.7	59.7	54.5	68.3	65.8	-	-	-
	$t_{(\alpha=5\%)}$	2.1	3.6	2.8	16.1	5.4	5.4	-	-	-
SU	mean	67.4	72.3	70.6	56.0	77.1	72.9	55.5	75.1	72.7
	$t_{(\alpha=5\%)}$	2.3	2.1	2.6	3.6	1.6	4.6	4.8	2.5	3.4
FA	mean	55.6	60.4	58.0	56.8	67.1	63.9	-	-	-
	$t_{(\alpha=5\%)}$	2.7	2.7	2.5	7.1	2.2	2.2	-	-	-
WI	mean	51.2	57.8	54.0	45.4	62.2	58.8	44.4	62.6	60.3
	$t_{(\alpha=5\%)}$	2.3	2.2	2.1	5.6	3.4	3.7	6.1	3.1	3.2

This is also confirmed by the comparison between each sample, which highlights that a very low correlation it can established (Figure 30). The overestimations are due to the simplified

system considered by the model, similarly to what was already stated for the diagram proposed by Potukuchi and Wexler (1995)[106]. On the contrary, the experimental measurements are the results of the integrated interaction of the compounds forming the aerosol samples.

Again, even though the E-AIM model is able to fit the trend of the DRH changing the chemical composition of the aerosol system, its capability to predict the experimental DRH is still scarce.

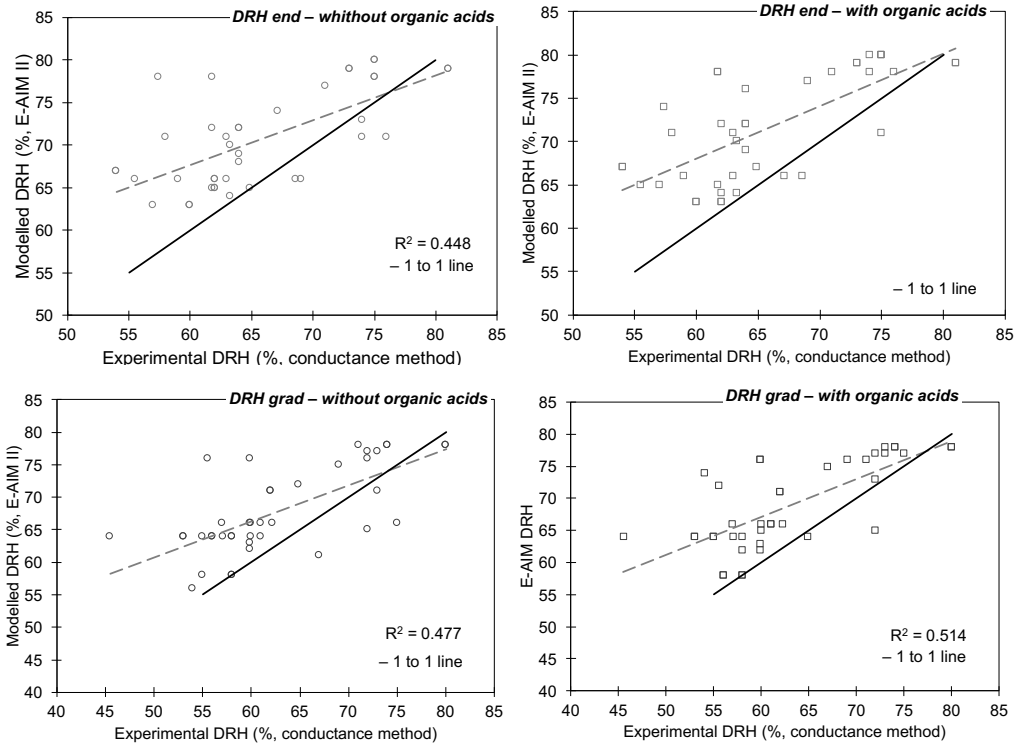

Figure 30 Comparison between experimental data and estimations by E-AIM II.

As it was discussed in the previous section, a sub-dataset of 20 samples collected during WI and SU seasons were used to compare the conductance method with another method which allows to take into account the same complexity of atmospheric aerosols. For this reason, as it was introduced in Chapter II, Sect. 2.6 and in Chapter III, Sect. 2 and 3, the gravimetric method was used.

Figure 31 provides the comparison between DRH and CRH obtained by means of gravimetric and conductance methods. The high determination coefficients (0.907 and 0.926 for DRH and

CRH, respectively) and the slopes coefficients close to 1 (0.937 and 0.834) confirm that the relative humidity of phase transitions provided by the two methods were in good agreement.

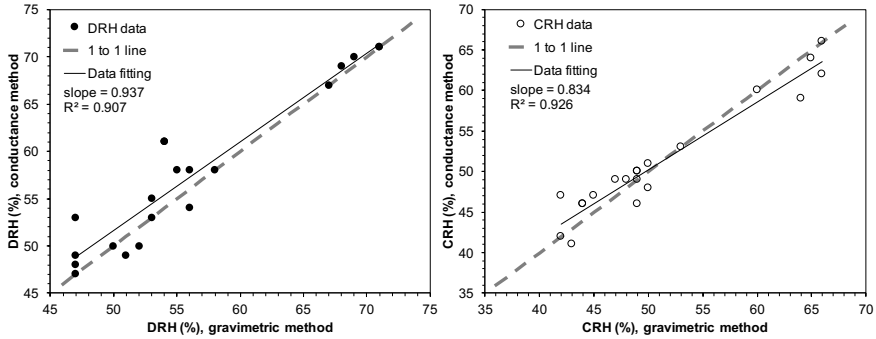

Figure 31 Relation between gravimetric and conductance method for both DRH (left) and CRH (right) values obtained by means of gradient.

The gravimetric method, in addition to the DRH and CRH, provided a profile of the increase (decrease) in water mass adsorption (desorption) on the considered aerosol samples as well. Direct comparisons with these measurements are provided by means of the E-AIM II. The averaged H_2O moles amount experimentally determined were compared with those estimated by E-AIM II and the results are shown in Figure 32.

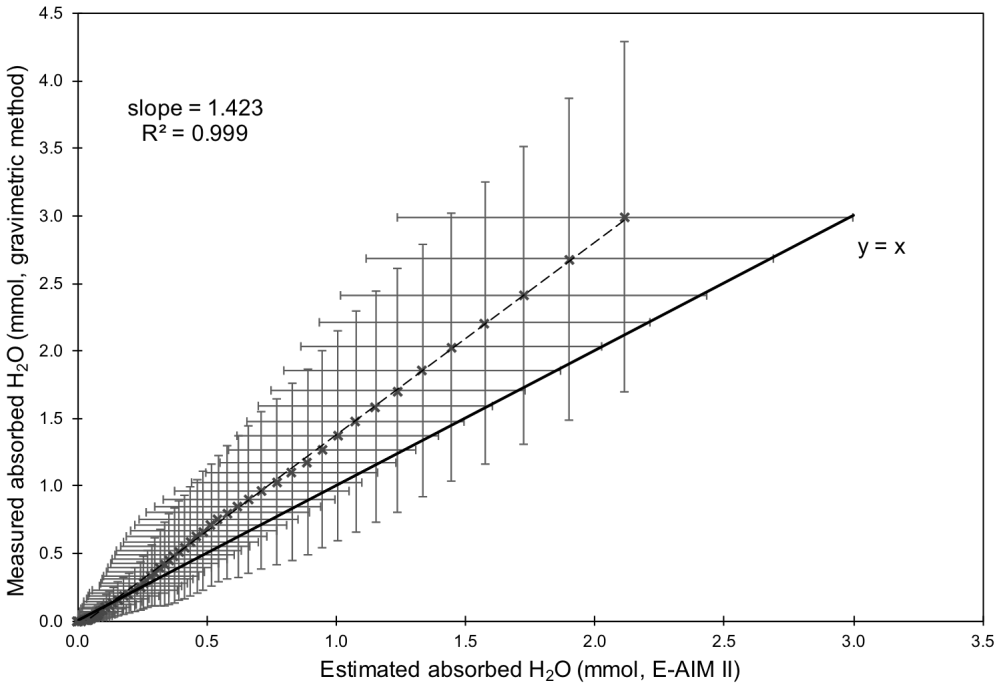

Figure 32 Comparison between adsorbed liquid water measured with gravimetric method and calculate by E-AIM II model.

Figure 32 shows that E-AIM II fits with the measurements provided by the gravimetric method (R^2=0.999) even though a clear underestimation of water content by 21% was found. These results are perfectly in agreement Khlystov et al. (2005)[102]. The authors carried out a measurements campaigns during summer 2001 in a urban park in Pennsylvania with a dry and ambient aerosol size spectrometer (DAASS) in order to estimate the volumetric growth factor and the water content of ambient aerosols. They also compared their results with those calculated by E-AIM. They found that the model underestimated their estimations on average by 36%. The authors attributed this underestimation to the lack of hygroscopic behavior of the organic fraction.

The comparison between experimental data and E-AIM model was also performed adding the di-carboxylic acids quantified by means of the ion chromatography. As it was expected, E-AIM performances did not improve. The underestimation could be also attributed to the lack of other ionic species neglected by E-AIM II models such as Na^+, Mg^{2+}, Ca^{2+} and Cl^-. On the other hand, their relative importance in the mass closure (Table 4), i.e. less than 5%, appeared to be insufficient to explain this disagreement all alone. Therefore, it is possible that other organic species could have an additional role in aerosol overall hygroscopicity. A number of WS organic

compounds was reviewed in Saxena et al. (1996)[110]. Other carboxylic acids, such as glyoxilic and citric one, in addition to polyols, amino acids, amines and other polar particle-forming compounds can absorb water and they overall behavior could be the reason of the underestimation. On the other hand, many compounds forming the atmospheric aerosols presents very low hygroscopicity. In this regards, many authors[68,111–113] had pointed out the role of a barely-hydrophobic or low hygroscopic fractions of aerosols. McMurry and Stolzenburg (1989)[113] suggested that atmospheric aerosols can be discerned into a hygroscopic and less hygroscopic modes. Virkkula et al. (2006)[112] indicated that secondary organic aerosols formed from monoterpenes oxidation as compounds responsible of a decrease in hygroscopic growth factor for a mixture organic/inorganic compounds in respect of pure inorganic salts. This means that the presence of compounds with a hydrophobic or low hygroscopic behavior can reduce the amount of water adsorbed by the aerosols. In conclusion, the thermodynamic models are far from correctly predict the overall hygroscopic behavior of real atmospheric particles.

4 – THE ESTIMATION OF THE HYDRATION TIME

As it was pointed out in Chapter I (Sect. 2), the hydration state of ambient aerosols alters a variety of atmospheric processes. Optical properties and the radiative forcing are differently affected by dry or hydrated particles[114] since condensed water changes their refractive index that becomes hygroscopic dependent because of the change in particles sizes, for example. In addition, many heterogeneous reactivity is enhanced in liquid phase and gas-particle partitioning of semi-volatile compounds is also facilitated[115]. The aerosols hygroscopicity can also promote stone decay (Chapter IV) and metal corrosion (Chapter V). In order to sufficiently predict many of these processes, one should known the conditions in which aerosols are in aqueous or solid phases. At very low and very high RH conditions these prediction would be easy, whereas at the most frequently air conditions (30-80% RH) this could be not. This is due to the presence of a RH range in which aerosols can occupy two possible states: a stable state in which they are solid and a metastable one, in which aerosols are in a supersaturated aqueous phase. This leads to the need in consider both DRH and CRH and the previous RH exposure conditions.

Some works was published in order to provide data about the hydration state of atmospheric aerosols. Rood et al. (1987)[116] performed light-scattering measurements in Riverside, California, during August and September 1983. They took into account the hysteresis behavior of the aerosols in order to estimate their physical states and they concluded that aerosols were hydrated during 86% of the time during their tests. In addition, the authors estimated that atmospheric aerosols exhibited a metastable state for 61% of the time while for 25% of it the RH was above the aerosols DRH. For the remaining time (14%), aerosols was concluded to be dry. Similar estimations were carried out in Santarpia et al. (2004)[71] in Texas where RH mostly ranged between 53% and 69% RH.

In this section, an estimation of the hydration time is proposed considering the aerosols phase transition relative humidity and the RH conditions experienced by the aerosols. Since any direct measurement is available in the Po Valley, same calculations were carried out. Firstly, the hydration time is estimated as Time of Wetness (TOW, Sect. 4.1) according to ISO 9223, a method commonly use in corrosion science[117–120] and cultural heritage climatology[121–123]. Then, the threshold considered in the TOW method (i.e. 80% RH) was substituted (Section 4.2) with the seasonal DRH experimentally measured and discussed in Section 2.4. A further step is reached considering the hysteresis loop, therefore introducing the experimental CRH (Sect. 4.3). The last estimations (Sect. 4.5) consider the temperature-dependence of the phase transitions processes (Chapter I, Sect. 2.1.1) that is modeled by means of the E-AIM II (Sect. 4.4).

4.1 – Hydration time as the Time of Wetness according to ISO 9223

The ISO (International Standard Organization) 9223 defines the Time of Wetness (TOW) as the total time in which the RH of the ambient environment is equal or higher than 80% at temperature above 273.15 K. This practical definition based on the ambient parameter of the surrounding air is commonly used to estimate the time in which surfaces are wet, thus chemical reactions can occur and enhance their decay. Because of this, TOW is used as descriptor of the risk induced by ambient conditions and pollutants in corrosion science and cultural heritage climatology[117,124–126].

Thus, in order to estimate the time in which aerosol WS compounds are in a liquid phase, the ISO 9223 method is here firstly presented as the percentage of hours for each seasons.

1-hour time-resolved meteorological data of temperature and RH were retrieved by Regional Agency for Environmental Protection (ARPA-Lombardia) meteorological stations and concerned the air conditions in Milan for 2006-2014 period.

With TOW method, the hydration time was simply estimated only identifying the hours in which T>273.15 K and RH≥80%. Therefore, atmospheric aerosol physical state can be discerned in two classes: dry and hydrated.

In Figure 34, 1-year (from 23/03/2013 to 22/03/2014) of RH data are shown as example. The blue-colored markers represent the RH in which aerosols are in a hydrated state while red-colored ones identify the dry state. The black-colored markers represents the conditions at T≤273.15 K.

As it is clearly shown Figure 34a, TOW method considers that aerosols are in wet state for very few time. In particular, during SP only 19.6% of the hours presented the demanded conditions to classify aerosols as hydrated. This percentage is reduced to 9.6% during SU while increases to 46.7% and 40.8% for FA and WI seasons, respectively, although T≤273.15 K occurred for 2.3% (FA) and 8.2% (WI).

4.2 – Hydration time with experimental DRH

As many authors[117,127–130] pointed out, the surfaces can be hydrated far below 80% RH because of their hygroscopicity and the aerosols deliquescence. Thus, aerosol DRH is used to substitute the RH threshold showed in the previous discussion. Here, the hydration time was evaluated considering the seasonal variability in DRH due to the different chemical composition of atmospheric aerosols. In order to estimate this parameter, aerosols were considered hydrated from the conclusion of their deliquescence transitions, i.e. from DRH_{end} (see section 2.4).

Figure 34b represents the aerosols physical states on the basis of the seasonal experimental DRH. This clearly shows that hydration time drastically increases for every seasons: 39.1%, 16.4%, 75.7% and 68.0% for SP, SU, FA and WI, respectively. It is important to take into account that T≤273.15 K conditions are considered as different classes (2.3% for FA and 8.2% WI). Even if it is well-known that the presence of electrolytes can significantly lower the freezing temperature due to vapor pressure depressing, in this discussion no assumption is done regarding the aerosols phase below 273.15 K.

4.3 – Introducing hysteresis: hydration time with DRH and CRH

Deliquescence and crystallization experimentally determined at 298 K are here considered in order to introduce the effect of the hysteresis of phase transitions on the aerosols physical states. Therefore, five different conditions can be now discerned. In addition to the cases in which air temperature is below than 273.15 K, when RH is below or equal than CRH, aerosols are in a dry state. Then, if the ambient RH increases and overcomes the CRH but it is lower than DRH, aerosols are still in a dry state but they are within the hysteresis loop RH range (in the lower stable branch) and this condition is discerned from the previous one. When RH≥DRH, aerosols deliquesce and they are hydrated until the RH comes back to the aerosols CRH value. On the other hand, when RH decreases from RH≥DRH to a RH condition that is still higher than CRH, aerosols are again within the hysteresis loop but a supersaturated solution is still presented (upper metastable branch). In these latter cases (CRH<RH<DRH), the aerosols are still considered as hydrated until RH does not reach the CRH_{end} value (see Table 3). In order to discern these cases, it is fundamental to take into account not only the instantaneous RH conditions but also the previous ones.

These five cases are discriminated within the calculations and presented in Figure 34c. Here, in addition to black, red and blue markers, yellow and cyan ones identified the two cases within the hysteresis loop: yellow for the lower stable branch and cyan for the upper metastable branch.

Whereas the fourth case (RH≥DRH), which correspond to the hydration time reported in the previous paragraph, remains unchanged, the overall hydration time now increases due to the contribution of the metastable upper branch of the hysteresis loop, which accounted for 10.5% during SP season, 5.4% for SU, 7.6% for FA and 7.0% during WI.

4.4 – Modelling temperature–dependence of DRH and CRH

In Chapter I, the temperature–dependence of DRH and CRH was discussed on the basis of the available literature. Whereas a thermodynamically derived equation was proposed by Tang and Munkelwitz (1993)[39] and Wexler and Seinfeld (1991)[43] for DRH, no algorithm was provided for the T–dependence of the crystallization transitions. In addition, few data are available about the effect of temperature on the CRH but some authors[44–46,56] suggested a negative relation between temperature and crystallization point similar to DRH one.

The E-AIM II was firstly used in order to to estimate seasonal DRH in function of T, then the DRH T-dependence was evaluated. With this aim, the seasonal averaged mass percentage of NH_4^+, NO_3^- and SO_4^{2-} were related to 1.000 mg of aerosol inorganic ionic fraction and used as input for the model. The E-AIM II was used to scan the increase in liquid water moles adsorbed on the input aerosol system scanning from 274.15 K to 328.15 K. For each temperature and season, the DRH ranges were identified and a good linear correlation were found between the two parameters of interest (Figure 33).

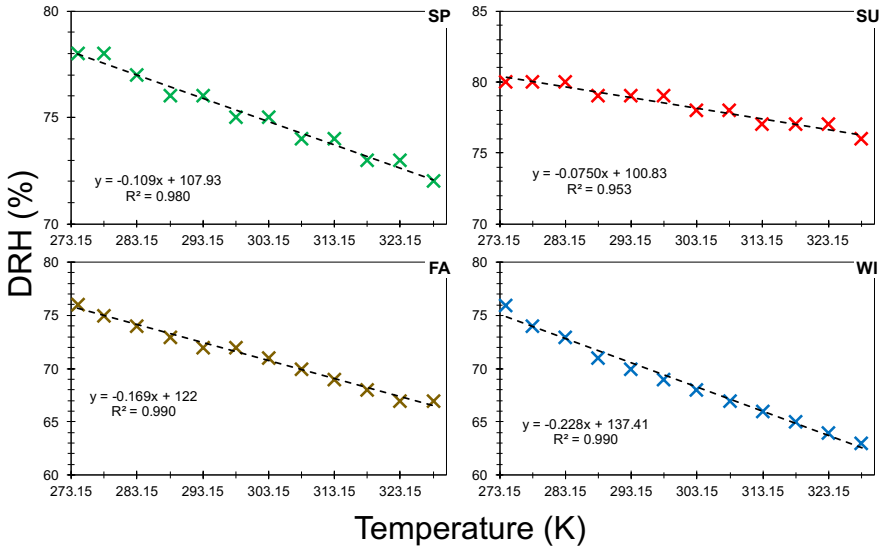

Figure 33 Temperature–dependence for seasonal DRH derived by E-AIM II model.

The fitting equations were then adjusted in order to pass through the experimental DRH values found at room temperature. For this reason, while the slopes of the curves were kept constant, the intercept were decreased. Again, it was assumed that CRH has the same T-dependence of the DRH, therefore to retrieval a relation valid for CRH, intercept value was further reduced and the fitting line was forced to pass through the experimental points.

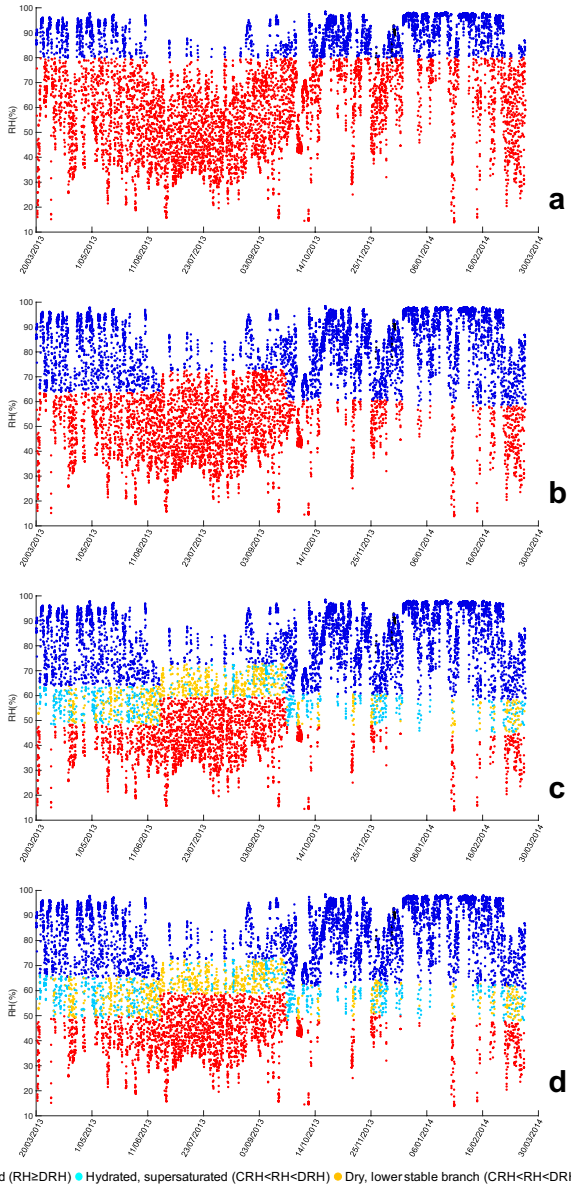

Figure 34 Atmospheric aerosols physical states in Milan estimated by means of: (a) time of wetness, (b) seasonal DRH threshold, (c) considering experimental DRH and CRH determined at 298 K and hysteresis, (d) considering T-dependence of both DRH and CRH.

4.5 – Hydration time considering temperature-dependence

Finally, an estimation of the hydration time due to the aerosol $PM_{2.5}$ fraction deliquescence and crystallization is here provided considering the effect of temperature on the DRH and CRH values. Therefore, the phase state of aerosols depends on the season and temperature as well and are shown in Figure 34d.

Table 6 summarizes the results of this calculation discerning the parameters for each seasons. As it is pointed out, for all seasons a decrease in averaged temperature in respect of the reference one, i.e. 298 K, leads to an increase in DRH and CRH. On the other hand, while the average DRH and CRH for SU are almost unchanged (72.8% RH and 58.8% RH, respectively), due an average temperature (296.9 K) close to the reference one, the transitions humidity for WI increased almost of 10%. This is very interesting since the T-dependence of both DRH and CRH seems to partially compensate the effect of the seasonality in chemical composition of the aerosols.

Table 6 Averaged seasonal parameters: meteorological, experimental phase transition relative humidity and T-dependent DRH and CRH.

season		RH (%)	T (K)	DRH (%, 298 K)	CRH (%, 298 K)	DRH (%, T)	CRH (%, T)
SP	mean	58.2	290.4	64.0	48.3	65.3	49.5
	±σ	21.3	5.6	-	-	0.6	0.6
SU	mean	54.8	296.9	72.7	59.3	72.3	58.8
	±σ	17.7	4.4	-	-	0.3	0.3
FA	mean	74.9	284.2	60.7	47.9	62.7	49.9
	±σ	18.7	5.8	-	-	1.0	1.0
WI	mean	73.5	278.9	58.3	44.7	63.1	49.6
	±σ	21.0	4.4	-	-	1.0	1.0

As it was expected, the increased in both DRH and CRH for every season leads to a decrease in hydration time in respect of the estimations provided in the paragraph 4.3, except for SU seasons that results almost unchanged (from 21.8% to 22.0%). In addition, this decrease mainly involves WI seasons since the increase in transitions humidity is higher. In fact, the hydration time decreases from 75.0% (Sect. 4.3) to 70.4% of the total wintertime hours. The remained seasons show a weak decrease in the hydration time, i.e. 47.0% and 81.8% for SP and FA, respectively. For all the seasons, the reduction of the hydration time is manly due to a decrease of the frequency in which the RH conditions are above the DRH.

The results separated in respect of the five conditions, expressed in averaged seasonal hours, are summarized in Figure 35. The graphs show that, using the atmospheric aerosols phase

transition relative humidity, the hydration time strongly increases in respect of the ISO 9223 method, i.e. as the time of wetness. This in not only due to the decrease of the upper threshold but also because of the consideration of upper metastable branch of the hysteresis loop in which aerosols are still presented as liquid phase. On the other hand, the considered T-dependence of DRH and CRH appeared to not drastically affect the estimation of the hydration time in respect of the consideration of the experimental values obtained at 298 K, except for the WI seasons in which averaged hydration time decreased approximately of 92 h.

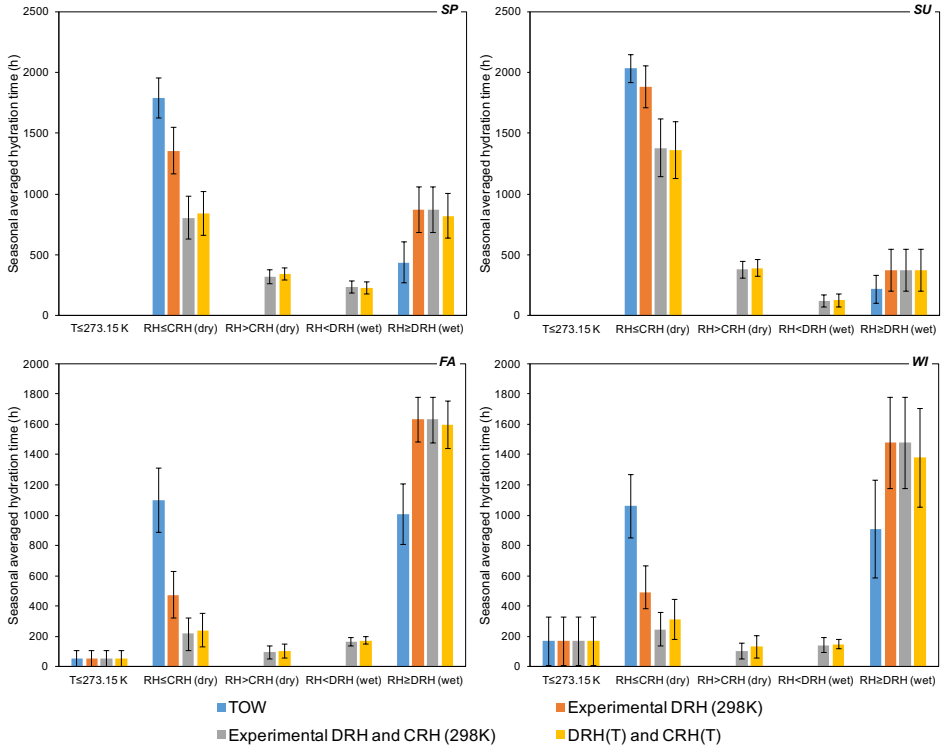

Figure 35 Seasonal hydration time with the described four methods.

5 – CONCLUSIONS

In the present chapter, atmospheric aerosols phase transitions are shown and discussed in relation to the seasonal variability affected by the chemical compositions one. The experimental activity, which was carried out at room temperature (i.e. 298 K), highlighted that the DRH occurs at higher RH in respect to CRH. The hysteresis amplitude, meaning the distance between the RH at which the transitions end, was estimated to be about 14%.

The atmospheric aerosols sampled during WI seasons present the lower DRH and CRH at 298 K: deliquescence resulted to occur within the range 52.0±1.5% – 58.3±1.5% RH while CRH between 48.4±1.0% RH and 44.7±1.2% RH. On the opposite, during the warmer seasons, i.e. SU, DRH was identified in the 68.1±2.1% – 72.7±2.0% RH range and CRH between 63.7±2.2% RH and 60.1±2.3%. Comparing these results with the chemical composition of the inorganic ionic fraction, which typically accounts among 30-40% (w/w) of the mass of the samples, the trend of the phase transitions RH agrees with the trend of the ratio between NO_3^- and SO_4^{2-}: in fact, the prevalence of nitrate ions lowers both DRH and CRH and high amounts of nitrate are common for the WI samples (ratio 5.9±1.6). On the contrary, high amount of sulfates, typical for the SU samples (ratio 0.3±0.3), increases the phase transitions relative humidity. Concerning SP and FA seasons, DRH and CRH occur between the transition of WI and SU. Again, NO_3^-/SO_4^{2-} ratio for SP results 1.8±0.7 and DRH and CRH occur at higher RH (56.6±1.3% – 64.0% RH and 51.3±1.0% – 48.3±1.4% RH, respectively) in respect of WI, whereas FA samples (ratio 3.3±0.9) occurs among the SP and SU, i.e. 55.8±2.1% – 60.7±2.4% RH range for DRH and 51.3±1.2% – 47.9±1.3% RH range for CRH.

The experimental data are then compared with estimations provided by Potukuchi and Wexler (1995)[106] and E-AIM II model by Clegg et al. (1998)[49] for the DRH, both considering a simplified system composed by NH_4^+, NO_3^- and SO_4^{2-}, the main ionic species forming the samples collected in Milan. Both the estimations provide DRH values higher in respect of those experimentally identified. On the other hand, the trends predicted by them are in line with the trend showed by the real aerosol samples, suggesting the key role of NH_4^+, NO_3^- and SO_4^{2-} which drive the deliquescence. Therefore, the discrepancies found is ascribed to the role of the other chemical compounds which low the DRH.

Concerning the crystallization process, the experimental results were compared with those calculated by means of the empirical algorithm proposed by Martin et al. (2003)[47]. The limitations of this model avoid to carry out the estimations for the WI and FA samples because their chemical composition is out of the algorithm domain. Instead, the calculations for SU and SP results in lower CRH respect of the experimental ones. Again, this is imputable to the simplified system which mainly not consider the role of organic compounds and of insoluble inclusions which are known to act as nuclei for heterogeneous crystallization.

Finally, a discussion about the hydration time of the aerosols was provided. This it is of great importance since aerosols can affect many processes both when they are suspended within the atmosphere (clouds formation and light-scattering, therefore visibility and radiative forcing) and when they contaminate surfaces (such as corrosion of metals and stone decay), and their behavior can drastically change in function of their physical state. The hydration time was estimated proposing four step of complexity, from a single high RH threshold to T-dependent hysteresis.

Data demonstrated the importance in consider both DRH and CRH in order to calculate the hydration time and to predict the aerosols physical state.

CHAPTER IV – IMPLICATIONS OF AEROSOLS PHYSICAL STATES

In this chapter the effects of the aerosols hydration states are taken into account in order to show their implications in some fields. The estimation of the hygroscopic growth factor and the implications for remote sensing data retrieval (Sect. 1) are discussed in D'Angelo et al. (2016)[74] in a paper submitted on *Atmospheric Research*. On *Aerosol and Air Quality Research*, Casati et al. (2015)[75] applied the estimation of the hydration time with the aim to develop two parameters able to support the risk assessment of stones in cultural heritage climatology field.

1 – THE EFFECTS OF HYSTERESIS ON THE REMOTE SENSING DATA RETRIEVAL ALGORITHM

The interaction of atmospheric aerosols with solar radiation is strongly affected by their hygroscopic behavior. As mentioned in Chapter I, water uptake changes the optical properties of aerosol particles – therefore their scattering and light absorption efficiency (direct effect on climate). In addition, aerosols can also act as cloud condensation nuclei and their hygroscopicity affects the size of the cloud droplets, impacting on the cloud albedo and on their lifetime (indirect effect). Because of these, the hygroscopic behavior of atmospheric aerosols is a topic of great interest.

Usually, the hygroscopicity is described by means of the hygroscopic growth factor (HGF), which allows to indicate the ability of the particles to attract and adsorb air moisture on their surface and bulk. The HGF is calculated as the ratio of the particle dimension at the target RH on the dimension at RH<40%. Typically, the HGF is expressed at high RH conditions, such as 85% or 90% RH.

The gravimetric method provides a mass HGF (massHGF) of a broad size range of particles, i.e. $PM_{2.5}$ for what concerns this work. Two examples of hygroscopic growth are shown in Figure 36 for a WI (left) and SU (right) samples. At 90% RH, the averaged measurements indicate that WI aerosols showed a massHGF of 2.76±0.06, larger if compared with the SU ones, whose massHGF was 1.91±0.11.

The majority of data presented in literature are provided by means of the hygroscopic tandem differential mobility analyzers (HTDMA). Even if many designs of this instrument exist, the HTDMA are based on an extraction of a narrow size cut from a dry polydisperse aerosols. Then, this is exposed to a target RH and then a determination of the increased in particles diameter is carried out. The difference in diameter is due to the water uptake: therefore, the ratio of the increased diameter on the original one is the HGF[131], here indicates as sizeHGF in order to specify that is a ratio based on the measurement of the particles diameter.

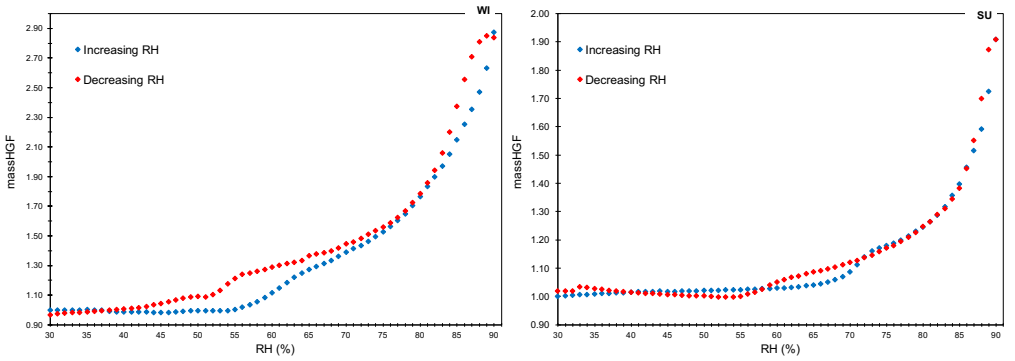

Figure 36 Hygroscopic behavior of WI (left) and SU (right) samples.

Because of this discrepancy in nature of the results, an estimation of the sizeHGF is here provided. This calculation was carried out assuming particles as spheres with an average dry density of 1.5 g cm^{-3} (as in Seinfield and Pandis, 2006[2]) and under an internally mixed scenario since every chemical components affected the measured massHGF from which the sizeHGF was derived. The internal mixing (due for example to the ageing of particle in the atmosphere) was demonstrated by several observations conducted in the past over the investigated site[23].

Within these assumptions, the sizeHGF – expressed as the ratio between particle diameter at ambient RH and at dry condition – was calculated from massHGF inverting the following algorithm:

$$massHGF(RH) = \frac{m}{m_0} = \frac{\rho d^3 \frac{\pi}{6}}{\rho_0 d_0^3 \frac{\pi}{6}} = \frac{\rho_0 d_0^3 + \rho_w (d^3 - d_0^3)}{\rho_0 d_0^3} = 1 + \rho_0^{-1} \left(\frac{d^3}{d_0^3} - 1 \right)$$

Thus:

$$sizeHGF(RH) = \sqrt[3]{\rho_0 (massHGF - 1) + 1} \qquad \textit{(Eq. 4.1)}$$

Where:

m = particle mass [g] at ambient RH

m_0 = particle mass [g] at dry condition

ρ = particle mass density [g cm^{-3}] at ambient RH

ρ_0 = particle mass density [g cm^{-3}] at dry condition

ρ_w = water density (1 g cm^{-3})

d = particle diameter at ambient RH

d_0 = particle diameter at dry condition

The calculations provided a sizeHGF at 90% RH of 1.54±0.01 in WI and 1.33±0.03 in SU. The HGF trends are in agreement with the DRH values discussed in chapter III. In this respect, lower DRH observed during WI turn into wider hygroscopic growth regions which generally range from DRH up to 100% RH. Thus, the hygroscopic growth in WI starts earlier (in terms of

RH) with respect to SU, a condition able to promote a larger condensation of water when considering the same absolute RH.

Higher WI sizeHGF in respect of the SU ones were also found by Kamilli et a. (2014)[132] in Paris for submicrometric particles. The authors found variability in sizeHGF depending on different chemical compositions, especially nitrate, sulfate and organic compounds. In their work, averaged sizeHGF were measured at 1.27 for SU samples and 1.35 for WI (RH=90%, 285 nm), and these values are both lower if compared with the measurements presented in this work but the same trend affected by nitrate-enrichment for WI samples and sulfate-enrichment for SU samples was found. Within the Po Valley, Bialek et al. (2014)[96] carried out a sampling campaign at San Pietro Capofiume (44°39'0'' North, 11°38'0'' East, near Bologna, Italy) in SU 2009. They observed a diurnal variation of aerosol water uptake: in early morning sizeHGF (at 90% RH) reached the lowest values (1.18 for 35 nm particles and 1.38 for 165 nm particles), while a gradually increase in sizeHGF was observed during the day (1.32 and 1.46 for 35 nm and 165 nm particles, respectively, in the early afternoon). At the same sampling site in November, Svenningsson et al. (1992)[133] used a TDMA and distinguished two hygroscopic modes at 85% RH: a less hygroscopic one (sizeHGF=1.10±0.07) and a more hygroscopic one (sizeHGF=1.44±0.14) were observed.

Although the seasonal trends are in agreement, the results obtained by gravimetric method on $PM_{2.5}$ cannot directly compared with the data available in literature because of the different methodology of investigation, especially because of the aerosols size range studied.

Both the hygroscopic growth curves showed in Figure 36 highlighted that the phase transitions hysteresis affects the growth factor. The importance in taking into account this behavior was discussed for radiative forcing modelling in many paper[114,128]. Wang and co-authors (2008)[134], modeled the physical state of an ammonium-sulfate aerosol system building on data reported in Martin (2000)[40] in the boundary layer. The authors estimated that comparing a scenario in which hysteresis is considered and 66% of aerosols are in aqueous phase, the omission of the upper metastable branch leads to an overestimation of the solid phase of +22% whereas the opposite case, i.e. neglect of the lower stable branch, increases the aqueous phase of +11%. These evaluations were further improved in Wang et al. (2008)[135] in which global anthropogenic sulfate direct radiative effect was estimated to increased of ~4% when aerosols in hysteresis loop were always considered in the upper branch, and decreased of ~8% in the opposite case in respect of a full consideration of the hysteresis loop. In an earlier paper, Martin et al.[114] estimated a difference in radiative forcing of 24% if a simple sulfate-nitrate-ammonium aerosol system is considered in the upper or in the lower branches of the hysteresis loop with clear sky (clouds absence).

Radiative forcing is strictly affected by the optical properties of aerosol particles. The interactions between light and aerosols is therefore modeled with three main parameters: aerosol optical depth (τ), single-scattering albedo and the phase function. The first is the magnitude of

the light that is scattered and absorbed by the aerosols within the vertical column (top-of-atmosphere – ground): in other words, it is the attenuation of the light-intensity through the atmosphere. The single-scattering albedo allows to compare the relative importance between scattering and absorption, i.e. the ratio between scattering and extinction coefficients. The last parameter (phase function) represents the scattered intensity at a given direction in respect of the integral of the scattered intensity at all directions.

Since aerosol optical properties depends on the size of the aerosols, their hygroscopicity is usually taken into account in order to estimate the previous mentioned parameters at given ambient conditions and their overall effects. In particular, it is well-known that aerosols concentrations decreased along the vertical profile and the main contribution is given within the mixing layer.

In this regards, Levy et al. (2007)[136] showed a simple algorithm to estimate the $PM_{2.5}$ concentrations within boundary layer:

$$[PM_{2.5}] = \frac{\rho}{\Delta Z_{PBL} HGF} \tau M'_c \qquad \textit{(Eq. 4.2)}$$

where: ρ is the aerosol density, ΔZ_{PBL} indicates the thickness of the boundary layer, τ is the aerosol optical depth and M'_c is a mass conversion coefficient. As highlighted in Barnaba et al. (2010)[137], the hysteresis can also strongly affect data comparison of aerosol optical depth by remote sensing (LIDAR) measurements and *in situ* aerosol concentrations. This is due to the fact that aerosols concentration is usually derived from the sampled particles mass measured by gravimetric analysis at 50% RH (according to EN-14907), while remote sensing measurements are carried out at ambient RH. This is consistent with the findings showed in Chapter III, since the gravimetric method showed that at 50% RH aerosols can be on the upper metastable branch of the hysteresis loop, therefore they still contain water when exposed to decreasing RH conditions. Consequently, the presence of liquid water adsorbed on the aerosols would increase the estimates of their concentration at ground level. Thus, a correct parameterization of HGF is needed.

For WI aerosols the lower branch region of the humidograph occurred on average in the range 44.7-52.0% RH, and the massHGF was estimated as 1.02±0.03. The upper branch of the hysteresis region was on average between 48.4% and 58.3% RH. Since the average estimated massHGF was 1.25±0.02, omission of the metastable branch causes an underestimation of the massHGF up to 23.2±0.8%. Similarly, for SU aerosols, the average massHGF of the upper branch of the hysteresis loop (63.7-72.7% RH) was 1.39 while, for the lower branch (60.1-68.1% RH), was 1.15±0.06, with a mean error of 21.1±1.8%.

Considering these massHGF values within the hysteresis region and using Eq. 4.2 to estimate the $PM_{2.5}$ concentrations, the percentage overestimation of these calculated $PM_{2.5}$ concentrations was calculated with the Eq. 4.3 (indicated as $\Delta[PM_{2.5}]$%), and it resulted to be of 18.9±0.7%

during WI and of 17.4±1.4% during SU when aerosols are in the upper branch (metastable states) of the hysteresis loop.

$$\Delta[PM_{2.5}]\% = \left(\frac{massHGF_L}{massHGF_U} - 1\right)\% \qquad \textit{(Eq. 4.3)}$$

In Eq. 4.3 $massHGF_U$ and $massHGF_L$ are the averaged massHGF in the upper and lower branch of the hysteresis loop, respectively.

An estimation of such an error magnitude is of great interest in order to compare τ provided by remote sensing method (such as ground based LIDAR or satellite sensors like MODIS) with $PM_{2.5}$ concentrations at ground level. As reviewed by Hoff and Christopher (2009)[138], while the precision of the measurement of τ is ±20%, the accuracy of the estimation of $PM_{2.5}$ concentration from τ is order ±30%. Therefore, the opportunity to improve the satellite data retrieval could be supplied by a better parameterization of the HGF within the algorithms.

The estimation of the hydration time (Chapter III) was again used in order to evaluate the frequency of the wrong assignments. In this regards, the temporal range was reduced to consider the hydration state of aerosols in Milan when TERRA and AQUA satellites – equipped with MODIS sensors (Moderate Resolution Imaging Spectroradiometer) – pass above Po Valley, i.e. from 10 a.m. to 2 p.m..

During WI seasons, the meteorological conditions (65.3±22.4% RH and 280.5±4.6 K) facilitated the hydrated state of aerosols. In fact, the hydration time was estimated at 76.2% if the experimental phase transitions RH were considered, while 70.2% of the time if the temperature-modelled DRH (62.7±1.0% RH) and CRH (49.2±1.0% RH) values were used. Conversely, the drier SU conditions (44.4±14.2% RH, 299.9±3.8 K) and the higher DRH and CRH values suggested a prevalence of dry states for aerosols. In SU seasons, the hydration time was estimated at 10.1% of the time with experimental DRH and CRH and 10.2% with those modelled (72.1±0.3% RH and 58.6±0.3% RH, respectively).

A further calculation allows to estimate the time in which the RH conditions are within the hysteresis loop. These occurred for 19.9% and 5.9% (or 19.9% and 6.1% with temperature-modelled phase transitions) of the cases for WI and SU seasons, respectively. Therefore, a very low occurrence of conditions affects the data retrieval algorithms during the warm seasons. On the other hand, when aerosols are within the hysteresis loop they are mostly hydrated: for WI seasons, aerosols are on the upper metastable branch for almost 95% of the time while for SU this percentage decreased only to 85%.

This means that without a correct parameterization of the HGF, the algorithms are not able to estimate the $PM_{2.5}$ concentrations at ground level for the majority of time in which RH conditions are within the hysteresis loop RH range.

2 – APPLICATION IN HERITAGE CLIMATOLOGY

In the last decades, a growing attention on the role of atmospheric particles contaminations on materials weathering was given. Many authors[139–141] stated that PM can cause damage to both indoor and outdoor stones and its effects have an increasing relative importance due to the reduction in acidic gaseous pollutants such as SO_2[142–144].

In this regards, a key role in stone decay is attributed to the aerosols hygroscopicity. The presence of liquid water can trigger some weathering processes such as dissociation and solid-liquid reactions, acid attacks, penetration of salts solutions in the media porosity and biological activities which can further enhance these processes. These "chemical" decay mechanisms are parameterized by several authors[121,125,145] with the time of wetness (see Chapter III, Sect. 4.1). Grossi et al. (2011)[146] focused their attention on the phase-transition occurrences and the "mechanical" decay-mechanisms are parameterized by means of the number of crystallization-dissolution cycles (Ncy), an indicator that counts the number of phase transitions (from solid to liquid and reverse) of soluble stone contaminants due to ambient RH variations.

The approach carried out by Casati and co-authors is based on the conductance methods described in Chapter II and on the results presented in Chapter III, Sect. 2. The results provided in Casati et al. (2015)[75] concerns the 2006-2013 period and the estimation of the hydration time and Ncy were limited introducing the experimentally determined DRH and CRH, without any modelling of T-dependence.

Figure 37a shows the different results obtained with time of wetness method calculation and those provided considering the DRH and CRH experimentally determined, i.e. the hydration time (Chapter III, Sect. 4.3). Data are here presented as averaged time and standard deviation among the same months of the 8-years considered. Both methods present a similar trend for what concerns the time in which stone surfaces are wet because both the parameters are strongly related to the climatic conditions of the surrounding air. On the other hand, the time of wetness method suggests lower frequencies in respect of the hydration time method.

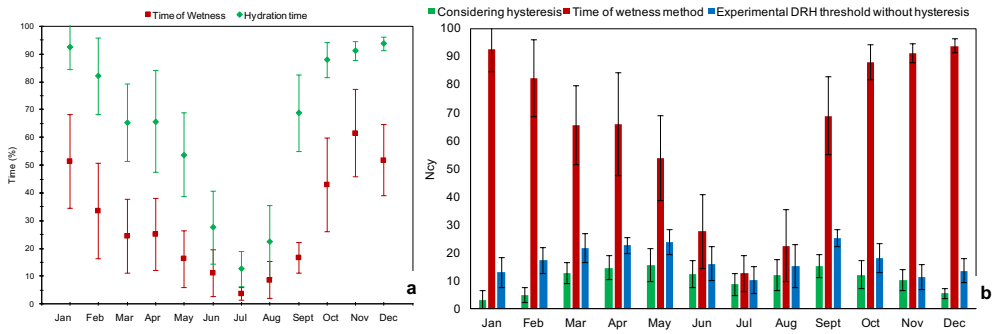

Figure 37 Monthly variability in hydration time (green) and time of wetness (red)(a) and Ncy (b) in Milan for 2006-2013 period.

Similarly, Figure 37b showed that considering 80% RH as threshold, the occurrences from a dry to a wet conditions are more frequents. For example, during January the time of wetness method indicates that Ncy is 93±8. Introducing the measured threshold, i.e. DRH_{end}, the Ncy strongly decreases (13 ±5) even if it still neglects the hysteresis of atmospheric aerosols. In fact, considering also the CRH, the Ncy further decreases since the surrounding air RH, once that aerosols are deliquesced, has to decreased down to CRH in order to complete the crystallization-dissolution cycles. The overall results highlighted that neglecting the hysteresis behavior of atmospheric particles about 64% more cycles/years were calculated.

The analysis of these two improved indicators suggest that WI seasons are characterized by high hydration time (89±11%) but low Ncy (3±3), due to the high RH conditions that are enhanced by low T. On the contrary, low conditions of RH suggest low hydration time (20±13%) but a higher Ncy (11±5) were estimated during SU.

Without considering freezing processes, which can affect the stone weathering but that they were not considered in this work, WI and SU seasons appeared to be less hazardous in respect of FA and SP seasons: Ncy was estimated for 8±6 and 14±5 for FA and SP, respectively while hydration time indicates higher values for FA (83±15%) in respect of SP (61±16%). Therefore, while during FA a "chemical" stress is suggested to be prevalent, the "mechanical" one is more hazardous during SP seasons.

The proposed improvements of the hydration time and number of crystallization-dissolution cycles are based on the considering of the hysteresis behavior of atmospheric aerosols. The water-soluble fraction, once they deliquesce, can enhance chemical reactivity and salts penetration events, therefore surfaces weathering. The estimation of these two parameters indicates that time of wetness method strongly underestimates the wetting occurrences and the "chemical" hazard, whereas it overestimates the "mechanical" stress due to internal re-crystallization of penetrated soluble salts.

CHAPTER V – A PRELIMINARY STUDY OF THE EFFECT OF ATMOSPHERIC AEROSOL CONTAMINATION AND HUMIDITY ON TIN CORROSION

1 – INTRODUCTION

In order to satisfy the demand of smaller electronic devices, the component density on printed circuit boards has strongly grown in the last decades. Due to miniaturization and increase in the component density the heat dissipation efficiency became ever important factor affecting the overall reliability of electronic device. Elevated temperatures first have a significant influence on the reliability of semiconductor devices, secondly high temperatures of *printed circuits assembly* (PCBA) can result in degassing of volatile corrosive compounds (fire retardants) from laminate material [147], [148], or affect robustness of solder joints. Therefore, high dissipation from the PCBA is often controlled by cooling. One of the commonly used cooling methods is forced convection, which causes an increase of the airflow to the PCBA. On the other hand, this increases the devices exposure to moisture and contaminants [149,150] and consequently the risk of metal corrosion. In fact, high humidity conditions promote the formation of thin water-layer on the surface of circuits, which enhances gaseous species (such as O_2, SO_2 and NO_x) solubilization. In addition, the deposition of particulate contaminants facilitates the water-layer development as well, due to the hygroscopicity of many compounds of atmospheric particles. The consequence of this can be electronics failure as stated by Litvak et al.(2000)[151], who reported that about $200 million was annually spent to repair failed electronic circuits of telephone switching offices due to the effects of indoor air pollutants.

In the past years, Sn-Pb solders were mostly used in electronic because of their low cost, low melting and good solderability[152]. On the other hand, with the introduction of *Restriction of Hazardous Substances Directive* (RoHS) 2002/95/EC, lead usage was banned in many field (such as in electronic) because of its eco-toxicological effects. Therefore, many other solder alloys were developed and nowadays commonly used, where tin is the main constituent. According to Takemoto et al. (1997)[153], higher tin contents in Sn-Pb solders lead to lower susceptibility to corrosion, and the lowest one is observed for pure tin in distilled water. For this reason, in the last decade many authors[154–158] investigated the corrosion susceptibility of tin under different contamination conditions.

One of the most important process involves by contaminants and humidity on PCBA is electrochemical migration (ECM). Under an applied voltage, once that a water layer is formed between two electrodes, metal cations are dissolved at the anode.

Anode:

$$Sn_{(s)} \rightleftharpoons Sn^{2+} + 2e^- \quad (R.1)$$

$$Sn^{2+} \rightleftharpoons Sn^{4+} + 2e^- \quad (R.2)$$

$$Sn^{4+} + 4H_2O \rightleftharpoons Sn(OH)_4 + 4H^+ \quad (R.3)$$

$$2H_2O \longrightarrow O_{2(g)} + 4H^+ + 4e^- \quad (R.4)$$

Reactions R.3 and R.4 indicate that at the anode the pH of the electrolytic solution decreased. In high acidic conditions, $Sn(OH)_4$ and $Sn(OH)_2$ tend to remain dissociated as Sn^{4+} and Sn^{2+} and to migrate towards the cathode where alkaline pH is developed:

Cathode:

$$2H_2O + O_{2(g)} + 4e^- \rightleftharpoons 4OH^- \quad (R.5)$$

$$2H_2O + 2e^- \rightarrow H_{2(g\uparrow)} + 2OH^- \quad (R.6)$$

As it was highlighted in Krumbein (1988)[159], the higher the bias the higher is the diffusion of the dissociated species due to the effects of higher electrical field. When Sn^{2+} and Sn^{4+} experience a less acidic or an alkaline environment, they tend to precipitate as hydroxides. Minzari et al. (2011)[160] pointed out the role of the convection within the electrolytic media due to the gaseous species formation. As a consequence, even if tin hydroxides are formed at the alkaline/acid region interface at the beginning, the convection leads to further dissolution of the solids and tin cations are free to migrate towards the cathode again. Moreover, in an high alkaline conditions, tin hydroxides disproportionate (R.7). Although $(Sn(OH)_6)^{2-}$ would be repelled by the cathode, this migration mechanism could be explained because of an equilibrium between $(Sn(OH)_6)^{2-}$ and Sn^{4+}, as reported in Minzari et al. (2011)[160]. Once they reach the cathode, which is not influenced by further changes in pH, tin hydroxides and metallic tin precipitates are formed and act as new cathode:

Cathode:

$$Sn(OH)_4 + 2OH^- \rightleftharpoons (Sn(OH)_6)^{2-} \quad (R.7)$$

$$(Sn(OH)_6)^{2-} + 4e^- \longrightarrow Sn_{(s)} + 6OH^- \quad (R.8)$$

$$(Sn(OH)_6)^{2-} \rightleftharpoons Sn^{4+} + 6OH^- \quad (R.9)$$

$$Sn^{4+} + 4e^- \longrightarrow Sn_{(s)} \quad (R.10)$$

Consequently, the electrode distance is shortened because of dendrites growth from cathode towards anode. This causes a further increase of current density between the electrodes and it can cause the failure of PCBA due to electrical shorts.

The synergic effects of contamination and air humidity on the PCBA was investigated by many authors. Sherlock and Britton (1973)[161] found that nitrates enhance tin dissolution, therefore increase the corrosion rate. Warren et al. (1989)[162] observed ECM at 76% RH on α-alumina substrates contaminated with $CuCl_2$. Frankenthal et al. (1993)[163] identified 75% RH (at 373 K) as the threshold condition above which the formation of $Cu_4(SO_4)(OH)_6$ is observed for copper specimens contaminated with submicron-sized $(NH_4)_2SO_4$ particles. Verdingovas et al. (2014)[59] investigated the effect of NaCl contamination at different RH and temperature (T) on

surface insulation resistance (SIR) comb pattern measuring leakage current (LC) biased at 5 V DC. The authors observed a strong increase in LC above 75% RH at room T. Lately, Verdingovas et al. (2015)[60] pointed out the effects of five weak organic acids – namely adipic, succinic, DL-malic, glutaric and palmitic acids commonly used in no-clean fluxes – on LC finding RH thresholds above which LC started to increasing abruptly. These studies highlighted the role of the deliquescence of the contaminants on corrosion, since it implies the formation of an electrolyte solution and the increase in the electrical conductivity of the moisture film on the PCB surface. As a consequence, decreasing in performance of the electronic components can happen due to higher LC and shorts [164].

Contrary to a situation in which a security threshold can be easily identified since just a pure compound contaminates the circuit, ambient contaminants present a more complex chemical composition (Chapter I and III). Considering the liquid or solid particles suspended within the troposphere (with a diameter between few nanometers up to hundreds of micrometers, i.e. atmospheric particles), their chemical composition varies in time and space because of the different sources and chemical reactivity [14,165,166]. The key role of these contaminants is due to the hygroscopic behavior of many compounds, mostly inorganic ionic ones, forming atmospheric particles, which enhances the formation of a thin water layer on the circuit surfaces. Concerning the fine fraction, i.e. $PM_{2.5}$, the results showed in Chapter III (in agreed with those found by many authors [167,21,97]) stated that WS compounds represent an important mass fraction.

In Chapter III and in D'Angelo et al. (2016)[74], a relation between chemical composition and phase transition relative humidity was highlighted, showing that an electrolytic solution due to deliquescence can form starting in the range 50-70% RH.

These results indicated that electrolytic layers can be developed far from water condensing conditions. Thus, in this chapter a preliminary study on the effects of atmospheric particles are investigated in relation to their role in tin corrosion. The atmospheric contaminants were deposited on eleven tin SIR patterns (surface insulation resistance, see Sect. 2) and stored in a climatic chamber where impedance was measured in order to identify the DRH and CRH of the particles (Sect. 3.1) similarly to the methods used elsewhere [57,58,61]. Moreover, the effects of the RH changing rate and the T exposure on the impedance measures are discussed (Sect. 4.1 and 4.2) and LC at 5 V DC was measured in order to study the synergic effects of contaminants and RH on the corrosion of tin SIR patterns (Sec. 4.3).

2 – METHODS

2.1 SIR patterns contamination

The effects of atmospheric particles contamination were studied on a lead-free hot air solder levelled (HASL) surface insulation (SIR) patterns (Figure 38). Overall surface area of the SIR pattern was 13 mm x 25 mm. The width of conductive lines and the spacing in-between the lines

were 0.3 mm. The nominal square count (ratio of total length of opposing faces and the spacing of segments) of SIR pattern was 1476.

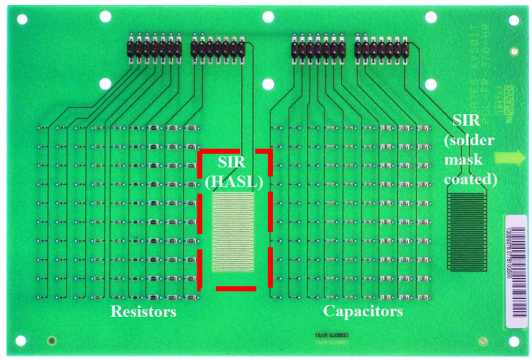

Figure 38 Test PCBA used. In red dashed line is indicated the circuit element contaminated.

A cascade impactor (Sioutas Personal Cascade Impactor, four impact stages, particle size cut-point: 2.5µm, 1.0 µm, 0.5 µm, 0.25 µm and a filtering stage) was modified in order to deposit a round spot with a diameter of 2.0 cm, by means of a mechanism which allowed the complete rotation of the line-shaped nozzle in less then 6 min. The airflow rate was set constant at 10 L min^{-1} by means of a vacuum pump. The SIR patterns were removed from the PCBA and housed at the lowest impaction stage (nominal particles size range: 0.25 – 0.50 µm) to deposit the finest fraction possible, which was shown that represents an important mass fraction within the atmospheric particles size mode [77,168]. In addition, the finest particles are recognized being the most hazardous fraction due to the fact that they can easily bypass filtering systems [149].

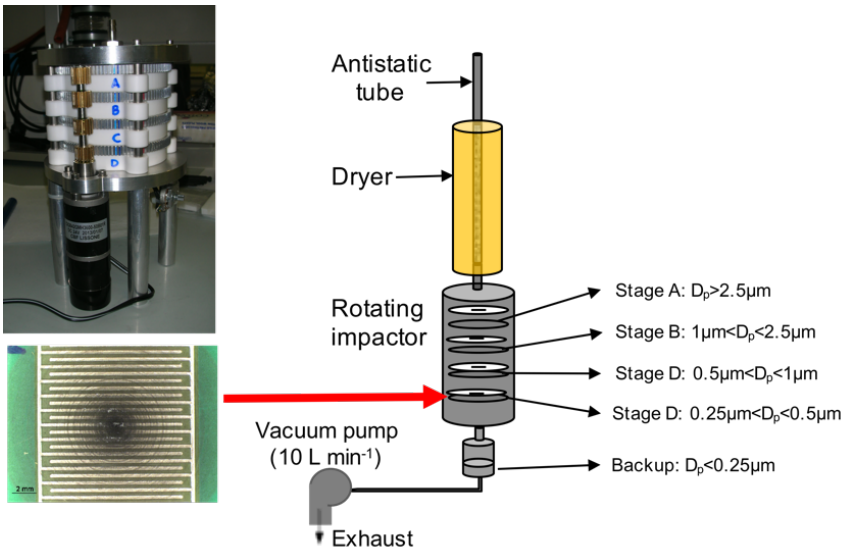

Figure 39 The ROTating impactOR (ROTOR) and the experimental setup for SIR patterns contamination.

In order to avoid the deposition of liquid particles, the airflow was forced passing through an airflow-tube dryer before entering inside the modified *ROTating impactOR* (hereinafter called ROTOR). The sampling campaign was carried out in Milan between 19th March and 26th March.

The effects of atmospheric particles were compared with pure NaCl particles as well. A 25 M solution was prepared and a NaCl spray was generated by means of a Topas ATM 220 atomizer. The spray was inlet within a PTFE (poly-tetra-fluoro-ethylene) smog-chamber and collected on SIR patterns with the same set up used to collect the ambient particles.

2.2 Climatic chamber and exposure conditions

Contaminated SIRs patterns were exposed to increasing and decreasing RH conditions in the ESPEC PL-3KPH climatic chamber. The RH ramp was gradual and continuous in the range of 30-99% RH with a variation rate of 0.49% RH min^{-1}. The fluctuations in temperature – set at 298 K – and RH in the climatic chamber during the testing were below ±0.3°C/±2.5% RH, as specified by the manufacturer. Prior to experiments, the samples were stored inside a desiccator for 48 h at low RH condition (<15% RH). At the beginning of experiments, climatic chamber was programmed to keep for 1 h at 30% RH: in the last 30 min measurement equipment recorded data in order to be sure that the contaminants where completely in equilibrium with the air conditions.

Moreover, three SIR patterns contaminated with atmospheric particles were exposed to three RH ramps with different variation rate (Sect. 4.1), i.e. 0.49% RH min^{-1} (2h 20min for each ramp),

0.10 % RH min^{-1}(12h) and 0.05 % RH min^{-1}(24h). Between each cycle, the chamber was kept at 30% RH for 1 hour allowing to the samples to reach the equilibrium with the surrounding air. Further, three SIR patterns were also exposed to three RH cycles (rate 0.49 RH min^{-1}) setting surrounding air temperature at 281 K, 298 K and 308 K (Sect. 4.2).

2.3 Impedance and leakage current measurements

Formation of thin water-layers on the PCB surface was followed by measuring impedance at 1 kHz frequency with a 25 mV sinus amplitude. The impedance at 1 kHz frequency is dominated by the capacitance between the SIR lines, when RH is low (below deliquescence RH of the dust). However, when RH increases, water layer starts to build up and contamination deliquescence, the measured impedance becomes dominated by the resistance of water layer between the lines rather than capacitance. In this case, a significant reduction in impedance corresponds to the deliquescence of the dust and increase in water layer thickness.

The measurements were performed with a "BioLogic VSP" potentiostat at 1 kHz frequency and with 25 mV sinus amplitude. Measured data are presented as mean values within a RH range of RH-0.5% ≤ RH < RH+0.5%. Although Ferrero et al. (2014) [76] showed the effectiveness of DC voltage in order to identify both DRH and CRH on PTFE filters, it is well known [61] that AC voltage limits corrosion, because of the low voltage applied, and it avoids dendrites formations, because anode and cathode are not fixed and there is not enough time for that due to the high frequency usually used.

ECM is typically studied applying constant voltage and measuring LC through not-linked electrodes [169]. In this circumstance, "BioLogic VSP" potentiostat was used to record the low current passing through a conductive layer. Thus, 5 V DC was applied to SIR patterns and LC was recorded within increasing and decreasing RH ramp (30.0-90.0% RH).

In addition, in order to observe the behavior of atmospheric contaminants in condensing conditions, WS compounds were sonically extracted from PTFE filters (see Sect. 2.4), diluted four times (from 1:2 up to 1:16) and a 2.5 µL micro-droplet was placed on ceramic chip capacitor (housing size 0805, Yageo Phycomp, Taiwan Type 2238 580 15649). Thus, five solutions for three atmospheric particles samples were tested and LC was measured at 5 V DC biased for 15 min at room RH and temperature until complete evaporation of droplet (which needed in average about 10 min). Each test was repeated at least 10 times. The results are discussed in Sect. 4.4.

2.4 Chemical characterization of atmospheric contaminants

Morphology of corrosion products and tin dendrites after the LC measurements was characterized by means of scanning electron microscope (SEM JEOL 5900 instrument) and analyzed for elemental composition with energy dispersive spectroscopy technique (EDS Oxford Link ISIS).

In order to chemically characterize the WS fraction of collected contaminants, atmospheric $PM_{2.5}$ was collected on PTFE filters (Millipore®, Ø=47 mm, PMP ring, 2 µm porosity). Each sample was collected for 24 h in Milan (Italy) between March 19th and 26th 2015 by means of a gravimetric low-volume sampler (FAI-Hydra dual channel, 2.30 m^3 h^{-1}). Filters were stored at low RH conditions (<15% RH) for 48 h and weighed before and after the sampling campaign. Particles mass was determined using a weighting precision balance (Sartorius SE-2F, 0.1 µg precision). WS compounds were then extracted in ultrasonic bath for 20 min (SONICA®, SOLTEC, Italy) in 3 mL of ultrapure water (Milli-Q®, 18.2 MΩ cm^{-1} at 25°C) and the solutions were then recovered with a syringe and filtered (0.45 µm PTFE Syringe Filters, Phenomenex). The extraction efficiency was investigated elsewhere [4]. $PM_{2.5}$ WS compounds were then analyzed with ion chromatography technique by means of Dionex ICS-90 (analytical column: Ion Pac CS12A-5 µm Analytical 3x150 mm, Dionex) for cations (Na^+, K^+, Ca^{2+}, Mg^{2+} NH_4^+) and ICS-2000 (Ion Pac AS14A-5 µm Guard and Analytical 3x150 columns, Dionex) for anions (F^-, acetate, formiate, Cl^-, succinate, NO_3^-, SO_4^{2-}, oxalate and PO_4^{3-}).

WS compounds extraction was also carried out in order to evaluate the corrosion behavior of this fraction on pure tin. Otherwise to the volume extraction used for chemical characterization, the sampled filters were extracted in 10 mL of ultrapure water in order to carry out at least three repetitions of the same measurements.

2.5 Micro-Electrochemical measurements

The corrosiveness of the WS particles was investigated by performing potentiodynamic polarization measurements using electrolyte solution from collected contaminants. The overall inorganic ionic concentration of the tested solution accounted for 101.3 ppm. Prior to start the electrochemical measurement, leakage current measurements of 100 µL droplets were carried out. The results of these tests allowed identifying the concentration of a NaCl solution as reference during the micro-electrochemical analyses, i.e. 15.6 ppm. The potentiodynamic polarization measurements were performed on a sample of pure tin, which is most commonly used element for the surface finish on the PCBs. The sample was cleaned with 2-propanol and ultra-pure water prior to testing. However, no polishing of the sample was done, in order to maintain oxide layer naturally existing on tin finish surfaces (solder alloys) on the PCBA.

The potentiodynamic polarization measurements were performed using micro-electrochemical cell, which allows measurements using low volume of electrolyte. The detailed description of the cell can be found elsewhere[170]. Micro-electrochemical cell (Figure 40) is designed for the measurements with high lateral resolution, which is defined by the diameter of pipette tip, which makes the contact with a local region of the working electrode (1 mm in current case).

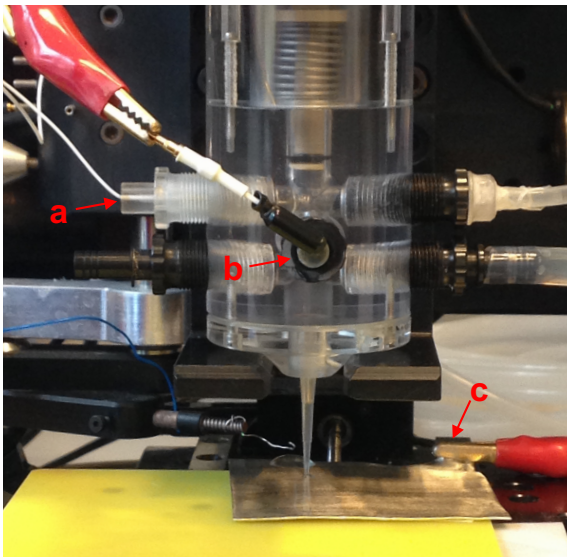

Figure 40 Micro-electrochemical cell: (a) counter electrode, (b) reference electrode, (c) working electrode (crocodile linked directly to tin).

The potentiodynamic polarization measurements (cathodic and anodic) were performed relative to Ag/AgCl micro electrode at a scan rate of 1 mV/s. Prior to potentiodynamic polarization, the open circuit potential (OCP) measurements were performed. The potential stabilization was observed within first 5 min of OCP measurement.

3 – RESULTS

The degree of contamination of the SIR patterns by means of the prototype ROTOR was estimated by means of data provided by an optical particles counter (OPC Grimm, Model 1.107, "Environcheck", 31 size classes from 0.25 to 32 µm, time resolution: 5 min). The OPC allows to quantify the number concentration of particles classifying them into 31 classes basing on their dry optical diameter. Assuming a spherical shape, the particles volume concentration was calculated and log-normally distributed data were fitted in order to estimate the volume of particles with a diameter down to 30 nm. Once that a complete size distribution was obtained in the range 30 nm – 32 µm, the cumulated volume of particles with sizes 0.03 – 2.5 µm was used in order to estimate the $PM_{2.5}$ density as the ratio between particle mass collected on PTFE filters ($PM_{2.5}$) and the calculated volume. The results indicate that $PM_{2.5}$ fraction sampled in Milan during the campaign period was 2.1±0.1 g cm^{-3} (average ± standard deviation).

Literature data [171–174] had shown that particle density can vary from 0.6 g cm^{-3} for freshly emitted diesel exhaust particles to 3.2 g cm^{-3} for coal combustion particles. McMurry et al. (2002)

[175] measured 0.1-0.3 µm sized particles density finding a mean range between 1.54 – 1.77 g cm^{-3} for urban spherical hygroscopic particles in dry conditions but density within the range 1.7 – 2.2 g cm^{-3} were also observed. In this context, our estimations seem in agreement with the previous findings.

In order to estimate the mass of particles deposited on SIR patterns, density was assumed constant within the whole size distribution range of interest. Hence, the average mass of atmospheric particles was estimated of 0.345±0.093 mg, which corresponds to 95.6±28.6 µg cm^{-2} on SIR patterns.

Impedance measurements carried out on SIR patterns contaminated with NaCl and atmospheric particles are shown in Sect. 3.1.

3.1 Impedance behavior of contaminated SIRs

The effects of deposited NaCl particles were firstly investigated at increasing and decreasing RH exposure conditions (Sect. 2.1, rate 0.49% RH min^{-1}). Whereas a negligible reduction in impedance was measured up to 62% RH, water uptake was detected from 63.0% RH when the impedance started to decrease (Figure 41). A sharp drop in impedance was recorded within 74.0-77.0% RH: this drop happened in correspondence of the DRH of NaCl. Above the DRH, water uptake still occurred and impedance decreased until 99% RH.

Concerning the electrical behavior of SIR pattern with decreasing RH conditions, Figure 41 clearly shows that electrolytic solution formed on the SIR surface tends to decrease the conductive properties and a strong increase in impedance occurred between 59.0 – 52.0% RH range, interpreted as CRH.

Similarly, the SIRs contaminated with atmospheric particles (Figure 42) highlighted a hysteresis loop. In Figure 42a, an early water uptake led to an impedance decrease below 54% RH. Further increase in RH caused a drop in impedance within the range 55.0-63.0% RH. Above this range, impedance continued to decrease with the RH increasing, reaching an impedance values below 20 kΩ at 90.0% RH. During the decreasing RH period, firstly, a slow increase in impedance was observed, then a faster one was recorded suggesting a re-crystallization of water-soluble compounds within the range 50.0-44.0% RH and then a complete water evaporation.

Figure 42b shows a different behavior in respect of the previous one, especially during the decreasing RH ramp. For this sample, the deliquescence process was observed starting at 56.0% RH until 65.0% RH, while the crystallization was identified within the range 56.0-52.0% RH^{-1}. Nevertheless, the ability in conducting electrical signal is far from being similar to the beginning of the increasing RH ramp.

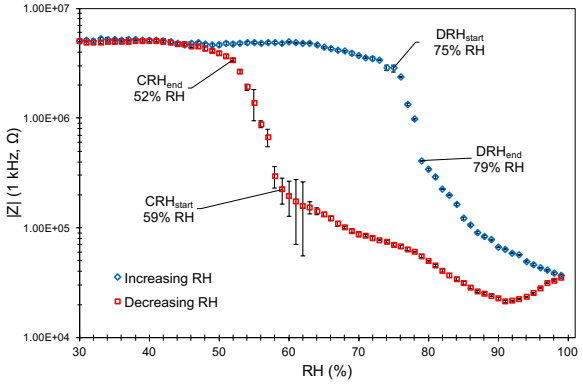

Figure 41 Impedance response for NaCl contaminated SIR pattern.

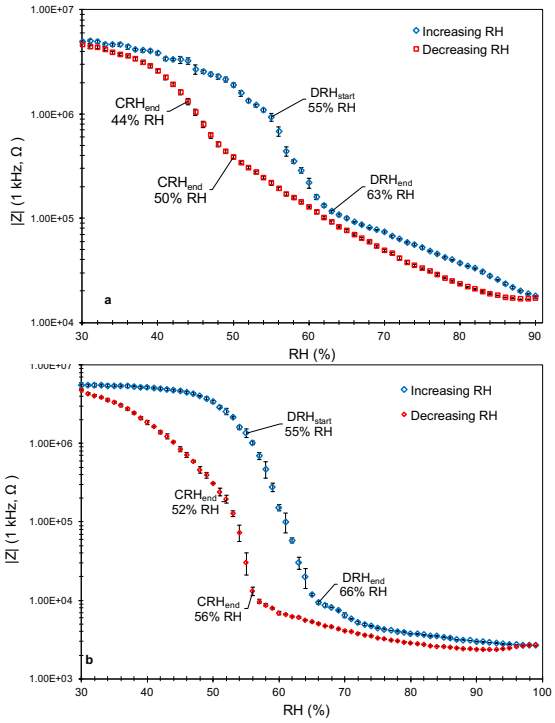

Figure 42 Impedance responses for two SIR patterns contaminated with atmospheric particles.

3.3 Potentiodynamic polarization of tin in atmospheric electrolytes

Figure 43 shows potentiodynamic polarization curves obtained for the WS compounds of atmospheric particles and a reference electrolyte containing NaCl (15.6 ppm). When comparing

anodic polarization, it can be clearly seen passivation region and breakdown of the passive oxide layer on a surface of tin for the WS compounds containing electrolyte. For the NaCl electrolyte, in contrast, no clear breakdown potential was seen. The fluctuations in current during anodic polarization, and passivation of the surface were observed for both electrolytes, although for atmospheric contaminants it was more pronounced. The corrosion potential was higher (more noble) in electrolyte solution containing atmospheric compounds, (-126 ± 11) mV vs (-198 ± 3) mV in NaCl solution. The corrosion current density was also slightly higher in electrolyte containing atmospheric WS compounds $(1.21 \pm 0.31) \cdot 10^{-3}$ mA cm^{-2} compared to NaCl solution $(8.71 \pm 3.87) \cdot 10^{-4}$ mA cm^{-2}. A pronounced increase in current density was observed for atmospheric compounds containing electrolyte above a breakdown potential, and the resulting current density was higher compared to NaCl.

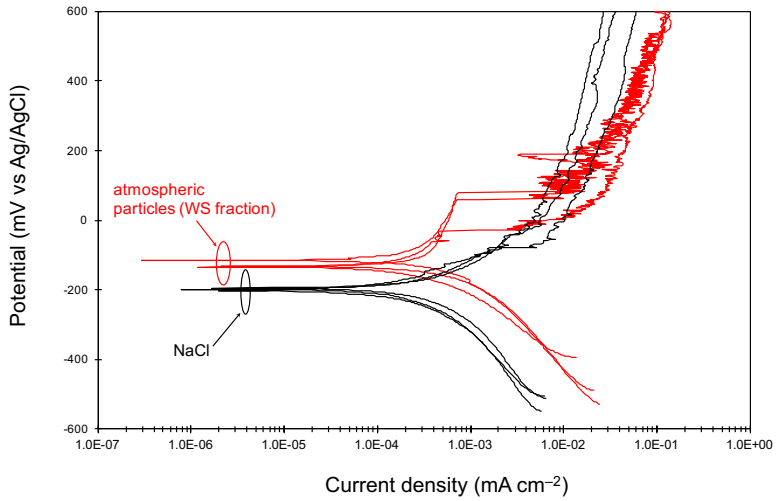

Figure 43 Potentiodynamic polarization of tin in electrolytes of NaCl and WS compounds of atmospheric particles.

4 – DISCUSSION

The results showed in sect. 3.1 highlighted the effect of RH exposure conditions on the impedance due to the hygroscopicity of NaCl salt and atmospheric particles deposited on the SIR patterns. The electrical methods were used by many authors in order to observe the phase-transitions of inorganic salts [57–59], weak organic acid [60], coarse dust [61] or atmospheric particles [75] deposited on different surfaces. The authors highlighted the effectiveness of this method to characterize the DRH of the contaminants. The resistance drop becomes dramatic when RH reaches the DRH since the contaminants form an electrolytic solution on the substrate surface.

For NaCl salt deliquescence occurs at 75% RH[40], perfectly in agreement with the observation presented in Sect. 3. In decreasing RH conditions, the opposite behavior was observed and impedance increased. According to D'Angelo et al. (2016)[74], Schindelholz et al. (2014)[58] and Ferrero et al. (2015)[76], when an abrupt increase happened, crystallization of NaCl salt occurred. In this regards, two observations were allowed by means of data showed in Figure 42. *In primis*, evidence of the hysteresis behavior was seen due to the fact that DRH and CRH occurred at two different RH conditions. This is because before crystallization, all the water needs to evaporate from the solution even if the solid-liquid energies were equal at higher RH, i.e. at the DRH, and particles need crystallization nuclei in order to crystallize. Moreover, the observed CRH was higher then the CRH commonly found in literature (45% RH[176]). This could suggest the presence of crystallization nuclei, which increased the CRH of NaCl. Thus, our hypothesis is that AC and high NaCl contamination level caused a weak tin corrosion, which made available seeds for premature heterogeneous nucleation[107,177]. The effects of chloride contaminations on corrosion under alternating field was investigated by many authors[178,179]. For example, Kim et al. (2006)[180] observed that AC fields accelerate the corrosion of mild steel both in NaCl solution and natural seawater environments.

The analyses carried out on 9 SIR patterns contaminated with atmospheric particles indicated that DRH occurred within 51.7±2.9% RH and 59.0±4.5% RH range at 298 K. Evaporation, which occurs drying the air inside the climatic chamber, caused a reduction in the thickness of the water layer and increases the electrolytes concentration of the solution. This explains the increase in impedance until an abrupt change was observed ramping from 49.0±5.3% RH to 41.5±4.8% RH. This range was identified as the crystallization one and an hysteresis was clearly observed. Figure 42b showed that when RH was decreased to 30%, impedance was still higher in respect to the levels measured at the beginning of the cycle. This behavior suggested that water was still absorbed to atmospheric contaminants, likely due to kinetic limitations on water mass transfer at low RH[90,93].

The obtained results of DRH and CRH for atmospheric particles are in agreement which those described in Chapter III: samples with high NO_3^- ions showed DRH range between 51.6±0.7% and 58.5±0.7% RH while CRH was observed in average within 48.1±0.5 – 44.3±0.6 % RH range. These findings perfectly agreed with date presented in this chapter. The results from ion chromatography (Sect. 2.4) carried out on the extracted WS compounds from $PM_{2.5}$, suggested that the samples were chemically similar to the WI samples with a high content in nitrate (25.7±4.6% w/w) and a lower content in sulfate ions (12.1±0.6% w/w) and an average ratio NO_3^-/SO_4^{2-} of 2.1±0.5. Inorganic ionic fraction accounted for 50.1±4.8% w/w of the total mass of particles collected on filters. In addition to nitrates and sulfates, ammonium ions (10.5±1.0% w/w) represented the manly specie found. Other cations (Na^+, K^+ and Mg^{2+}) and inorganic anions

(F^-, Cl^-, PO_4^{2-}) accounted for less then 1% each. The organic acids were found representing about 1.1±0.4% of the mass.

Other parameters can affect the hygroscopic behavior of particles, thus their effects on circuits. Sect. 4.1 and 4.2 described the changes in DRH and CRH due to different exposure conditions. The samples used for these experiments were collected between April 20th and 24th, 2015 and particles presented different chemical composition in respect to the ones showed in Sect. 3. In this regards, ion chromatography highlighted that WS fraction was mainly constituted by sulfates (12.4±7.0% w/w) while an important lower content in nitrates (2.8±0.5% w/w), with average ratio NO_3^-/SO_4^{2-} of 0.3±0.2. For this reason, DRH and CRH of these samples were not considered in the previous dissertation. Comparing with the previous dataset (and by means of the same RH variation rate and at 298 K), DRH and CRH occurred at higher RH conditions, i.e. 78–81% RH and 64–58% RH, respectively.

4.1 Kinetic effects on hydration of atmospheric particle contaminants

Figure 44a shows the impedance profile of a SIR pattern contaminated with NaCl during RH cycles at different variation rates (Sect. 2.2). Deliquescence was observed for three RH cycles at 75.0% RH until 79.0% RH was reached. Even if impedance responses showed similar behaviors during the increasing RH ramp, comparing the slowest (rate 0.05% RH min^{-1}) with the others a higher water uptake was suggested since lower impedance values were reached. The same hypothesis seems supported from the decreasing RH ramps: at RH>70%, the impedance response is lower in respect of the faster response. Then, it assumed the same order of magnitude of the slower ones.

A SIR pattern contaminated with atmospheric particles is shown in Figure 44b. The profiles highlighted how the DRH and CRH tend to decrease with variation RH rate decreasing. The fastest RH cycle (rate 0.49% RH min^{-1}) showed DRH within 79.0 – 84.0% RH range while CRH within 61.0 – 58.0% RH. Slowing down the variation rate, both DRH and CRH decreased.

Data analysis suggests the importance in defining a RH variation rate in order to simulate the most similar conditions of the circuits operating environment. Thus, since lots of electrical equipment are nowadays exposed to outdoor conditions, a thermo-hygrometric sensor (DMA 572.1, LSI-Lastem S.r.l.) have been recorded RH and T of the air in Milan for seven months from March 2015 to September 2015 with a time resolution of 5 min. Relative humidity variation rate was then calculated and an average rate of ~0.14% RH min^{-1} was obtained. This means that in order to simulate a real RH cycle, a single RH ramp should last about 8 h.

On the other hand, many electronic systems are protected within box enclosures, which can both make difficult the heat dissipation and slow down the variation rates of humidity in respect to the external conditions. For these reasons, a better evaluation of how humidity changes inside the electrical panel boxes is needed. In this regards, nighttime low temperatures can promote condensation within the electrical panel boxes and this effect is also facilitated by switching off

the electrical circuits, which do not provide a source of heat in order to keep the humidity below the condensation conditions. As a consequence, when circuits are switched on and current flows, humidity can affect electrical properties of the electrolytic layer depending on the air temperature (Sect. 4.2). In other cases, moisture condensation can enhance corrosion, ECM and electric short failures (Sect. 4.5).

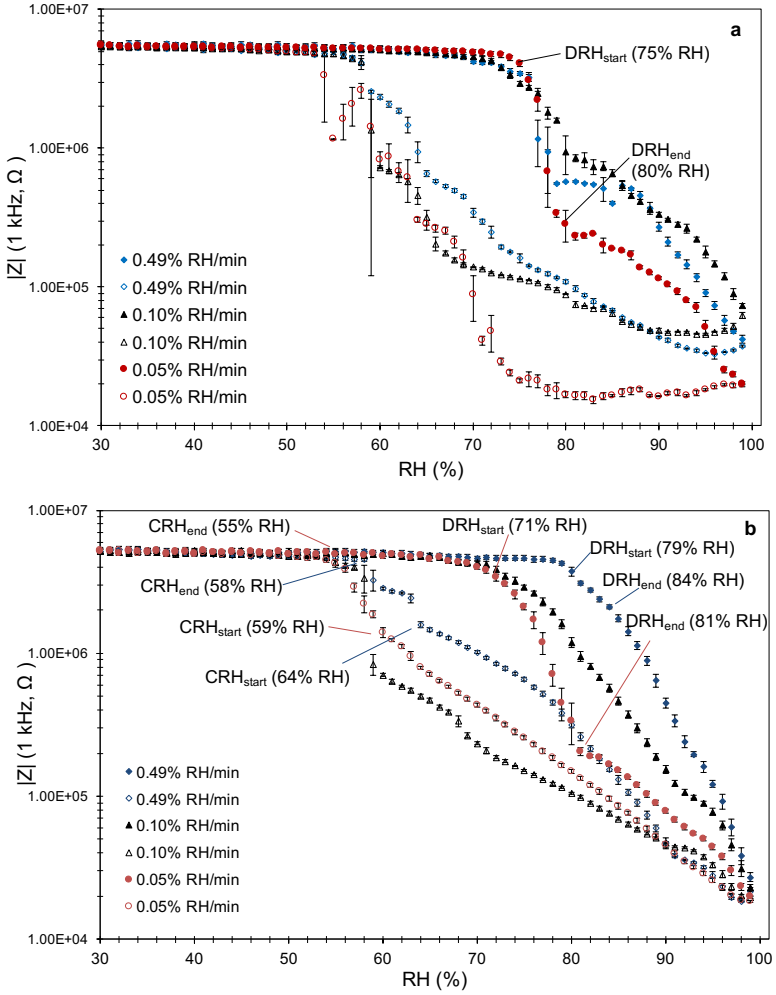

Figure 44 Kinetic effects on impedance on SIR patterns contaminated by NaCl (a) and atmospheric particles (b).

4.2 The effect of the surrounding air temperature

In order to observe the effects of T on atmospheric particles deposited on SIR patterns, three RH cycles were carried out at different T (Sect. 2.2). Figure 45 shows the impedance responses to three different T during increase (Figure 45a) and decrease (Figure 45b) RH ramps. The results clearly highlighted that both DRH and CRH decrease with the increasing in air temperature. As a preliminary analysis, data suggested that an averaged decrease in DRH of 0.4±0.1% RH K^{-1} and in CRH of 0.5±0.2% RH K^{-1}.

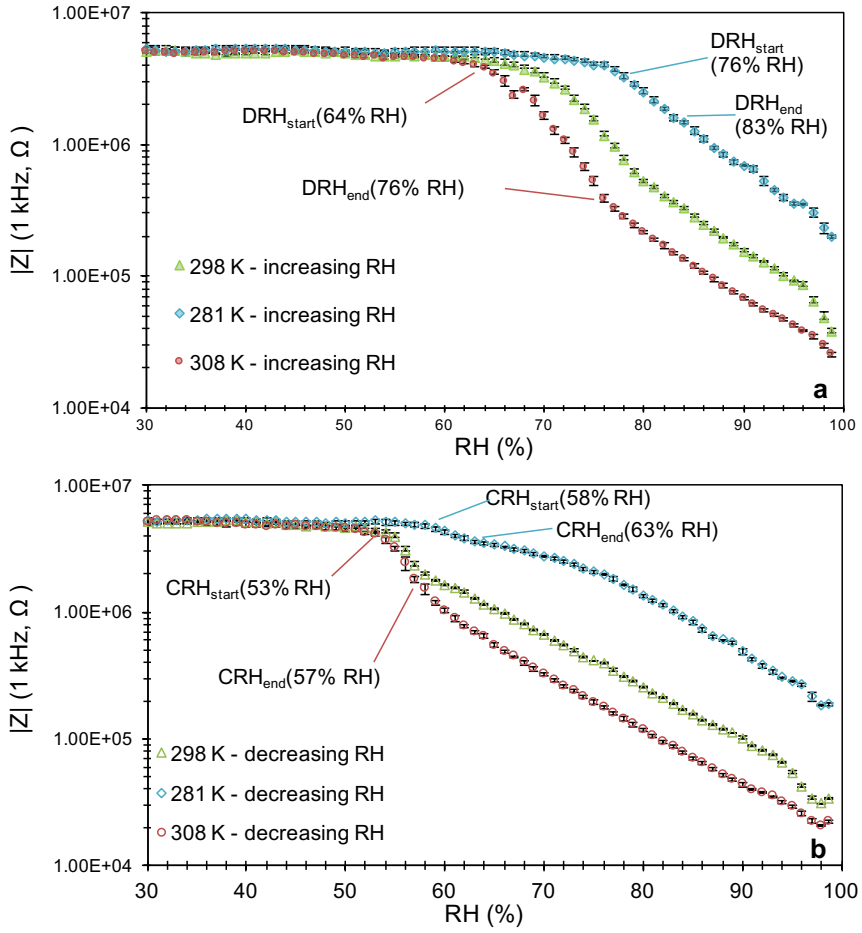

Figure 45 Impedance responses during increasing (a) and decreasing (b) RH ramp obtained at different temperatures.

Beside a lower DRH, a reducing in impedance values with the increase in temperature was recorded in agreement with findings in Song et al. (2013) [61]. Song and co-authors linked this behavior with the lower DRH conditions, which permit more moisture absorption and an increase in water layers at fixed RH, and with higher solubility of WS compounds forming atmospheric particles and corrosion products.

Many authors [39,46,56] highlighted the temperature-dependence of DRH for pure inorganic salts or mixtures. Although many evidences are available regarding the DRH-temperature dependence, few works were carried out to understand the effect of the temperature on the crystallization process. Zeng and co-authors (2014)[32] used an ATR-FTIR flow system in order to study the temperature dependence of methanesulfonate sodium salt (CH_3SO_3Na), one among the most abundant atmospheric methanesulfonate salt due to dimethyl-sulfide reactivity with OH radical [181]. They found a negative trend of DRH and CRH with temperature. The same trend was obtained for ammonium sulfate but not for sodium chloride, which showed a negative trend for DRH and a weak positive trend for CRH.

4.3 The effect of atmospheric contaminants and RH on leakage current on SIR patterns

Leakage current was measured applying 5 DC voltage during a RH cycle from 30.0% to 90.0% RH and reverse with a single ramp duration of 2 h 20 min. In Figure 46 the impedance response (Figure 46a) and the leakage current measurements (Figure 46b) of the same sample are shown. The SIR pattern was contaminated with an estimated particles mass surficial density of 270.6 μg cm^{-2}. The impedance response revealed that atmospheric contaminants enhanced water adsorption even at low RH conditions that caused an increase in LC as well (Figure 46b). At the beginning of the experiment, measured LC was lower than 10^{-3} mA and it increased up to 10^{-2} mA at 57.6% RH. Even though the starting RH of the deliquescence process is not clear, the impedance response points out that the end of this processes occurred at 64.0% RH. Below this threshold, the increase in LC was already observed but, starting from 64.0% RH, the LC showed a further increasing trend. This suggested that water-soluble compounds dissolved and the electrolytic layer formed on the SIR surface allowed the conduction of charges and the electrolytic cell was active (corrosion of SIR pattern). At 71.8% RH a sharp increase in LC – from $5.3 \cdot 10^{-2}$ mA to $1.7 \cdot 10^{-1}$ mA at 72.1% RH – was detected indicating that ECM occurred and resistance between the two conductive tin lines was reduced. This fact was confirmed by the SEM-EDS analysis shown in Table 7. Although no dendrite-like structures were observed, EDS revealed the presence of oxides/hydroxides and tin deposits between the conductive lines, therefore a shorten of their distance that caused the increase in leakage current.

The maximum measured LC was $3.3 \cdot 10^{-2}$ mA reached at 73.0% RH during the increasing RH ramp. Further increase in RH was not followed by an increase in LC, which irregularly decreased instead and then exponentially diminished when RH was reduced inside the climatic chamber.

In order to compare the effect of atmospheric particle contamination with a not contaminated SIR pattern behavior, a cleaned one was exposed to a longer RH cycle, i.e. 24 h per RH ramp. As Figure 46c shows, LC for cleaned SIR pattern was affected by changing in RH exposure conditions as well but with an exponential growth (diminish) during the increasing (decreasing) RH ramp. Beyond the sharp increases in LC showed by the contaminated samples, the drop in current before the end of the increasing RH ramp suggested a different behavior in respect of the clean SIR pattern, which showed an almost symmetric LC profile referring of the top of the RH ramp. This difference could be ascribed to tin passivation but no information about the corrosion products phases was obtained.

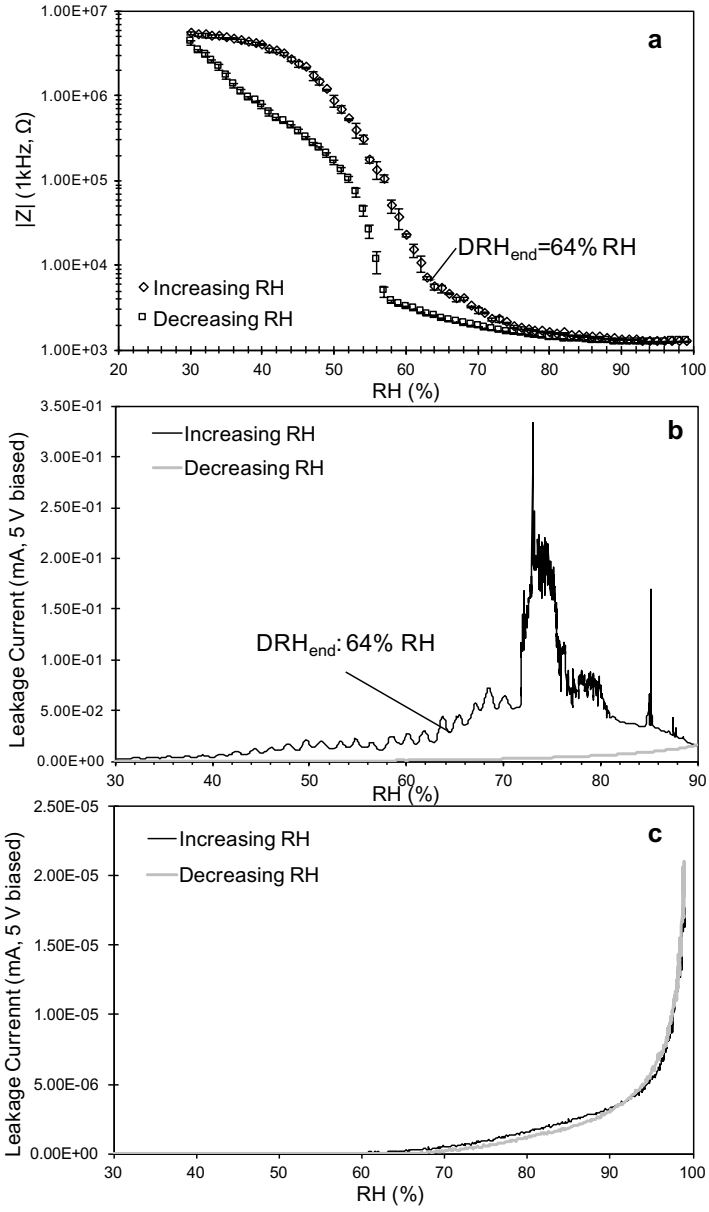

Figure 46 Impedance (a) and LC measurements (b) of the same SIR pattern contaminated with atmospheric particles. A clean SIR pattern was also tested as reference (c).

EDS analyses (Table 7) highlighted the presence of sulfur and oxygen forming the corrosion products. Moreover, ion chromatography carried out by the water-soluble compounds extracted from the PTFE filter – sampled simultaneously with the SIR pattern – showed many other chemical species both organic and inorganic compounds which can affected the corrosion process. Inorganic ionic fraction represents the 50.1% (mass percentage) of the collected particles mass and 1.1% is represented by mono- and di-carboxylic acids. The unresolved fraction (48.8%) was mainly represented by elemental carbon, other not-analyzed water-soluble organic and hydrophobic organic compounds. In this regards, many authors investigated the chemical composition of organic matter within atmospheric particle fine fraction[18,182,183] in urban sites. Sannigrahi and co-authors (2006) [183] found that the main representative functional groups in aliphatic fraction (about 95% of water-soluble organic compounds) were alkyl and oxygenated alkyls (about 80%), carboxylic acids (about 10%) and aromatic functional groups (about 4%) were also found. Such a chemical composition makes difficult the understanding of the processes involved in corrosion. Therefore, micro-electrochemical analyses were carried out on a simplified system consisting of WS fraction only and pure tin (see Section 4.4).

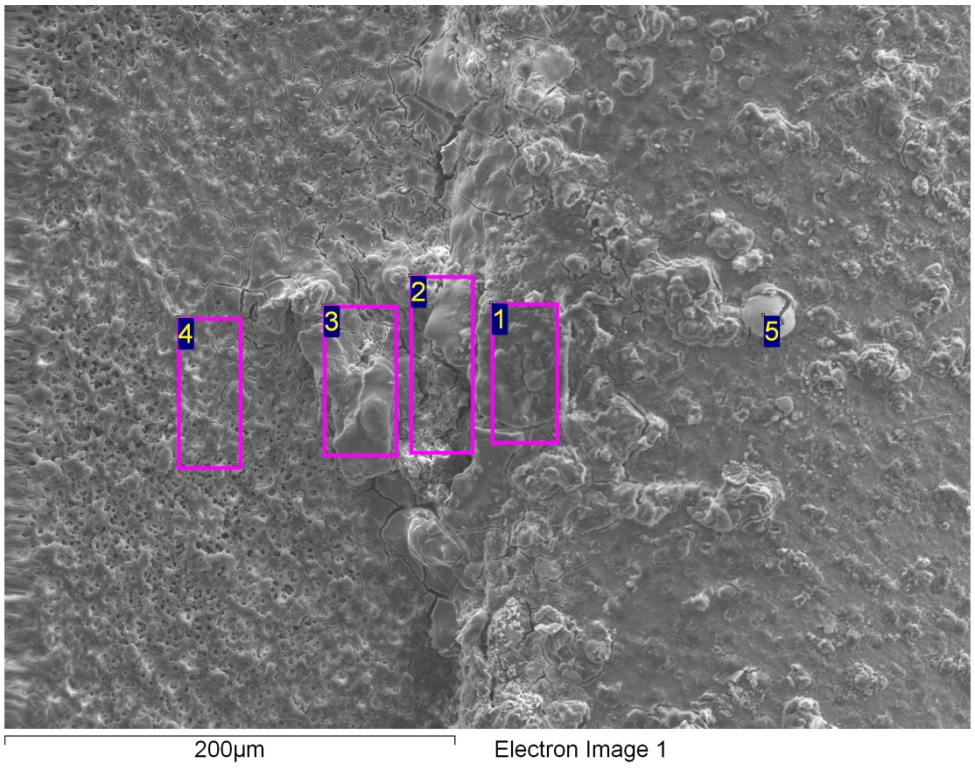

Figure 47 SEM image of the corrosion promoted by atmospheric particles and 5 V DC biased.

Table 7 EDS results of corrosion products referring to Figure 47. All data are given in mass percentage.

Spectrum	O	Br	Si	S	Cu	Sn
1	49	<0.1	-	4	1	46
2	42	<0.1	-	5	4.6	47
3	40	-	-	5	1	54
4	44	3	0.6	4	-	48
5	33	-	-	2	-	64

4.4 Corrosion in condensing conditions

Moisture condensing conditions were simulated by placing a 2.5 µL droplet – containing WS compounds of atmospheric particles – on the ceramic chip capacitors (as described in Sect. 2.3).

Camera was used in order to record bridging formations. Indeed, microscopy technique at the end of the experiment allowed observing dendrite structures on one sample only (Figure 48). In

this regards, EDS analysis highlighted a major contribution in tin (about 60% w/w) and oxygen (<30% w/w). Dendrites breakdown were common likely due to the high current transported through them and heat generated by evaporation of water layer[184]. Both black and white corrosion products were observed on the ceramic chip capacitor surface. The same findings were described in Verdingovas et al. (2013)[185] due to the presence of tin hydroxides. EDS analysis also revealed the presence of other inorganic ions, such as Na and Cl. On the other hand, further investigations are needed in order to identify the crystalline phases presented in the corrosion products. Ion chromatography technique was used to chemically characterize the WS composition of the solutions and the results are summarized in Table 8.

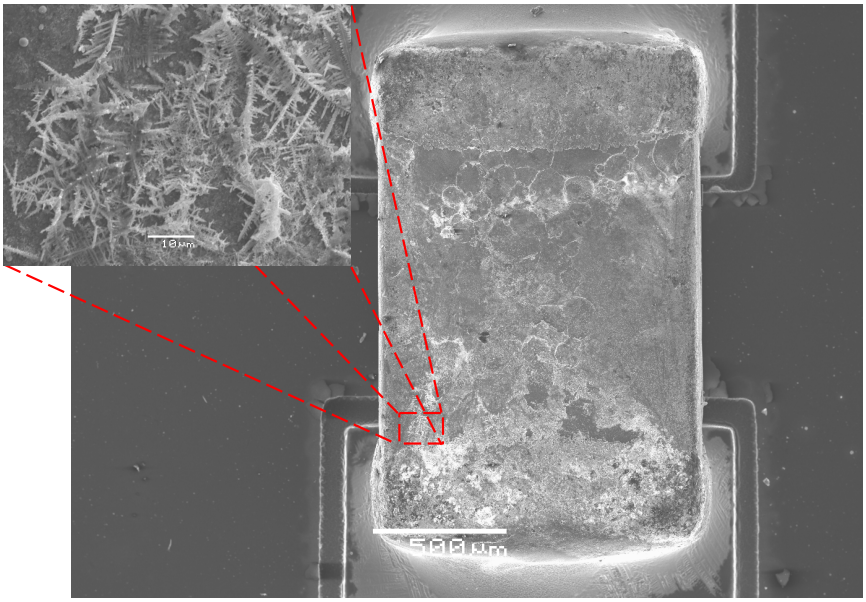

Figure 48 SEM image of dendrite formed on chip capacitor contaminated with atmospheric WS compounds.

The effects of voltage applied on these single components in condensing conditions were investigated in Verdingovas et al. (2013) [185] for NaCl solutions and flux residues solutions at different concentrations. The authors reported ECM probability is as a function of the solution concentration, reporting for NaCl the maximum ECM probability reached for 1.56 µg cm^{-2} contamination degree and 92 µg cm^{-2} for flux residue. It was also reported that at highest level of contaminations no dendrites or tin hydroxides were observed likely due to a reduction in pH, which makes unfavorable their precipitations. The importance of pH in ECM was deeply investigated in Minzari et al. (2011) [160], highlighting the role of convection within the droplet in

dissolving hydroxides precipitates and metallic tin precipitation at the cathode, allowing the dendrites formations and shorts events occurrence.

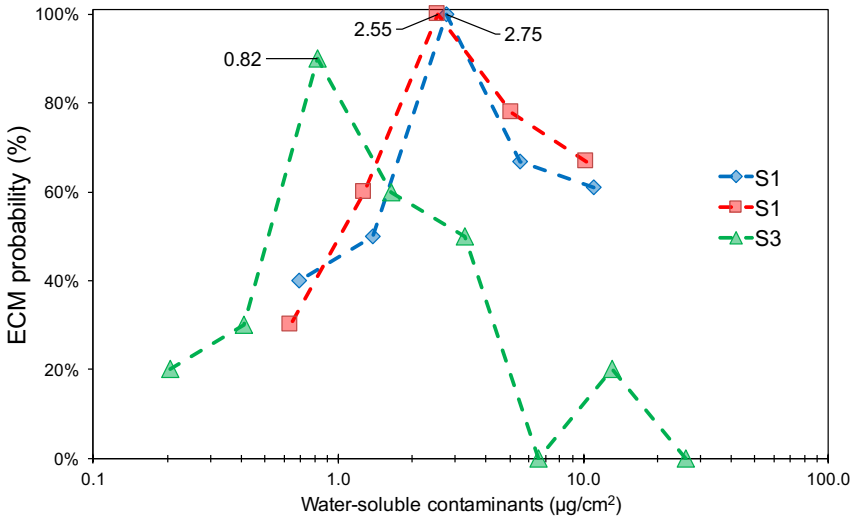

Figure 49 ECM probability in simulated condensing conditions. Three different particles electrolytes contain solutions were applied.

Table 8 Composition of the solutions used for single component test.

Solution	SO_4^{2-}	NO_3^-	Cl^-	Other anions	Organic acids	NH_4^+	Other cations
S1	22.5%	52.3%	0.2%	0.2%	2.0%	19.6%	3.4%
S2	21.9%	51.6%	0.2%	0.2%	2.6%	21.9%	3.4%
S3	28.1%	44.0%	0.4%	0.3%	2.6%	20.6%	4.0%

As it was observed in Verdingovas et al. (2013) [185] and Minzari et al. (2011) [160], ECM presents a bell-shape probability in function of solution concentration. Solutions S1 and S2 are very similar in ionic chemical composition, which correspond to 52.8% and 54.5% of the total mass, respectively. As result, ECM probability reached the maximum for 2.75 µg cm^{-2} and 2.55 µg cm^{-2} of ionic contaminations respectively. Increasing and decreasing in surface contamination the ECM probability decreased (Figure 49). The same shape of probability distribution was showed by the solution S3. Differently, S3 presented a maximum in ECM probability at lower ionic contamination degree (0.82 µg cm^{-2}) and the increase in contamination drops the probability faster in respect of the other two solutions. This was an unexpected results since no relevant changes was detected by means ion chromatography. Verdingovas et al. (2013) [185] found a maximum ECM probability at higher contamination degree (1.56 µg cm^{-2}) for NaCl solution and more then one order of magnitude for flux residue (92 µg cm^{-2}). They authors also reported that

at highest level of contaminations no dendrites or tin hydroxides were observed likely due to a reduction in pH, which makes unfavorable their precipitations. The importance of pH in ECM was deeply investigated in Minzari et al. (2011) [160] highlighting the role of convection within the droplet in dissolving hydroxides precipitates and metallic tin precipitation at the cathode, allowing the dendrites formations and shorts events occurrence.

4.5 Polarization curve and corrosion rate

Potentiodynamic polarization of tin in the WS atmospheric particles containing electrolytes indicated an influence of particles composition on the anodic dissolution and passivation of electrode. In comparison with NaCl electrolyte, the atmospheric electrolytes caused higher passivation (initially lower current density); however, the breakdown of oxide layer in these electrolyte was also more pronounced (potential when significant increase in current density is measured). Above the breakdown potential, a significant increase in anodic current by an order of magnitude was observed, and the resulting overall current density in anodic polarization was higher compared to NaCl. Pronounced fluctuations observed in the anodic polarization above breakdown potential indicated influence of compounds in the atmospheric contaminants on the re-passivation and anodic dissolution of tin. The latter observations also may play a role in electrochemical migration and influence probability for formation of tin dendrites. The electrochemical polarization and passivation of tin in electrolytes containing chlorides and other halides were studied elsewhere [156,160] and they suggested the importance of atmospheric particles composition on the corrosion behavior and passivation. As the dissolution of tin is a rate determining step in formation of tin dendrites, the formation of passive films influence dissolution of tin, thus can affect probability and rate of dendrite formation. The corrosion behavior of Sn-based solder alloys in NaCl and acid electrolytes was also reported[186,187].

Overall comparison of corrosion potential and corrosion current density in current study, indicates similar corrosion rates, although different influence on passivation and pitting of tin. On the other hand, a difference of approximately 75 mV was observed in the corrosion potential, with particles electrolyte resulting in more noble potential.

5 – CONCLUSIONS

This preliminary study was designed to investigate the corrosion effects induced by atmospheric particles on PCBA.

Atmospheric particles were deposited on SIR patterns with a prototype device, called ROTOR. In this work, the contamination degrees were estimated in term of mass deposited from optical measurements by means of an optical particles counter. Even if further improvements are needed, this device provides many advantages in order to establish the corrosive role of atmospheric contaminants. First, the ROTOR allows to force the deposition of real particles on

not-filtering substrates by means of an inertial impaction method. This leads to an accelerated contamination of surfaces avoiding long exposures campaigns usually carried out for atmospheric corrosion tests. Moreover, the ROTOR is able to select the size range of particles that are deposited on the impaction stage. In this work, the SIR patterns were contaminated with submicrometric particles, nominally within the aerodynamic diameter range of 0.25 – 0.50 μm. Therefore, this device has the potential to discern the particle fraction that has the most hazardous role in materials corrosion.

The climatic conditions which enable the corrosion of tin were identified monitoring the impedance at different RH conditions and constant temperature. This allows to observe the formation of a thin water layer, which is enhanced by the hygroscopic behavior of the atmospheric contaminants. In particular, a sharp drop in impedance magnitude indicated the deliquescence of water-soluble compounds, whereas the corresponding increase suggested the re-crystallization of them while RH conditions were gradually decreased.

At 298 K, the averaged results of DRH and CRH were in line with the values found for nitrates-rich samples: this prevalence in nitrate ions in respect of sulfates was confirmed by ion chromatography analyses carried out on $PM_{2.5}$ samples collected simultaneously on PTFE filters.

Further tests highlighted that both air temperature and the rate used for RH variation affect the development of the water layer. The increase in air temperature decreased both phase transitions RH and the impedance values comparing those reached at the same RH condition but different temperature. Similar behaviors were observed when the RH ramp was slowed down. These results pointed out the importance in defining the exposure conditions that can be representative of the PCBA operating environment.

The tin corrosion tests were performed at 5 V DC. The SIR patterns showed that high leakage current levels were reached at complete water-soluble compounds dissociation, i.e. after the end of the deliquescence process, suggesting a potential failure. These conditions were not permanent: leakage current showed a sharp decreased even if the RH was still increasing. Such findings suggested a possible breakdown of dendrite-like structures and similar bridges were observed no more even continuing the RH ramp. This did not permit to observe further high leakage current events, especially when the electrolytic solution formed on the SIR pattern was supersaturated. Since these conditions are very interesting for many applications (such as it is pointed out in Chapter VI), further investigations are needed.

Corrosion tests were also performed on ceramic chip capacitor placing 2.5 μL droplet in order to simulate water condensing conditions. The electrochemical migration (ECM) probability was found to depend on the ionic concentration, showing a bell-shape relation. Comparing with previous results found by Verdingovas et al. (2012)[188], the water-soluble fraction of the atmospheric particles indicated maximum in ECM probability similar to that of NaCl.

Potentiodynamic polarization of tin showed that corrosion potential and the initial current density during anodic polarization in atmospheric electrolyte is higher with respect to NaCl solution at equivalent concentration. On the other hand, the complexity in chemical composition of atmospheric contaminants is reflected by the passivation and oxide layer breakdown that are more pronounced in respect of NaCl polarization curve and by the continuous fluctuation in anodic.

CHAPTER VI – AEROSOL PHASE TRANSITIONS AND ENERGY-SAVING STRATEGIES IN DATA CENTERS

1 – INTRODUCTION

Everyday people connects on internet, visit webpages and share data. Data storage, sharing and fast transfer are fundamental for our lifestyle and economy. But, where these data are stored? Data centers are data banks, which allow most of our data sharing need.

In 2011, data centers were more then 500 thousand and the growth number rate was estimated to increase every year (source: http://www.datacenterdynamics.com/). In 2013, U.S. data centers only consumed about 91 billion kWh of electricity, an amount of the same order of magnitude to that produced by 34 coal-fired power plants (500 MW)[189]. A report of the NRDC (2014)[189] estimated data centers energy consumption could increase of about 140 billion kWh/year by 2020 and Greenpeace International forecasts the energy demand of data centers would growth by 81% by the same year[190].

In the last decades many methods to increase the data centers energy efficiency were developed in order to reduce the economical impacts due to these high energy demand. The energy efficiency is usually indicated with the index *power usage effectiveness* (PUE), based on the relative consumption of the informatics technologies and the electricity demand by data center:

$$PUE = \frac{total\ electricity\ provided\ to\ data\ center}{IT\ electricity\ usage} \qquad (Eq.6.1)$$

PUE (always higher than 1) indicates that the more the ratio is close to 1, the best the energy efficiency is. Traditional PUE for data centers with close loop cooling systems is higher then 2.00[191].

Typical way to decrease the PUE value is decrease the demand for the cooling systems, which can represent about 40% of the overall energy consumption. In this regards, the direct free-cooling system (DFC) is one of the most used technique[192]. This consists in using filtered external air, which is forced within the data center by means of funs in order to remove the heat generated by the electrical circuits activity.

Even though DFC system usage is characteristic for different data centers in order to optimize its use, a resistance in exploiting DFC is due to the increase in circuits exposure to gaseous and atmospheric particle contaminants. In this regards, the American Society of Heating, Refrigerating and Air-conditioning Engineers (ASHRAE) defined both thermal[193] (Table 9) and contamination[194] level in order to avoid electrical failures.

Table 9 Thermal guidelines defined by ASHRAE for data centers[193]

		Dry-bulb wet temperature	Humidity range	Maximum dew point
Recommended				
Class A1 and A4		291 - 300 K	278.6 K to 60% RH and 288 K DP	-
Allowable				
Class	A1	288 - 305 K	20 - 80%	290
Class	A2	283 - 308 K	20 - 80%	294
Class	A3	278 - 313 K	8 - 85%	297
Class	A4	278 - 318 K	8 - 90%	297

On the other hand, low attention was paid in considering atmospheric aerosols physical state. As stated in Chapter V, aerosols can form an electrolytic solution able to cause corrosion and ECM even below the thresholds defined by ASHRAE guidelines. In addition, due to the phase transitions hysteresis, aqueous aerosols can deposit on circuits surfaces even below the DRH. Therefore, the safety limits should be identified considering the aerosols chemical composition and their history.

In this chapter, the aerosols physical states are taken into account in order to estimate the PUE values which results optimizing DFC system usage and with a high ITs protection.

1.1 Case study presentation: the ENI Green Data Center

The aerosols deliquescence was considered in the ENI Green Data Center (GDC-ENI, http://www.eni.com/green-data-center/it_IT/pages/home.shtml) design, which was built in order to centralize all of ENI's management IT. For this aim, the GDC-ENI has four rooms for standard computing, each one of a volume of 6000 m^3 (with 800 m^2 of IT installed in each room), and two rooms for high performance computing, each measuring 7000 m^3 (with 1000 m^2 of IT installed in each). Thus a total IT area of 5200 m^2 was planned, with a final installed power of 30 MW (5.8 kW/m^2). Use of the IT causes a 285 K increase in air temperature in the standard computing rooms, and a 293 K increase in the high performance computing rooms. To ensure the effective cooling of the installed IT, the designed air flow system for each computing room is as follows: air from outside enters the building at floor level, passes through the IT, and the resulting hot air exits through the roof, with the aid of the chimney effect. Cooling air (supplied mechanically) flows through the standard and high performance computing rooms at rates of $1.25 \cdot 10^6$ m^3 h^{-1} and $1.26 \cdot 10^6$ m^3 h^{-1}, respectively; this means an air exchange rates of 208 h^{-1} and 179 h^{-1}, respectively. Moreover, the set room temperature is 298 K; it has been demonstrated that above

this temperature, IT exponentially increases demand for internal fan power for cooling purposes[193].

The GDC-ENI was designed in order to minimize the energy demand of the whole data center (E_{tot}). This was modelled as follows:

$$E_{tot}(t) = E_{IT} + E_L + E_{EL} + E_F(t) + E_{HTC}(t) + E_{LTC}(t) + E_E(t) \qquad (Eq.\ 6.2)$$

$E_{tot}(t)$ represents the 1-hour averaged energy consumption. Since the data center was not realized yet, the first three parameters in Eq. 6.2 were considered time-independent whereas the remaining are since they depend on the external air conditions.

E_{IT}, E_L and E_{EL} represents the hourly energy consumption of IT (30 MWh), lighting (360 kWh) and energy losses estimated (2 MWh) including the UPS losses, electricity load dispersion and distribution. Energy losses were decreased using ultra-high-efficiency transformers and UPS.

$E_F(t)$, $E_{HTC}(t)$, $E_{LTC}(t)$ and $E_E(t)$ are the energy demanded by fans, high-temperature chillers, low-temperature chillers and evaporation units, respectively. Decrease in funs energy consumption was planned avoiding the use of inverters for funs but choosing those with adjustable blade inclination (between 37° and 48°). The low-temperature chillers dry the air which is planned to be successfully treated in order to heat removal by the high-temperature chillers. When the DFC has to be avoided, this allows to constantly recirculating the same dehumidified air within the data centers and it has to be treated for further heat removal generated by IT. Finally, the evaporation unit allows to humidified the air whenever it reaches an RH values below the threshold suggested by ASHRAE.

In order to maximize the use of the DFC, avoiding IT failures, a feasibility study was carried out.

The GDC-ENI was designed in order to locate it in Italy, at Sannazzaro de' Burgondi in the Po Valley (45°05'59"N, 8°51'40"E), close to the largest ENI power generation plant (1 GW natural gas turbine) in Northern Italy. This ensures a continuous power supply to the data center, and avoids any interruption in the power supply. However, the Po Valley is an environmental hot spot with the worst atmospheric aerosol pollution in Europe[19,23,77,79]; furthermore, the presence of a Power Plant close to the GDC-ENI called for solutions to be found to the potential problem of aerosol contamination within the data center.

The $PM_{2.5}$ concentrations level were discussed in Ferrero et al. (2013)[149] considering number size distributions and the capability to penetrate the filtering systems. This consists of 456 MERV13 (Minimum Efficiency Reporting Value) filters, also recommended by ASHRAE[193,194], providing a total filtering surface of 165 m^2, which corresponds to a maximum flow rate of 2763 $m^3\ h^{-1}$ for each individual filter.

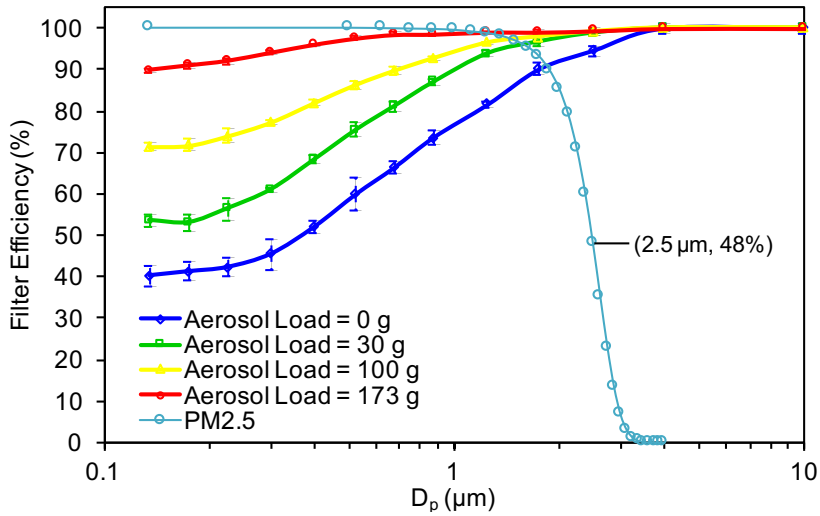

Figure 50 Filter efficiency at different aerosols loadings compared with the collection efficiency for $PM_{2.5}$.

Ferrero and co-authors[149] showed that the MERV13 filter's efficiency increases with increasing particle size, up to 100% at 3 µm (Figure 50). Thus, the authors highlighted that overall filter efficiency is lower than 100%[195], and stated the need to assess the chemical properties of those particles capable of getting into the GDC-ENI despite the filters. For this reason, $PM_{2.5}$ samples, smaller than those guaranteeing the 100% efficiency of MERV13 filters, were sampled and chemically analyzed in order to estimate their phases by means of the E-AIM II, once their chemical composition was known.

These estimations were the topic of *Aerosol corrosion prevention and energy saving strategies in the designing of Green Data Center*[149] published on *Environmental Science and Technology* in 2013 and the results are presented in Section 2.1 of the present chapter.

Beside this study, a further step was carried out used a precautionary threshold for both DRH and CRH values obtained as the annual average resulted by the conductance method. The results were published on *International Journal of Environmental Science and Technology* in 2015 in a paper titled *Determination of Aerosol Deliquescence and Crystallization Relative Humidity for Energy Saving in Free-Cooled Data Centers*[76] and they are reported in Section 2.2.

Finally, the importance of coupling a highly engineered cooling system and the knowledge of the aerosols physical state is highlighted showing the PUE values obtained basing on aerosol properties only.

It has to be pointed out that, even if aerosols properties are site-specific, the method here reported is widely applicable.

2 – DIRECT FREE-COOLING USAGE AND AEROSOLS HYDRATION STATE

2.1 Energy efficiency considering modelled DRH

2.1.1 Aerosol chemical characterization

Since aerosols chemistry drives the phase transition processes (Chapter III), sampling and chemical characterization was firstly carried out as described in Chapter II. Ionic fraction was found to be 35±1%, during IOP_1, and 23±1% during IOP_2 (Table 10). These results confirm those of previous studies conducted in the Po Valley[21,196]. The main $PM_{2.5}$ ionic components were NO_3^-, SO_4^{2-} and NH_4^+ (91-94% of the whole ions during both IOP_1 and IOP_2,). Other cations (K^+, Na^+, Mg^{2+}, Ca^{2+}) and carboxylic acids accounted for ~1% of PM, while Cl^- displayed the very low concentrations: 0.3-0.6% of $PM_{2.5}$ during both IOP: the risk associated with Cl^- was considered negligible. In Table 10, mono and di-carboxylic acids are grouped with Cl^-, F^- and PO_4^{2-} (indicated as 'other anions').

Table 10 Chemical composition of $PM_{2.5}$, measured at ENI-Green Data Center during IOP_1 and IOP_2. (σ indicates the standard deviation). The slope and R^2 for the ionic balance equation (bases vs. acids ion equivalents), i.e. the degree of neutralization, are also reported.

		Chemical composition (% w/w)					Degree of neutralization	
		NO_3^-	SO_4^{2-}	NH_4^+	Other cations	Other anions	Slope	R^2
IOP_1	mean	20.1	5.6	7.0	0.9	0.6	1.0	0.988
	±σ	12.8	3.4	4.4	0.8	0.7	<0.1	-
IOP_2	mean	6.5	10.3	4.7	0.7	0.5	0.9	0.988
	±σ	6.1	7.3	2.9	0.6	0.9	<0.1	-

Due to the important role played by NO_3^-, SO_4^{2-} and NH_4^+, which constitute the majority of the aerosol, their behavior was investigated. During IOP_1, NO_3^- accounted for 20.1% of $PM_{2.5}$ mass, while SO_4^{2-} accounted for 5.6%. Conversely, during IOP_2, NO_3^- accounted for only 6.5% while SO_4^{2-} accounted for 10.3%.

This behavior reflects the seasonal differences observed in the Po Valley (Chapter III), and affects the DRH (section 2.2.2). During IOP_1, the temperature was lower (285.3±0.2 K) than during IOP_2 (297.0±0.2 K): in IOP_1 gas to particle conversion of NH_4NO_3, and an increase in its gaseous precursors (due to the lower mixing height), enhance its condensation; conversely, higher temperatures and photochemical reactions (IOP_2) enhance the $(NH_4)_2SO_4$ aerosol content[19,77].

The offsetting of the two aforementioned effects meant that NH_4^+ remained fairly constant during both IOP (4-7% in both cases) and resulted in low aerosol acidity. Table 10 shows the

slope and R^2 for this ionic balance. During both IOP, the condition of all $PM_{2.5}$ was close to neutrality (slopes close to 1); only a small amount of H^+ were not neutralized.

These neutral conditions are important for the use of the DFC system in the GDC-ENI, due both to the corrosive capacity of acidic species[197–199] and to the low DRH values usually associated with the presence of such acidic species[106,117].

Finally, the E-AIM model was applied to the chemical composition of $PM_{2.5}$.

2.1.2 Aerosol deliquescence estimated by E-AIM II model

Figure 51 summarizes DRH frequency distributions for $PM_{2.5}$ resulted from E-AIM II estimations. DRH values fell within a broad range of 40-80%. Within this range, the most abundant DRH were found in the 60-65% range, with a percentage frequency of 43%. Thus, averaged DRH for $PM_{2.5}$ accounted for 60.8±0.7% RH (IOP_1) and 62.4±0.9% RH (IOP_2).

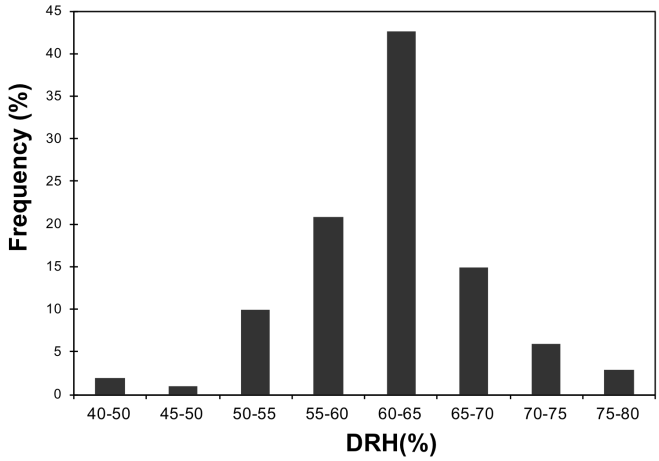

Figure 51 DRH frequency distribution at GDC-ENI site (Sannazzaro de' Burgondi).

These values clearly reflect the influence of aerosol chemistry: nitrates were more abundant in IOP_1, whereas sulfates were more abundant in IOP_2 (Table 10). According to Potukuchi and Wexler's method[106], the sulfate fraction was 0.20±0.02, during IOP_1, and 0.59±0.03 during IOP_2; the ammonium fraction remained fairly constant: 0.95±0.01 and 0.84±0.01 during both IOP. These results explain the higher average DRH during IOP_2.

2.1.3 PUE estimations with modelled DRH

The average DRH values were compared to the ASHRAE (2011) guideline values: during both IOP they were higher than the "recommended" limit but lower than the "allowable" one (Sect. 1).

All the averaged DRH were found to be higher than 60%. Moreover, DRH was above 60% for 69% (IOP_1) and 64% (IOP_2) of the time, respectively. Thus, 60% of RH was chosen as the

upper limit for the DFC operating cycle in order to prevent, as a rule, the corrosive effects of the aerosol.

This result allowed to optimize the cooling cycle by developing a new thermodynamic operating area. This area optimized the "allowable" ASHRAE[194] guidelines, including the deliquescence properties estimated at the GDC-ENI construction site. The new thermodynamic operating area was as follows: 1) lower "allowable" limits of ASHRAE (288.15 K, 20% of RH) were maintained to maximize energy efficiency; 2) the maximum temperature was set at 298.15 K; 3) maximum RH was 60% in accordance with the estimated aerosol DRH, in order to prevent any IT failure due to the aerosol; 4) the use of a maximum dew point limit (and thus of specific humidity) was avoided, as it does not affect the hydration level of the aerosol. According to the aforementioned guidelines, Figure 52 shows the DFC operating area within the GDC-ENI.

As already mentioned, DFC is the preferred data center option from the energy saving point of view. Thus, in order to assess the theoretical energy efficiency of the GDC-ENI, the thermodynamic limits for the DFC were applied, considering one year's meteorological data gathered at San Nazzaro de' Burgondi (as provided by the local Environmental Protection Agency - *ARPA Lombardia*).

As a result, it was estimated that the DFC system could be operated for 78% of the time. It was thus possible to estimate the time variation of the data center's energy consumption and its Power Usage Effectiveness (PUE): this latter index reached a value of 1.20, which is lower than that of both traditional air conditioning data centers (PUE=2.04), and of other data centers adopting DFC (PUE=1.42-1.46)[191]. These results are given because even if the maximum allowed RH is 60%, this is an indoor limit (at 298 K); although outdoor events with RH of over 80% may happen, in most such events the air temperature is below 298 K. Thus, because the GDC-ENI was designed to partially mix the outdoor air supply with re-circulated air in order to attain a temperature of 298 K, the RH of the outdoor-supplied air decreases, enabling us to use it even when outdoor RH is beyond the set limits.

A PUE of 1.20 means that in one year, for every 1 kW of installed IT, the calculated energy saving is 7.4 MWh (81%; 221 GWh for the entire 30 MW of IT), compared to traditional air conditioning data centers (PUE=2.04), and 2.1 MWh (55%; 63 GWh for the entire 30 MW of IT) compared to other data centers adopting the DFC system (PUE=1.42-1.46). This results in both environment and economic savings; considering a CO_2 emission factor of 362 gCO_2 kWh^{-1} (European Environment Agency, EEA: http://www.eea.europa.eu/) and an energy cost of 0.15 € kWh^{-1}, the environment and economic savings (for each kW of IT) are as follows: 2.7 t of CO_2 and € 1,100 (80 kt of CO_2 and € 33 mln. for the entire 30 MW of IT), compared to traditional air conditioning data centers (PUE=2.04); and 0.8 t of CO_2 and € 300 (23 kt of CO_2 and € 9.5 mln. for the entire 30 MW of IT) compared to other data centers adopting DFC systems (PUE=1.42-1.46).

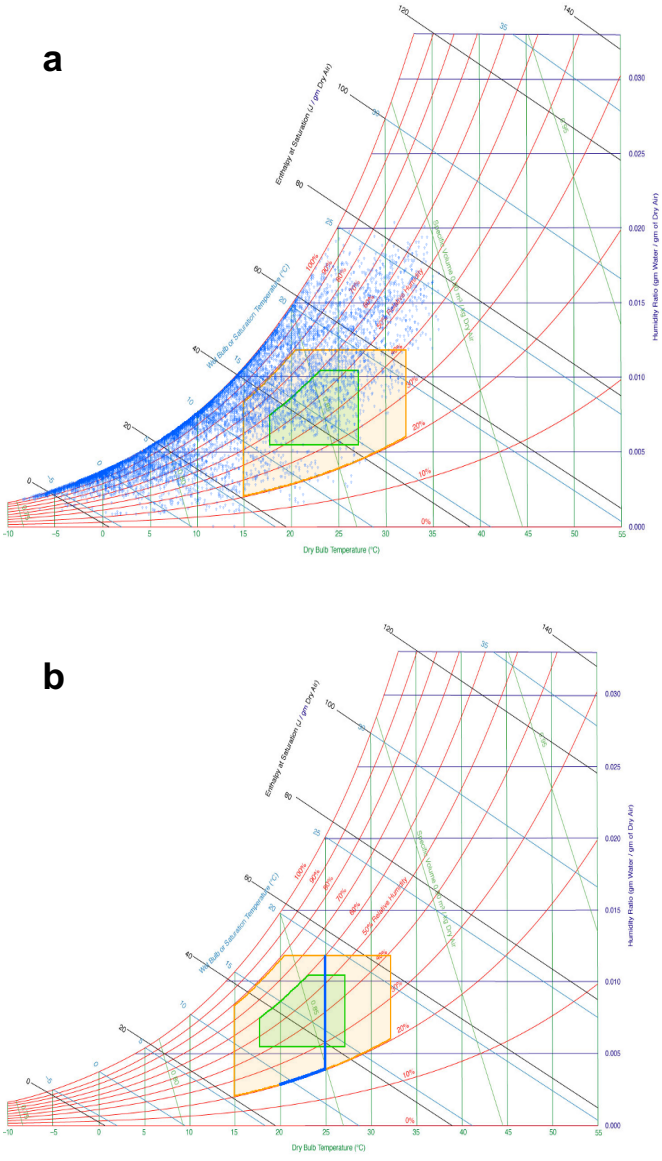

Figure 52 Psychrometric chart of the thermodynamic conditions obtained outdoor(a) and within the GDC-ENI (b); ASHRAE "allowable" (orange) and "recommended" (green) areas are also plotted. Blue dots indicates the air conditions outside the GDC-ENI.

2.2 Energy efficiency considering experimental data

The experimental results obtained by means of the conductance method (Chapter II) on a preliminary subset of 55 $PM_{2.5}$ samples. For this subset, averaged DRH and CRH were found to be 60.5±8% RH and 47.9±0.7% R, respectively. These values were taken into account in order to estimate the time in which aerosols were in hydrated state during 2006-2009 period, i.e. the period in which those samples were collected. The computation of the hydration time indicates that 52% of the time the aerosols were dry because ambient RH was below CRH (36%) or because of the lower branch of the hysteresis loop (16%). In the remaining time (48%) the aerosols were hydrated mostly because RH was higher than DRH (39%) or because of the upper metastable branch (9%).

The aforementioned DRH and CRH were then used in the calculation of the PUE value: the lower moisture limits of ASHRAE (20% RH) were kept to enhance energy efficiency whereas the upper threshold was set 48% RH and 60% RH in function of the history of the ambient RH in order to consider the hysteresis behavior of the hygroscopic aerosols. The the maximum dew point limit was neglected since it does not influence the hydration state of the aerosols.

As it was expected, the PUE value increased since the operating time of the DFC system was lower in respect of the estimations without considering the hysteresis of aerosols hydration. The PUE value resulted to account for 1.22, therefore – in respect of the PUE obtained by data center which adopted DFC system – the energy saving was estimated to account for 58 GWh (for a 30 MW of installed IT), which means €9 mln and 21 kt CO_2 not emitted.

2.3 – Simulation of pure direct free-cooling based on aerosols physical state only

It has to be noted that a pure free cooling would not obtain similar efficiency results. In this section, it is shown that, even maximizing DFC usage by means of seasonal parameterization of RH limits (derived from seasonal DRH and CRH), the free-cooling system would be used very few times if it would not be coupled with recirculating system which mix the supplied outdoor air with the recirculating one, decreasing the resulting air RH but minimizing the use of high-temperature chillers for the recirculated air as well.

2.3.1 Simulation design

The GDC-ENI has been active since the end of 2013. One-year of external meteorological data (RH and T, from November 1, 2014 to October 31, 2015) were provided by GDC-ENI in order to evaluate the aerosols physical states and to estimate the conditions in which DFC was allowable with the goal to prevent corrosion processes and IT failures. In this regards, some new data were also provided by GDC-ENI concerning the air T at the entry of data rooms, which was not set at 298 K for the entire year. In fact, indoor T was then seasonally modulated in order to provide a better cooling during the cold season (WI) and to reduce the use of high-temperature

chillers during the warmest season (SU), air T (hereinafter called 'target T') was set at 291 K during WI and 300 K during SU, whereas during SP and FA the T was kept at 298 K.

In this simulation, no changes in RH were simulated because of the mix between outdoor air and modulated recirculated air, whereas they are calculated for only changes in T. Such a similar approach allows to take into account the changes in DRH and CRH following the aerosols dynamics without external influences.

Thus, this simulation is carried out with the following steps:

1. aerosols DRH and CRH are estimated considering the season and the hourly averaged outdoor air temperature;
2. the physical state is evaluated taking into account the phase transition RH at the hourly averaged T, discerning the stable and metastable conditions as well;
3. RH in outdoor condition is recalculated at the internal target T (291 K for WI, 298 K for SP and FA and 300 K for SU season);
4. aerosols DRH and CRH are recalculated at target T;
5. aerosols hydration state is finally recalculated at target T.

The estimation of the outdoor hydration states is fundamental in order to discern the states when RH falls within the hysteresis loop once that the aerosols are forced indoor. The DFC usage was therefore allowed whenever the aerosols were in dry state.

3.2 Results

Seasonal outdoor and indoor air conditions and aerosols phase transitions RH are showed as average (with their standard deviation) in Table 11. In addition, Figure 53 graphically highlights the aerosols physical states during the considered period for both outdoor (a) and indoor (b) conditions.

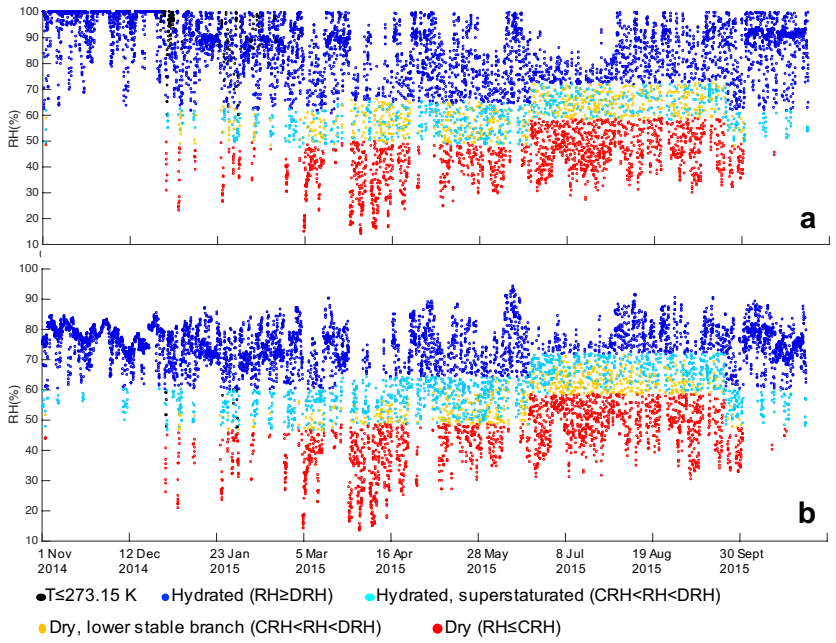

Figure 53 Atmospheric aerosols physical state at GDC-ENI site: a)out of data center, b)inside data center.

The results suggest that during WI, SP and FA, aerosols are in hydrated states for most of the time both outdoor and inside the data center. Even though the RH inside the data center decreases due to the increase in T, both DRH and CRH decrease for the same reason (Chapter III, Sect. 4.4). In Figure 54, the T-dependence of DRH is plotted with the change of RH when the air mass is forced within the data center. Here it is highlighted that, even if the air RH has a higher sensitivity to changes in T, within the considered T range (the starting and ending conditions represents the averaged conditions) the (mean) DRH remains below the (mean) air RH, although the difference decreases. This leads to an increase of the occurrences in which aerosols are in the metastable upper branch of the hysteresis loop. The results are that the hydration time accounts for 6217 hours (meaning 71% of the time) in outside conditions whereas 6293 hours (i.e. 72% of the time) inside the data center.

These conditions were imposed for the calculation of the PUE, which results 1.39±0.14. In fact, the low occurrences in which allowable conditions were estimated – which in this simulation depend on the aerosols physical state only – lead to a small energy saving for the GDC-ENI in respect of how was estimated in Sect. 2 with a PUE of 1.20 and 1.22. Referring to the last one PUE estimated by means of precautionary RH limits and aerosols hysteresis and efficient air

supply, such a PUE of 1.39 means +45 GWh of energy consumption at year, leading to - €6.8 mln of economical saving and +25 kt of CO_2 emitted.

Thus, a pure direct free-cooling guarantees very low energy saving, as demonstrated by the low frequency of activity of this system and the PUE reached (Table 11), which is lower than it is performed by traditional DFC systems anyway.

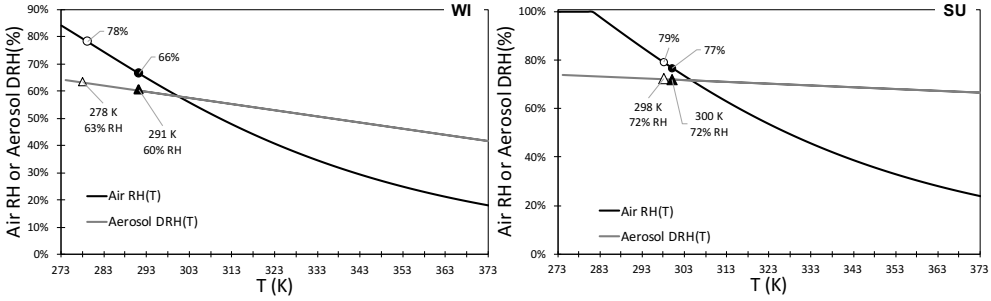

Figure 54 Air RH and DRH in function of the T. Round and triangle markers represents the change in air RH and aerosols DRH, respectively. Open markers represent the average outdoor conditions while the full ones indicates the indoor conditions.

Table 11 Outdoor and indoor air RH and T conditions and aerosols phase transitions relative humidity.

		GDC-ENI, outdoor				GDC-ENI, indoor				Aerosols physical state	
		RH (%)	T (K)	DRH (%)	CRH(%)	RH (%)	T (K)	DRH (%)	CRH (%)	PUE	DFC ON (%)
FA from 01/11/2014	mean	95.9	281.5	63.1	50.3	76.06	298.15	60.3	47.5	1.44	0.3
	±σ	7.8	3.2	0.5	0.5	6.02	–	–	–	0.02	–
WI 2014-2015	mean	79.5	278.3	63.2	49.7	66.73	291.15	60.3	46.7	1.38	14.8
	±σ	18.9	4.2	1.0	1.0	14.55	–	–	–	0.09	–
SP 2015	mean	64.3	291.8	65.1	49.4	58.20	298.15	64.4	48.7	1.34	38.1
	±σ	21.0	6.2	0.7	0.7	17.20	–	–	–	0.14	–
SU 2015	mean	64.8	298.2	72.2	58.7	62.18	300.15	72.1	58.6	1.43	54.4
	±σ	17.3	5.6	0.4	0.4	13.09	–	–	–	0.20	–
FA until 01/11/2015	mean	82.5	287.3	62.2	49.4	70.29	298.15	60.3	47.5	1.37	8.0
	±σ	17.3	5.6	0.7	0.7	12.05	–	–	–	0.07	–

3 – CONCLUSIONS

In this chapter, the implications of aerosols physical states were addressed to energy saving strategies in data centers. Direct-free cooling (DFC) system – one of the most performance solution to energy efficiency increasing – uses external air in order to cool IT technologies. On the other hand, its use has to take into account the aerosols hydration in order to avoid deposition of aqueous particles on PCBA surfaces.

As it was discussed in Chapter V the used method does not allow the observation of corrosive processes on tin when aerosols were in metastable state (upper branch of the hysteresis curve), a precautionary approach was applied in order to estimate the power usage effectiveness (PUE) of the GDC-ENI, built at Sannazzaro de' Burgondi (Po Valley, Italy).

The results showed that considering hysteresis, i.e. avoiding the entrance of aqueous aerosols, PUE increases of less than 2% (PUE=1.22) in respect of hysteresis omitting (1.20). Such a PUE value leads to interesting energy saving amounts for every 1 kW of IT installed (1.9 MWh $kW^{-1}year^{-1}$) with a consequent economical saving and reduction in CO_2 emission.

Such an energy efficiency cannot be reached by means of a pure DFC. In fact, at Sannazzaro de' Burgondi site aerosols hydration time was estimated to be very high (~ 71% of the time). This would lead to a DFC usage for very few time, increasing the PUE up to 1.39. Even if this value is lower than the average data centers that use DFC systems (i.e. 1.42-1.46), the energy saving cannot be attributed entirely to the DFC usage. Because of this, outdoor air – once forced within the data centers – is mixed with recirculated air, which has different temperature and very low RH. This mix allows to dry and warm up external air.

Some factors which were not taken into account suggest that a further decrease in PUE could be reached.

When aerosols experienced warmer T, their DRH and CRH decrease while the air RH decreases faster. This means that once the air reached the PCBA, further heating occurs decreasing RH and phase transition relative humidity as well. Even if a spatial heterogeneity was pointed out in some works[200,201], temperature of PCBA surface is higher than 323 K. Therefore, such a heating could cause aerosols crystallization leading to deposition of solid particles on circuits surface.

In addition, higher temperatures lead to a loss of semi-volatile compounds from aerosols. Among them, it is well-known that AN tends to volatilize[16,69] at high temperatures. Beside this, it was demonstrated that it lowers both DRH and CRH (Chapter III). Therefore, the loss of this compound, which represents an important fraction of the inorganic ones, could partially compensate the decrease in DRH and CRH due to the T.

These considerations suggest that the thermodynamic air operating conditions of the DFC systems could be extended further. In this regards, aerosols phase transitions and their

temperature-dependence have to be experimentally determined together with a detailed characterization of the air dynamics within the data center.

A little irony

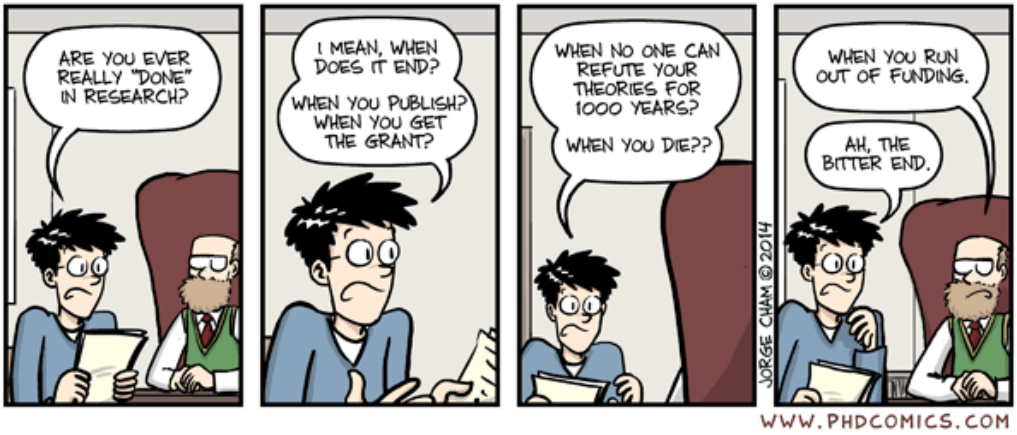

CHAPTER VII – CONCLUSIONS

This work provided a significant improvement on the knowledge of the conditions at which real atmospheric aerosols are formed by an aqueous fraction or by a solid phase only. This was obtained with the development of a method based on the changes in electrical conductive properties of aerosols collected as $PM_{2.5}$ on a hydrophobic and poorly conductive filter (PTFE). The aerosols samples, exposed to RH ramps, showed that when solid-to-liquid transition occurred, the electrical signal sharply increased, whereas a correspondent drop indicated the water-soluble fraction crystallization.

This method confirmed that atmospheric aerosols do not have the same behavior during increasing and decreasing RH ramps. This is because aerosols deliquescence and crystallization were identified at different RH conditions, therefore highlighting the existence of a hysteretic behavior. In additions, samples collected during different seasons in Milan (Po Valley, Italy) showed that DRH and CRH are not constant among different periods but a dependence on the chemical composition of the water-soluble fraction was observed. In fact, high content in nitrate ions drives the phase transitions at lower RH conditions; this effect is more pronounced during cold periods, i.e. winter, since particle-phase ammonium nitrate is promoted by low temperatures and high RH conditions. Deliquescence was recognized to occur between 52% and 59% RH while the crystallization processes were observed between 44% and 48% RH. On the contrary, low nitrate contents increases the relative importance of ammonium sulfate which strongly leads to higher DRH and CRH, particularly during warm seasons, i.e. summer, which were found within the ranges 68-73% RH and 59-63% RH, respectively. Spring and autumn present intermediate nitrate-to-sulfate ratio. As a consequence, both DRH and CRH were found to fall between those of summer and winter. On the other hand, the lack of the characterization of the organic compounds avoid the evaluation of the role of this fraction on the phase transitions.

Although this dependence was demonstrated, it was found that thermodynamic models are not applicable for atmospheric aerosols DRH predictions since a number of different compounds contribute to the overall DRH (and CRH as well) whereas the models considers only the main inorganic salts. As a result, the aerosols water uptake was found to be underestimated by the E-AIM II model if compared to the results obtained by a gravimetric method, developed firstly as comparison for the conductance method and then in order to estimate the hygroscopic growth of aerosols samples.

The phase transitions and their hysteresis were discussed highlighting their implications.

Many climatic models estimate the effects of aerosols on radiative forcing evaluating their optical properties, basing on a parameterization of their growth in function of the air RH. On the other hand, even if a growing number of works are developing some algorithms that take into account both aqueous and solid particles, a proper parameterization is still far. In this work, it

was estimated that aerosols hygroscopic growth factor can change up to 23% within the hysteresis loop range depending on their physical state. In addition, the same factor affects the estimations in air quality monitoring from remote sensing, e.g. LIDAR and MODIS. Aerosols concentrations within the planet boundary layer are commonly evaluated with these techniques in order to overcome the spotted characterization of air quality. On the other hand, as stated by some authors, ground-based measurements and remote estimations often disagree since the firsts are carried out at low RH whereas the seconds are retrieved from data obtained at ambient RH. Therefore, it was estimated that an omission of the hysteresis loop leads to an error up to 20% in $PM_{2.5}$ concentrations. A calculation of the hydration time of atmospheric aerosols suggested that these conditions occur about 19% of the time during winter and 5% of the time during summer when MODIS sensors (on TERRA and AQUA satellite platform) pass above Po Valley (10 a.m. – 2 p.m.). These findings point out that taking into account aerosols hysteretic behavior can substantially improve remote sensing estimations whose uncertainty in $PM_{2.5}$ concentrations are in the order of ±30%.

The calculation of the time in which aerosols are solid or in aqueous phase and the dissolution-crystallization cycles were used in order to evaluate the risk of stone decay occurrences. For this application, the hydration time was considered as the time in which aqueous aerosols promote chemical reactions on surfaces. It was estimated that these processes likely occur during winter seasons. The number of dissolution-crystallization cycles indicates the probability of aqueous electrolytes penetration within a porous media and the mechanic stress due to formations of solid inclusions when crystallization occurs. In respect of winter, summer seasons present higher hazard for mechanical stress whereas the chemical one seems less important. On the other hand, the highest hazard is reached during fall and spring seasons, due to high hydration time and number of dissolution-crystallization cycles.

Finally, the aerosols hygroscopic behavior was preliminarily investigated in relation to tin corrosion. Tin is the main metal used in solder alloys in printed circuit boards assembly because of its low cost, low melting point and relative resistance to electrochemical migration. On the other hand, in this work it was demonstrated that when atmospheric particles contaminate the circuit surface, a thin water-layer can form leading to corrosion processes. It was here shown that these conditions can occur even below 70% RH. Aerosols chemical composition, surrounding air temperature and RH variation rate are found to affect the RH conditions of circuits failure.

Circuit boards were contaminated accelerating aerosols deposition (~1 day) by means of a rotating particle impactor prototype, able to deposit a round spot with a diameter of 2.00 cm on a not-filtering substrate. In addition, aerosol water-soluble fraction was also extracted in ultra-pure water and potentiodynamic polarization measurements were carried out in order to provide information about the corrosion mechanisms of aerosols induced corrosion. The results suggested that atmospheric electrolytes solution containing affect tin passivation and anodic dissolution.

Because of their role in corrosion, aerosols contamination of electronic circuits has to be avoided, especially in sensitive environment such as data centers. Direct free-cooling is nowadays one of the widely used solution in order to decrease the energy consumption of air-cooling systems. This consists in forcing high volume amounts of outdoor air inside the data centers to remove the heat generated by the circuits activities. Even though the airflow is filtered before entering inside the data rooms – where IT are stored – it was demonstrated that the filtration efficiency decreased for submicrometric particles. Therefore, it is fundamental to consider the aerosols physical state whenever the direct free-cooling system is used.

In this work, the ENI Green Data Center (GDC-ENI, at Sannazzaro de' Burgondi, Po Valley, Italy) was considered as case-study in order to show how aerosols hydration states can be taken into account in order to maximize energy efficiency reducing failure risks. By this aim, GDC-ENI cooling system is designed in order to modulate the incoming air volume and mixing it with warmer and dryer recirculated air. A lower limit of 20% RH is always set in order to avoid electrostatic charges.

Three simulations were presented based on precautionary thresholds for free-cooling system usage and the energy efficiency was expressed in term of PUE (power usage effectiveness), that is the ratio of the total energy demanded by the data center and the energy consumption of the IT only. The first considered an average modelled DRH (by means of E-AIM II model) as threshold for acceptable entering air, neglecting the hysteresis of aerosols in response to relative humidity: PUE was estimated to account for 1.20. The second method avoided the entrance of aqueous metastable phase particles, therefore considering the hysteresis. In this case, an averaged experimental DRH and CRH were considered. Since the hydration time increased, the PUE was estimated to increase up to 1.22. The third simulations assumed a pure direct free-cooling without mixing with recirculated air. Even optimizing the time of activities of free-cooling by means of averaged seasonal DRH and CRH, the high hydration time led to very low occurrences of acceptable air conditions. Thus, a PUE of 1.39 was estimated.

These results showed that a high engineering system which take into account the aerosols properties can lead to an interesting energy saving (1.9 MWh for each 1 kWh of installed IT) in respect of the averaged efficiency of the other free-cooled data centers (PUE 1.42-1.46). This is a great opportunity in order to substantially reduce CO_2 emission (-700 t for each kWh of installed IT). This means that for a 30 MWh of installed IT (proper of GDC-ENI), energy (-58 GWh), economical (- €9 mln) and CO_2 emission (- 21 kt) savings could be reached and coupled with aerosols corrosion prevention.

A little irony

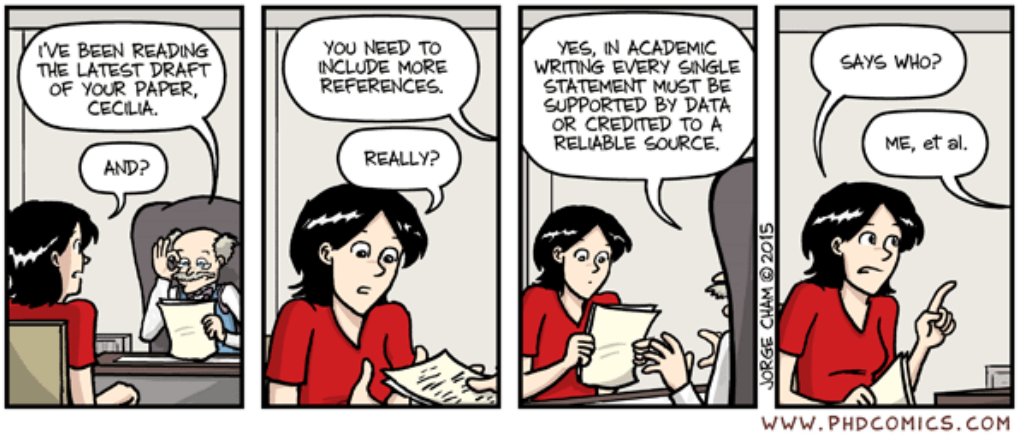

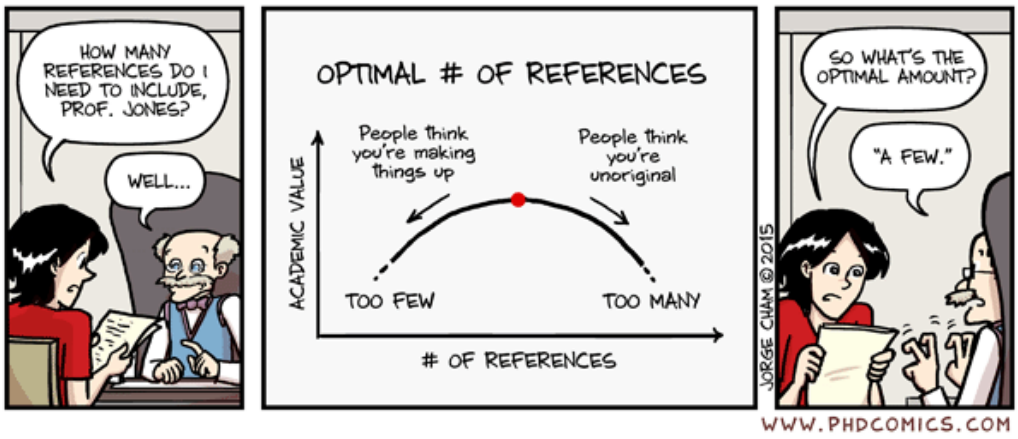

REFERENCES

(1) Kulkarni, P.; Baron, P. A.; Willeke, K. *Aerosol Measurement*; Kulkarni, P., Baron, P. A., Willeke, K., Eds.; John Wiley & Sons, Inc.: Hoboken, NJ, USA, 2011.

(2) Seinfeld, J. H.; Pandis, S. N. *Atmospheric Chemistry and Physics: From Air Pollution to Climate Change*, II.; John Wiley & Sons Inc., Ed.; Wiley-Interscience, 2006.

(3) Kulmala, M.; Vehkamäki, H.; Petäjä, T.; Dal Maso, M.; Lauri, A.; Kerminen, V.-M.; Birmili, W.; McMurry, P. H. Formation and growth rates of ultrafine atmospheric particles: a review of observations. *J. Aerosol Sci.* **2004**, *35* (2), 143–176.

(4) Perrone, M. G.; Gualtieri, M.; Ferrero, L.; Lo Porto, C.; Udisti, R.; Bolzacchini, E.; Camatini, M. Seasonal variations in chemical composition and in vitro biological effects of fine PM from Milan. *Chemosphere* **2010**, *78* (11), 1368–1377.

(5) Gualtieri, M.; Mantecca, P.; Corvaja, V.; Longhin, E.; Perrone, M. G.; Bolzacchini, E.; Camatini, M. Winter fine particulate matter from Milan induces morphological and functional alterations in human pulmonary epithelial cells (A549). *Toxicol. Lett.* **2009**, *188* (1), 52–62.

(6) Pöschl, U. Atmospheric aerosols: composition, transformation, climate and health effects. *Angew. Chem. Int. Ed. Engl.* **2005**, *44* (46), 7520–7540.

(7) Perrino, C.; Catrambone, M.; Dalla Torre, S.; Rantica, E.; Sargolini, T.; Canepari, S. Seasonal variations in the chemical composition of particulate matter: a case study in the Po Valley. Part I: macro-components and mass closure. *Environ. Sci. Pollut. Res. Int.* **2013**, *21* (6), 3999–4009.

(8) Pant, P.; Harrison, R. M. Critical review of receptor modelling for particulate matter: A case study of India. *Atmos. Environ.* **2012**, *49*, 1–12.

(9) Liu, Y.; Minofar, B.; Desyaterik, Y.; Dames, E.; Zhu, Z.; Cain, J. P.; Hopkins, R. J.; Gilles, M. K.; Wang, H.; Jungwirth, P.; et al. Internal structure, hygroscopic and reactive properties of mixed sodium methanesulfonate-sodium chloride particles. *Phys. Chem. Chem. Phys.* **2011**, *13* (25), 11846–11857.

(10) Chameides, W. L.; Stelson, A. W. Aqueous-Phase Chemical Processes in Deliquescent Sea-Salt Aerosols ' A Mechanism That Couples the Atmospheric Cycles of S and Sea Salt. *J. Geophys. Res.* **1992**, *97*, 565–580.

(11) Jacobson, M. C.; Hansson, H. Organic atmospheric aerosols: review and state of the science. *Rev. Geophys.* **2000**, No. 1998, 267–294.

(12) Andreae, M. O.; Gelencés, A. Black carbon or brown carbon ? The nature of light-absorbing carbonaceous aerosols. *Atmos. Chem. Phys.* **2006**, *6*, 3131–3148.

(13) Ge, X.; Wexler, A. S.; Clegg, S. L. Atmospheric amines – Part I. A review. *Atmos. Environ.* **2011**, *45* (3), 524–546.

(14) Perrone, M. G.; Gualtieri, M.; Consonni, V.; Ferrero, L.; Sangiorgi, G.; Longhin, E.; Ballabio, D.; Bolzacchini, E.; Camatini, M. Particle size, chemical composition, seasons of the year and urban, rural or remote site origins as determinants of biological effects of particulate matter on pulmonary cells. *Environ. Pollut.* **2013**, *176*, 215–227.

(15) Sangiorgi, G.; Ferrero, L.; Perrone, M. G.; Bolzacchini, E.; Duane, M.; Larsen, B. R. Vertical distribution of hydrocarbons in the low troposphere below and above the mixing height: tethered balloon measurements in Milan, Italy. *Environ. Pollut.* **2011**, *159* (12), 3545–3552.

(16) Sangiorgi, G.; Ferrero, L.; Ferrini, B. S.; Lo Porto, C.; Perrone, M. G.; Zangrando, R.; Gambaro, a.; Lazzati, Z.; Bolzacchini, E. Indoor airborne particle sources and semi-volatile partitioning effect of outdoor fine PM in offices. *Atmos. Environ.* **2013**, *65*, 205–214.

(17) Duan, J.; Bi, X.; Tan, J.; Sheng, G.; Fu, J. The differences of the size distribution of polycyclic aromatic hydrocarbons (PAHs) between urban and rural sites of Guangzhou, China. *Atmos. Res.* **2005**, *78* (3-4), 190–203.

(18) Yao, X.; Fang, M.; Chan, C. K.; Ho, K. F.; Lee, S. C. Characterization of dicarboxylic acids in PM2.5 in Hong Kong. *Atmos. Environ.* **2004**, *38* (7), 963–970.

(19) Carbone, C.; Decesari, S.; Mircea, M.; Giulianelli, L.; Finessi, E.; Rinaldi, M.; Fuzzi, S.; Marinoni, a.; Duchi, R.; Perrino, C.; et al. Size-resolved aerosol chemical composition over the Italian Peninsula during typical summer and winter conditions. *Atmos. Environ.* **2010**, *44* (39), 5269–5278.

(20) Fisseha, R.; Dommen, J.; Gutzwiller, L.; Weingartner, E.; Gysel, M.; Emmenegger, C.; Kalberer, M.; Baltensperger, U. Seasonal and diurnal characteristics of water soluble inorganic compounds in the gas and aerosol phase in the Zurich area. *Atmos. Chem. Phys.* **2006**, *6* (7), 1895–1904.

(21) Perrone, M. G.; Larsen, B. R.; Ferrero, L.; Sangiorgi, G.; De Gennaro, G.; Udisti, R.; Zangrando, R.; Gambaro, a; Bolzacchini, E. Sources of high PM2.5 concentrations in Milan, Northern Italy: molecular marker data and CMB modelling. *Sci. Total Environ.* **2012**, *414*, 343–355.

(22) Kaiser, J. Mounting evidence indicts fine-particle pollution. *Science*. 2005, pp 1858–1861.

(23) Ferrero, L.; Cappelletti, D.; Moroni, B.; Sangiorgi, G.; Perrone, M. G.; Crocchianti, S.; Bolzacchini, E. Wintertime aerosol dynamics and chemical composition across the mixing layer over basin valleys. *Atmos. Environ.* **2012**, *56*, 143–153.

(24) Kuwata, M.; Martin, S. T. Phase of atmospheric secondary organic material affects its reactivity. *Proc. Natl. Acad. Sci. U. S. A.* **2012**, *109* (43), 17354–17359.

(25) Michel Flores, J.; Bar-Or, R. Z.; Bluvshtein, N.; Abo-Riziq, a.; Kostinski, a.; Borrmann, S.; Koren, I.; Rudich, Y. Absorbing aerosols at high relative humidity: linking hygroscopic growth to optical properties. *Atmos. Chem. Phys.* **2012**, *12* (12), 5511–5521.

(26) Petters, M. D.; Kreidenweis, S. M. A single parameter representation of hygroscopic growth and cloud condensation nucleus activity. *Atmos. Chem. Phys.* **2007**, *7*, 1961–1971.

(27) Dougle, P. G.; Veefkind, J. P.; ten Brink, H. M. Crystallisation of mixtures of ammonium nitrate, ammonium sulphate and soot. *J. Aerosol Sci.* **1998**, *29* (3), 375–386.

(28) Pant, A.; Parsons, M. T.; Bertram, A. K. Crystallization of aqueous ammonium sulfate particles internally mixed with soot and kaolinite: crystallization relative humidities and nucleation rates. *J. Phys. Chem. A* **2006**, *110* (28), 8701–8709.

(29) Eom, H.; Gupta, D.; Li, X.; Jung, H.; Kim, H.; Ro, C. Influence of Collecting Substrates on the Characterization of Hygroscopic Properties of Inorganic Aerosol Particles. *Anal. Chem.* **2014**.

(30) Semeniuk, T.; Wise, M.; Martin, S.; Russell, L.; Buseck, P. Water uptake characteristics of individual atmospheric particles having coatings. *Atmos. Environ.* **2007**, *41* (29), 6225–6235.

(31) Miñambres, L.; Méndez, E.; Sánchez, M. N.; Castaño, F.; Basterretxea, F. J. Water uptake of internally mixed ammonium sulfate and dicarboxylic acid particles probed by infrared spectroscopy. *Atmos. Environ.* **2013**, *70*, 108–116.

(32) Zeng, G.; Kelley, J.; Kish, J. D.; Liu, Y. Temperature-dependent deliquescent and efflorescent properties of methanesulfonate sodium studied by ATR-FTIR spectroscopy. *J. Phys. Chem. A* **2014**, *118* (3), 583–591.

(33) Vartiainen, M.; McDow, S. R.; Kamens, R. M. Water uptake by aerosol particles from automobile exhaust and wood smoke. *Chemosphere* **1994**, *29* (8), 1661–1669.

(34) Kreisberg, N. M.; Stolzenburg, M. R.; Hering, S. V.; Dick, W. D.; McMurry, P. H. A new method for measuring the dependence of particle size distributions on relative humidity, with application to the Southeastern Aerosol and Visibility Study. *J. Geophys. Res.* **2001**, *106* (D14), 14935.

(35) Gupta, D.; Kim, H.; Park, G.; Li, X.; Eom, H.-J.; Ro, C.-U. Hygroscopic properties of NaCl and $NaNO_3$ mixture particles as reacted inorganic sea-salt aerosol surrogates. *Atmos. Chem. Phys.* **2015**, *15* (1), 3379–3393.

(36) Li, X.; Gupta, D.; Eom, H. J.; Kim, H.; Ro, C. U. Deliquescence and efflorescence behavior of individual NaCl and KCl mixture aerosol particles. *Atmos. Environ.* **2014**, *82*, 36–43.

(37) Ling, T. Y.; Chan, C. K. Partial crystallization and deliquescence of particles containing ammonium sulfate and dicarboxylic acids. *J. Geophys. Res.* **2008**, *113* (D14).

(38) Tang, I. N. Thermodynamic and optical properties of mixed-salt aerosols of atmospheric importance. *J. Geophys. Res.* **1997**, *102* (96), 1883–1893.

(39) Tang, I. N.; Munkelwitz, R. Composition and temperature dependence of the deliquescence properties of hygroscopi aerosols. *Atmos. Environ.* **1993**, *27* (4), 467–473.

(40) Martin, S. T. Phase Transitions of Aqueous Atmospheric Particles. *Chem. Rev.* **2000**, *100* (9), 3403–3454.

(41) Martin, S. T.; Han, J.-H.; Hung, H.-M. The size effect of hematite and corundum inclusions on the efflorescence relative humidities of aqueous ammonium sulfate particles. *Geophys. Res. Lett.* **2001**, *28* (13), 2601–2604.

(42) Davis, R. D.; Lance, S.; Gordon, J. A.; Ushijima, S. B.; Tolbert, M. A. Contact efflorescence as a pathway for crystallization of atmospherically relevant particles. *Proc. Natl. Acad. Sci.* **2015**, No. 3, 201522860.

(43) Wexler, A. S.; Seinfeld, J. H. Second-generation inorganic aerosol model. *Atmos. Environ.* **1991**, *25* (12), 2731–2748.

(44) Cziczo, D. J.; Abbatt, J. P. D. Infrared Observations of the Response of NaCl, MgCl2, NH4HSO4, and NH4NO3 Aerosols to Changes in Relative Humidity from 298 to 238 K. *J. Phys. Chem. A* **2000**, *104* (10), 2038–2047.

(45) Xu, J.; Imre, D.; Mcgraw, R.; Tang, I. Ammonium Sulfate : Equilibrium and Metastability Phase Diagrams from 40 to - 50 ° C. **1998**, *5647* (98), 7462–7469.

(46) Onasch, T. B.; McGraw, R.; Imre, D. Temperature-Dependent Heterogeneous Efflorescence of Mixed Ammonium Sulfate/Calcium Carbonate Particles. *J. Phys. Chem. A* **2000**, *104*, 10797–10806.

(47) Martin, S. T.; Schlenker, J. C.; Malinowski, A.; Hung, H.-M. Crystallization of atmospheric sulfate-nitrate-ammonium particles. *Geophys. Res. Lett.* **2003**, *30* (21), 2102.

(48) Clegg, S. L.; Pitzer, K. S.; Brimblecombe, P. Thermodynamics of Multicomponent, Mlsclble, Ionlc Solutions. 2. Mlxtures Including Unsymmetrical Electrolytes. *J. Phys. Chem.* **1992**, *96* (23), 9470–9479.

(49) Clegg, S. L.; Brimblecombe, P.; Wexler, A. S. Thermodynamic Model of the System H+ - NH4+ - Na+ - SO42- - NO3- - Cl- - H2O at 298.15 K. *J. Phys. Chem. A* **1998**, *5639* (3), 2155–2171.

(50) Nenes, A. ISORROPIA : A New Thermodynamic Equilibrium Model for Multiphase Multicomponent Inorganic Aerosols. *Aquat. Geochemistry* **1998**, *4*, 123–152.

(51) Fountoukis, C.; Nenes, A. ISORROPIA II : a computationally efficient thermodynamic equilibrium model for. *Atmos. Chem. Phys.* **2007**, 4639–4659.

(52) Hu, D.; Chen, J.; Ye, X.; Li, L.; Yang, X. Hygroscopicity and evaporation of ammonium chloride and ammonium nitrate: Relative humidity and size effects on the growth factor. *Atmos. Environ.* **2011**, *45* (14), 2349–2355.

(53) Lightstone, J. M.; Onasch, T. B.; Imre, D.; Oatis, S. Deliquescence, Efflorescence, and Water Activity in Ammonium Nitrate and Mixed Ammonium Nitrate/Succinic Acid Microparticles. *J. Phys. Chem. A* **2000**, *104* (41), 9337–9346.

(54) Choi, M. Y.; Chan, C. K. The effects of organic species on the hygroscopic behaviors of inorganic aerosols. *Environ. Sci. Technol.* **2002**, *36* (11), 2422–2428.

(55) Sjogren, S.; Gysel, M.; Weingartner, E.; Baltensperger, U.; Cubison, M. J.; Coe, H.; Zardini, a. a.; Marcolli, C.; Krieger, U. K.; Peter, T. Hygroscopic growth and water uptake kinetics of two-phase aerosol particles consisting of ammonium sulfate, adipic and humic acid mixtures. *J. Aerosol Sci.* **2007**, *38* (2), 157–171.

(56) Onasch, T. B.; Siefert, R. L.; Brooks, D.; Prenni, J.; Wilson, M. A.; Tolbert, M. A. Infrared spectroscopic study of the deliquescence and efflorescence of ammonium sulfate aersol as a function of temperature. **1999**, *104*.

(57) Yang, L.; Pabalan, R. T.; Juckett, M. R. Deliquescence Relative Humidity Measurements Using an Electrical Conductivity Method. *J. Solution Chem.* **2006**, *35* (4), 583–604.

(58) Schindelholz, E.; Tsui, L.-K.; Kelly, R. G. Hygroscopic Particle Behavior Studied by Interdigitated Array Microelectrode Impedance Sensors. *J. Phys. Chem. A* **2014**, *118*, 167–177.

(59) Verdingovas, V.; Jellesen, M. S.; Ambat, R. Impact of NaCl Contamination and Climatic Conditions on the Reliability of Printed Circuit Board Assemblies. *IEEE Trans. Device Mater. Reliab.* **2014**, *14* (1), 42–51.

(60) Verdingovas, V.; Jellesen, M. S.; Ambat, R. Solder Flux Residues and Humidity-Related Failures in Electronics: Relative Effects of Weak Organic Acids Used in No-Clean Flux Systems. *J. Electron. Mater.* **2015**, *44* (4), 1116–1127.

(61) Song, B.; Azarian, M. H.; Pecht, M. G. Effect of Temperature and Relative Humidity on the Impedance Degradation of Dust-Contaminated Electronics. *J. Electrochem. Soc.* **2013**, *160* (3), C97–C105.

(62) Miñambres, L.; Méndez, E.; Sánchez, M. N.; Castaño, F.; Basterretxea, F. J. Water uptake properties of internally mixed sodium halide and succinic acid particles. *Atmos. Environ.* **2011**, *45* (32), 5896–5902.

(63) Dennis-Smither, B. J.; Hanford, K. L.; Kwamena, N.-O. a; Miles, R. E. H.; Reid, J. P. Phase, morphology, and hygroscopicity of mixed oleic acid/sodium chloride/water aerosol particles before and after ozonolysis. *J. Phys. Chem. A* **2012**, *116* (24), 6159–6168.

(64) Gupta, D.; Kim, H.; Park, G.; Li, X.; Eom, H.-J.; Ro, C.-U. Hygroscopic properties of NaCl and $NaNO_3$ mixture particles as reacted inorganic sea-salt aerosol surrogates. *Atmos. Chem. Phys. Discuss.* **2014**, *14* (23), 33143–33183.

(65) Duplissy, J.; DeCarlo, P. F.; Dommen, J.; Alfarra, M. R.; Metzger, a.; Barmpadimos, I.; Prevot, a. S. H.; Weingartner, E.; Tritscher, T.; Gysel, M.; et al. Relating hygroscopicity and composition of organic aerosol particulate matter. *Atmos. Chem. Phys.* **2011**, *11* (3), 1155–1165.

(66) Tritscher, T.; Dommen, J.; DeCarlo, P. F.; Gysel, M.; Barmet, P. B.; Praplan, a. P.; Weingartner, E.; Prévôt, a. S. H.; Riipinen, I.; Donahue, N. M.; et al. Volatility and hygroscopicity of aging secondary organic aerosol in a smog chamber. *Atmos. Chem. Phys.* **2011**, *11* (22), 11477–11496.

(67) Smith, M. L.; Bertram, a. K.; Martin, S. T. Deliquescence, efflorescence, and phase miscibility of mixed particles of ammonium sulfate and isoprene-derived secondary organic material. *Atmos. Chem. Phys.* **2012**, *12* (20), 9613–9628.

(68) Cruz, C. N.; Pandis, S. N. Deliquescence and Hygroscopic Growth of Mixed Inorganic−Organic Atmospheric Aerosol. *Environ. Sci. Technol.* **2000**, *34* (20), 4313–4319.

(69) Ten Brink, H. M.; Veefkind, J. P.; Waijers-Ijpelaan, A.; Van Der Hage, J. C. Aerosol light-scattering in the Netherlands. *Atmos. Environ.* **1996**, *30* (24), 4251–4261.

(70) Rood, M. J.; Shaw, M. A.; Larson, T. V.; Covert, D. S. Ubiquitous nature of ambient metastable aerosol. *Nature* **1989**.

(71) Santarpia, J. L.; Li, R.; Collins, D. R. Direct measurement of the hydration state of ambient aerosol populations. *J. Geophys. Res. Atmos.* **2004**, *109*, 1–16.

(72) Martin, S. T.; Rosenoern, T.; Chen, Q.; Collins, D. R. Phase changes of ambient particles in the Southern Great Plains of Oklahoma. *Geophys. Res. Lett.* **2008**, *35* (22), L22801.

(73) Taylor, N. F.; Collins, D. R.; Spencer, C. W.; Lowenthal, D. H.; Zielinska, B.; Samburova, V.; Kumar, N. Measurement of ambient aerosol hydration state at Great Smoky Mountains National Park in the southeastern United States. *Atmos. Chem. Phys.* **2011**, *11* (23), 12085–12107.

(74) D'Angelo, L.; Rovelli, G.; Casati, M.; Sangiorgi, G.; Perrone, M. G.; Bolzacchini, E.; Ferrero, L. Seasonal behavior of PM 2.5 deliquescence, crystallization and hygroscopic growth in the Po Valley (Milan): implications for remote sensing applications. *Atmos. Res. (submitted*.

(75) Casati, M.; Rovelli, G.; D'Angelo, L.; Perrone, M. G.; Sangiorgi, G.; Bolzacchini, E.; Ferrero, L. Experimental Measurements of Particulate Matter Deliquescence and Crystallization Relative Humidity: Application in Heritage Climatology. *Aerosol Air Qual. Res.* **2015**, 1–11.

(76) Ferrero, L.; D'Angelo, L.; Rovelli, G.; Sangiorgi, G.; Perrone, M. G.; Moscatelli, M.; Casati, M.; Rozzoni, V.; Bolzacchini, E. Determination of aerosol deliquescence and crystallization relative humidity for energy saving in free-cooled data centers. *Int. J. Environ. Sci. Technol.* **2015**, *12* (9), 2777–2790.

(77) Rodriguez, S.; Van Dingenen, R.; Putaud, J. P.; Dell'Acqua, A.; Pey, J.; Querol, X.; Alastuey, A.; Chenery, S.; Ho, K.-F.; Harrison, R.; et al. A study on the relationship between mass concentrations, chemistry and number size distribution of urban fine aerosols in Milan, Barcelona and London. *Atmos. Chem. Phys.* **2007**, 2217–2232.

(78) Ferrero, L.; Castelli, M.; Ferrini, B. S.; Moscatelli, M.; Perrone, M. G.; Sangiorgi, G.; D'Angelo, L.; Rovelli, G.; Moroni, B.; Scardazza, F.; et al. Impact of black carbon aerosol over Italian basin valleys: high-resolution measurements along vertical profiles, radiative forcing and heating rate. *Atmos. Chem. Phys.* **2014**, *14* (18), 9641–9664.

(79) Ferrero, L.; Riccio, a.; Perrone, M. G.; Sangiorgi, G.; Ferrini, B. S.; Bolzacchini, E. Mixing height determination by tethered balloon-based particle soundings and modeling simulations. *Atmos. Res.* **2011**, *102* (1-2), 145–156.

(80) Owoade, O. K.; Olise, F. S.; Obioh, I. B.; Olaniyi, H. B.; Bolzacchini, E.; Ferrero, L.; Perrone, G. PM10

sampler deposited air particulates: Ascertaining uniformity of sample on filter through rotated exposure to radiation. *Nucl. Instruments Methods Phys. Res. Sect. A Accel. Spectrometers, Detect. Assoc. Equip.* **2006**, *564*, 315–318.

(81) Arenas, K. J. L.; Schill, S. R.; Malla, A.; Hudson, P. K. Deliquescence phase transition measurements by quartz crystal microbalance frequency shifts. *J. Phys. Chem. A* **2012**, *116* (29), 7658–7667.

(82) Gilardoni, S.; Massoli, P.; Giulianelli, L.; Rinaldi, M.; Paglione, M.; Pollini, F.; Lanconelli, C.; Poluzzi, V.; Carbone, S.; Hillamo, R.; et al. Fog scavenging of organic and inorganic aerosol in the po valley. *Atmos. Chem. Phys.* **2014**, *14*, 6967–6981.

(83) Weschler, C. J. Predictions of benefits and costs derived from improving indoor air quality in telephone switching offices. *Indoor Air* **1991**, *78* (May 1990), 65~78.

(84) Hoshen, J. and Kopelman, R. Percolation and cluster distribution. I. Cluster multiple labeling techinique and critical concentration algorithm. *Phys. Rev. B* **1976**, *14* (8).

(85) Hoshen, J.; Kopelman, R.; Monberg, E. M. Percolation and cluster distribution. II. layers, variable-range interactions, and exciton cluster model. *J. Stat. Phys.* **1978**, *19* (3), 219–242.

(86) Tencer, M. Deposition of aerosol ("hygroscopic dust") on electronics – Mechanism and risk. *Microelectron. Reliab.* **2008**, *48* (4), 584–593.

(87) Awakuni, Y.; Calderwood, J. H. Water vapour adsorption and surface conductivity in solids. **1972**, *1038*.

(88) Anderko, A.; Lencka, M. M. Computation of Electrical Conductivity of Multicomponent Aqueous Systems in Wide Concentration and Temperature Ranges. *Ind. Eng. Chem. Res.* **1997**, *36* (5), 1932–1943.

(89) Gregor, H. P.; Robinson, R. A.; Stokes., R. H. *Electrolyte solutions*, Second Rev.; Dover Publications, I., Ed.; Wiley Subscription Services, Inc., A Wiley Company, 1960; Vol. 3.

(90) Lu, J. W.; Rickards, A. M. J.; Walker, J. S.; Knox, K. J.; Miles, R. E. H.; Reid, J. P.; Signorell, R. Timescales of water transport in viscous aerosol: measurements on sub-micron particles and dependence on conditioning history. *Phys. Chem. Chem. Phys.* **2014**, *16* (21), 9819–9830.

(91) Shiraiwa, M.; Zuend, A.; Bertram, A. K.; Seinfeld, J. H. Gas-particle partitioning of atmospheric aerosols: interplay of physical state, non-ideal mixing and morphology. *Phys. Chem. Chem. Phys.* **2013**, *15* (27), 11441–11453.

(92) Mikhailov, E.; Vlasenko, S.; Rose, D.; Pöschl, U. Mass-based hygroscopicity parameter interaction model and measurement of atmospheric aerosol water uptake. *Atmos. Chem. Phys.* **2013**, *13* (2), 717–740.

(93) Mikhailov, E.; Vlasenko, S.; Martin, S. T.; Koop, T.; Pöschl, U. Amorphous and crystalline aerosol particles interacting with water vapor: conceptual framework and experimental evidence for restructuring, phase transitions and kinetic limitations. *Atmos. Chem. Phys.* **2009**, *9* (24), 9491–9522.

(94) Tong, H.-J.; Reid, J. P.; Bones, D. L.; Luo, B. P.; Krieger, U. K. Measurements of the timescales for the mass transfer of water in glassy aerosol at low relative humidity and ambient temperature. *Atmos. Chem. Phys.* **2011**, *11* (10), 4739–4754.

(95) Hodas, N.; Zuend, A.; Mui, W.; Flagan, R. C.; Seinfeld, J. H. Influence of particle-phase state on the hygroscopic behavior of mixed organic–inorganic aerosols. *Atmos. Chem. Phys.* **2015**, *15* (9), 5027–5045.

(96) Bialek, J.; Dall Osto, M.; Vaattovaara, P.; Decesari, S.; Ovadnevaite, J.; Laaksonen, a.; O'Dowd, C. Hygroscopic and chemical characterisation of Po Valley aerosol. *Atmos. Chem. Phys.* **2014**, *14* (3), 1557–1570.

(97) Perrino, C.; Catrambone, M.; Dalla Torre, S.; Rantica, E.; Sargolini, T.; Canepari, S. Seasonal variations in the chemical composition of particulate matter: a case study in the Po Valley. Part I: macro-components and mass closure. *Environ. Sci. Pollut. Res. Int.* **2013**, *21* (6), 3999–4009.

(98) Squizzato, S.; Masiol, M.; Brunelli, A.; Pistollato, S.; Tarabotti, E.; Rampazzo, G.; Pavoni, B. Factors determining the formation of secondary inorganic aerosol: a case study in the Po Valley (Italy). *Atmos. Chem. Phys.* **2013**, *13* (4), 1927–1939.

(99) Du, H. Insights into Ammonium Particle-to-Gas Conversion: Non-sulfate Ammonium Coupling with Nitrate and Chloride. *Aerosol Air Qual. Res.* **2010**, No. 1, 589–595.

(100) Mozurkewich, M. The dissociation constant of ammonium nitrate and its dependence on temperature, relative humidity and particle size. *Atmos. Environ. Part A. Gen. Top.* **1993**, *27* (2), 261–270.

(101) Stelson, A. W.; Seinfeld, J. H. Relative humidity and temperature dependence of the ammonium nitrate dissociation constant. *Atmos. Environ.* **1982**, *16* (5), 983–992.

(102) Khlystov, A.; Stanier, C. O.; Takahama, S.; Pandis, S. N. Water content of ambient aerosol during the Pittsburgh air quality study. *J. Geophys. Res. Atmos.* **2005**, *110*, 1–10.

(103) Jimenez, J. L.; Canagaratna, M. R.; Donahue, N. M.; Prevot, a S. H.; Zhang, Q.; Kroll, J. H.; DeCarlo, P. F.; Allan, J. D.; Coe, H.; Ng, N. L.; et al. Evolution of organic aerosols in the atmosphere. *Science* **2009**, *326* (5959), 1525–1529.

(104) Chan, L. P.; Lee, A. K. Y.; Chan, C. K. Gas-particle partitioning of alcohol vapors on organic aerosols. *Environ. Sci. Technol.* **2010**, *44* (1), 257–262.

(105) Richardson, C. B.; Hightower, R. L. Evaporation of ammonium nitrate particles. *Atmos. Environ.* **1987**, *21* (4), 971–975.

(106) Potukuchi, S.; Wexler, A. S. Identifying solid-aqueous-phase transitions in atmospheric aerosols. II. Acidic solutions. *Atmos. Environ.* **1995**, *29* (22), 3357–3364.

(107) Han, J.; Martin, S. Heterogeneous nucleation of the efflorescence of (NH4) 2SO4 particles internally mixed with Al2O3, TiO2, and ZrO2. *J. Geophys. Res.* **1999**, *104* (D3), 3543–3553.

(108) Vecchi, R.; Marcazzan, G.; Valli, G.; Ceriani, M.; Antoniazzi, C. The role of atmospheric dispersion in the seasonal variation of PM1 and PM2.5 concentration and composition in the urban area of Milan (Italy). *Atmos. Environ.* **2004**, *38* (27), 4437–4446.

(109) Decesari, S.; Facchini, M. C.; Matta, E.; Lettini, F.; Mircea, M.; Fuzzi, S.; Tagliavini, E.; Putaud, J. P. Chemical features and seasonal variation of fine aerosol water-soluble organic compounds in the Po Valley, Italy. *Atmos. Environ.* **2001**, *35* (21), 3691–3699.

(110) Saxena, P.; Hildemann, L. M. Water-soluble organics in atmospheric particles: A critical review of the literature and application of thermodynamics to identify candidate compounds. *J. Atmos. Chem.* **1996**, *24* (1), 57–109.

(111) Varutbangkul, V.; Brechtel, F. J.; Bahreini, R.; Ng, N. L.; Keywood, M. D.; Kroll, J. H.; Flagan, R. C.; Seinfeld, J. H.; Lee, a.; Goldstein, a. H. Hygroscopicity of secondary organic aerosols formed by oxidation of cycloalkenes, monoterpenes, sesquiterpenes, and related compounds. *Atmos. Chem. Phys. Discuss.* **2006**, *6* (1), 1121–1177.

(112) Virkkula, A.; Van Dingenen, R.; Raes, F.; Hjorth, J. Hygroscopic properties of aerosol formed by oxidation of limonene, α-pinene, and β-pinene. *J. Geophys. Res. Atmos.* **1999**, *104* (D3), 3569–3579.

(113) McMurry, P. H.; Stolzenburg, M. R. On the sensitivity of particle size to relative humidity for Los Angeles aerosols. *Atmos. Environ.* **1989**, *23* (2), 497–507.

(114) Martin, S. T.; Hung, H.-M.; Park, R. J.; Jacob, D. J.; Spurr, R. J. D.; Chance, K. V.; Chin, M. Effects of the physical state of tropospheric ammonium-sulfate-nitrate particles on global aerosol direct radiative forcing. *Atmos. Chem. Phys.* **2004**, *4* (1), 183–214.

(115) Ansari, A. S.; Pandis, S. N. The effect of metastable equilibrium states on the partitioning of nitrate between the gas and aerosol phases. *Atmos. Environ.* **2000**, *34*, 157–168.

(116) Rood, M. J.; Covert, D. S.; Larson, T. V. Hygroscopic properties of atmospheric aerosol in Riverside, California. *Tellus B* **1987**, *39*, 383–397.

(117) Schindelholz, E.; Kelly, R. G. Wetting phenomena and time of wetness in atmospheric corrosion: a review. *Corros. Rev.* **2012**, *30* (5-6), 135–170.

(118) Cole, I. S.; Holgate, R.; Kao, P.; Ganther, W. The rate of drying of moisture from a metal surface and its implication for time of wetness. *Corros. Sci.* **1995**, *37* (3), 455–465.

(119) Hienonen, R.; Lahtinen, R. *Corrosion and climatic effects in electronics*; 2007.

(120) EL-Mahdy, G. a. Electrochemical impedance study on brass corrosion in NaCl and (NH4)2SO4 solutions during cyclic wet?dry conditions. *J. Appl. Electrochem.* **2005**, *35* (3), 347–353.

(121) Brimblecombe, P.; Grossi, C. M.; Harris, I. The effect of long-term trends in dampness on historic buildings. *Weather* **2006**, *61* (10), 278–281.

(122) Tidblad, J.; Kucera, V.; Ferm, M.; Kreislova, K.; Brüggerhoff, S.; Doytchinov, S.; Screpanti, A.; Grøntoft, T.; Yates, T.; de la Fuente, D.; et al. Effects of Air Pollution on Materials and Cultural Heritage: ICP

Materials Celebrates 25 Years of Research. *Int. J. Corros.* **2012**, *2012*, 1–16.

(123) Oesch, S.; Faller, M. ENVIRONMENTAL EFFECTS ON MATERIALS : THE EFFECT OF THE AIR POLLUTANTS SOS , NOz , NO AND O3 ON THE CORROSION OF COPPER , ZINC AND ALUMINIUM . A SHORT LITERATURE SURVEY AND RESULTS OF LABORATORY EXPOSURES. **1997**, No. March 1996.

(124) Fonseca, I. T. .; Picciochi, R.; Mendonça, M. .; Ramos, a. . The atmospheric corrosion of copper at two sites in Portugal: a comparative study. *Corros. Sci.* **2004**, *46* (3), 547–561.

(125) Cardell-Fernández, C.; Vleugels, G.; Torfs, K.; Van Grieken, R. The processes dominating Ca dissolution of limestone when exposed to ambient atmospheric conditions as determined by comparing dissolution models. *Environ. Geol.* **2002**, *43* (1-2), 160–171.

(126) Forslund, M.; Leygraf, C. Humidity sorption due to deposited aerosol particles studied in situ outdoors on gold surfaces. *J. Electrochem. Soc.* **1997**, *144* (1), 105–113.

(127) Chu, D. A.; Tsai, T.-C.; Chen, J.-P.; Chang, S.-C.; Jeng, Y.-J.; Chiang, W.-L.; Lin, N.-H. Interpreting aerosol lidar profiles to better estimate surface PM2.5 for columnar AOD measurements. *Atmos. Environ.* **2013**, *79*, 172–187.

(128) Randriamiarisoa, H.; Chazette, P.; Couvert, P.; Sanak, J. Relative humidity impact on aerosol parameters in a Paris suburban area. *Atmos. Chem. Phys.* **2006**, No. 1999, 1389–1407.

(129) Cole, I. S.; Ganther, W. D.; Sinclair, J. D.; Lau, D.; Paterson, D. a. A Study of the Wetting of Metal Surfaces in Order to Understand the Processes Controlling Atmospheric Corrosion. *J. Electrochem. Soc.* **2004**, *151* (12), B627.

(130) Veleva, L.; Perez, G.; Acosta, M. SHORT COMMUNICATION STATISTICAL ANALYSIS OF THE TEMPERATURE-HUMIDITY COMPLEX AND TIME OF WETNESS OF A TROPICAL CLIMATE IN THE YUCATAN PENINSULA IN MEXICO. **1997**, *31* (5).

(131) Swietlicki, E.; Hansson, H.-C.; Hämeri, K.; Svenningsson, B.; Massling, A.; Mcfiggans, G.; Mcmurry, P. H.; Petäjä, T.; Tunved, P.; Gysel, M.; et al. Hygroscopic properties of submicrometer atmospheric aerosol particles measured with H-TDMA instruments in various environments—a review. *Tellus B* **2008**.

(132) Kamilli, K. a.; Poulain, L.; Held, a.; Nowak, a.; Birmili, W.; Wiedensohler, a. Hygroscopic properties of the Paris urban aerosol in relation to its chemical composition. *Atmos. Chem. Phys.* **2014**, *14*, 737–749.

(133) Svenningsson, I. B.; Hansson, H.-C.; Wiedensohler, A. Higroscopicity in the Po Valley. *Tellus* **1992**, *44 B* (5), 556–569.

(134) Wang, J.; Hoffmann, A. a.; Park, R. J.; Jacob, D. J.; Martin, S. T. Global distribution of solid and aqueous sulfate aerosols: Effect of the hysteresis of particle phase transitions. *J. Geophys. Res.* **2008**, *113* (D11), D11206.

(135) Wang, J.; Jacob, D. J.; Martin, S. T. Sensitivity of sulfate direct climate forcing to the hysteresis of particle phase transitions. *J. Geophys. Res.* **2008**, *113* (D11), D11207.

(136) Levy, R. C.; Remer, L. a.; Dubovik, O. Global aerosol optical properties and application to Moderate Resolution Imaging Spectroradiometer aerosol retrieval over land. *J. Geophys. Res. Atmos.* **2007**, *112* (D13), n/a – n/a.

(137) Barnaba, F.; Putaud, J. P.; Gruening, C.; dell'Acqua, a.; Dos Santos, S. Annual cycle in co-located in situ, total-column, and height-resolved aerosol observations in the Po Valley (Italy): Implications for ground-level particulate matter mass concentration estimation from remote sensing. *J. Geophys. Res.* **2010**, *115* (D19), D19209.

(138) Hoff, R.; Christopher, S. Remote Sensing of Particulate Pollution from Space: Have We Reached the Promised Land? *J. Air Waste Manage. Assoc.* **2009**, *59* (6), 645–675.

(139) Ferm, M.; Watt, J.; O'Hanlon, S.; De Santis, F.; Varotsos, C. Deposition measurement of particulate matter in connection with corrosion studies. *Anal. Bioanal. Chem.* **2006**, *384* (6), 1320–1330.

(140) Grossi, C. .; Esbert, R. .; Díaz-Pache, F.; Alonso, F. . Soiling of building stones in urban environments. *Build. Environ.* **2003**, *38* (1), 147–159.

(141) Camuffo, D.; Del Monte, M.; Sabbioni, C.; Vittori, O. Wetting, deterioration and visual features of stone surfaces in an urban area. *Atmos. Environ.* **1982**, *16* (9), 2253–2259.

(142) Kucera, V.; Tidblad, J.; Kreislova, K.; Knotkova, D.; Faller, M.; Reiss, D.; Snethlage, R.; Yates, T.;

Henriksen, J.; Schreiner, M.; et al. UN/ECE ICP Materials Dose-response Functions for the Multi-pollutant Situation. *Water, Air, Soil Pollut. Focus* **2007**, *7* (1-3), 249–258.

(143) Ghedini, N.; Ozga, I.; Bonazza, a.; Dilillo, M.; Cachier, H.; Sabbioni, C. Atmospheric aerosol monitoring as a strategy for the preventive conservation of urban monumental heritage: The Florence Baptistery. *Atmos. Environ.* **2011**, *45* (33), 5979–5987.

(144) Urosevic, M.; Yebra-Rodríguez, A.; Sebastián-Pardo, E.; Cardell, C. Black soiling of an architectural limestone during two-year term exposure to urban air in the city of Granada (S Spain). *Sci. Total Environ.* **2012**, *414*, 564–575.

(145) Bonazza, A.; Messina, P.; Sabbioni, C.; Grossi, C. M.; Brimblecombe, P. Mapping the impact of climate change on surface recession of carbonate buildings in Europe. *Sci. Total Environ.* **2009**, *407* (6), 2039–2050.

(146) Grossi, C. M.; Brimblecombe, P.; Menéndez, B.; Benavente, D.; Harris, I.; Déqué, M. Climatology of salt transitions and implications for stone weathering. *Sci. Total Environ.* **2011**, *409* (13), 2577–2585.

(147) Grause, G.; Furusawa, M.; Okuwaki, A.; Yoshioka, T. Pyrolysis of tetrabromobisphenol-A containing paper laminated printed circuit boards. *Chemosphere* **2008**, *71* (5), 872–878.

(148) Barontini, F. An experimental investigation of tetrabromobisphenol A decomposition pathways. *J. Anal. Appl. Pyrolysis* **2004**, *72* (1), 41–53.

(149) Ferrero, L.; Sangiorgi, G.; Ferrini, B. S.; Perrone, M. G.; Moscatelli, M.; D'Angelo, L.; Rovelli, G.; Ariatta, A.; Truccolo, R.; Bolzacchini, E. Aerosol Corrosion Prevention and Energy-Saving Strategies in the Design of Green Data Centers. *Environ. Sci. Technol.* **2013**.

(150) Shehabi, A.; Horvath, A.; Tschudi, W.; Gadgil, A. J.; Nazaroff, W. W. Particle concentrations in data centers. *Atmos. Environ.* **2008**, *42* (24), 5978–5990.

(151) Litvak, a; Gadgil, a J.; Fisk, W. J. Hygroscopic fine mode particle deposition on electronic circuits and resulting degradation of circuit performance: an experimental study. *Indoor Air* **2000**, *10* (1), 47–56.

(152) Li, D.; Conway, P. P.; Liu, C. Corrosion characterization of tin-lead and lead free solders in 3.5 wt.% NaCl solution. *Corros. Sci.* **2008**, *50*, 995–1004.

(153) Takemoto, T.; Latanision, R. M.; Eagar, T. W.; Matsunawa, A. Electrochemical migration tests of solder alloys in pure water. *Corros. Sci.* **1997**, *39* (8), 1415–1430.

(154) Zhong, X.; Zhang, G.; Qiu, Y.; Chen, Z.; Guo, X.; Fu, C. The corrosion of tin under thin electrolyte layers containing chloride. *Corros. Sci.* **2013**, *66*, 14–25.

(155) Zhong, X.; Zhang, G.; Qiu, Y.; Chen, Z.; Guo, X. Electrochemical migration of tin in thin electrolyte layer containing chloride ions. *Corros. Sci.* **2013**, *74*, 71–82.

(156) Ammar, I. A.; Darwish, S.; Khalil, M. W.; Galal, A. Electrochemical Polarization and Passivation of Tin in neutral solutions of chloride, bromide and iodide ions. *Materwiss. Werksttech.* **1982**, *13* (11), 376–385.

(157) Trompette, J. L. The comparative breakdown of passivity of tin by fluorides and chlorides interpreted through the "law of matching affinities" concept. *Corros. Sci.* **2015**, *94*, 288–293.

(158) Noh, B. I.; Lee, J. B.; Jung, S. B. Effect of surface finish material on printed circuit board for electrochemical migration. *Microelectron. Reliab.* **2008**, *48* (4), 652–656.

(159) Krumbein, S. Metallic Electromigration Phenomena. *IEEE Trans. components, hybridis, Manuf. Technol.* **1988**, *11* (1), 5–15.

(160) Minzari, D.; Jellesen, M. S.; Møller, P.; Ambat, R. On the electrochemical migration mechanism of tin in electronics. *Corros. Sci.* **2011**, *53* (10), 3366–3379.

(161) Sherlock, J. C.; Britton, S. C. PROMOTION BY NITRATES OF THE DISSOLUTION OF TIN BY ACIDS AND ITS INHIBITION. *British Corrosion Journal*. 1973, pp 210–215.

(162) Warren, G. W.; Wynblatt, P.; Zamanzadeh, M. The role of electrochemical migration and moisture adsorption on the reliability of metallized ceramic substrates. *J. Electron. Mater.* **1989**, *18* (2), 339–353.

(163) Frankenthal, R. P.; Lobnig, R.; Siconolfi, D. J.; Sinclair, J. D. Role of particle contamination in the corrosion of electronic materials and devices. *J. Vac. Sci. Technol. A* **1993**, *11* (4), 2274.

(164) Schimpf, C.; Feldmann, K.; Matzner, C.; Steinke, a. Failure of electronic devices due to condensation. *Microsyst. Technol.* **2009**, *15* (1), 123–127.

(165) Canepari, S.; Astolfi, M. L.; Farao, C.; Maretto, M.; Frasca, D.; Marcoccia, M.; Perrino, C. Seasonal

variations in the chemical composition of particulate matter: a case study in the Po Valley. Part II: concentration and solubility of micro- and trace-elements. *Environ. Sci. Pollut. Res. Int.* **2013**.

(166) Crosier, J.; Allan, J. D.; Coe, H.; Bower, K. N.; Formenti, P.; Williams, P. I. Chemical composition of summertime aerosol in the Po Valley (Italy), northern Adriatic and Black Sea. *Q. J. R. Meteorol. Soc.* **2007**, *133* (S1), 61–75.

(167) Decesari, S.; Allan, J.; Williams, B. J.; Paglione, M.; Facchini, M. C.; Dowd, C. O. Measurements of the aerosol chemical composition and mixing state in the Po Valley using multiple spectroscopic techniques. **2014**, 12109–12132.

(168) Fermo, P.; Piazzalunga, A.; Vecchi, R.; Valli, G.; Ceriani, M. Secondary aerosol components contribution in PM10, PM2.5 and PM1: Results of a wintertime monitoring campaign in Milan (Italy). In *Journal of Aerosol Science*; 2004; Vol. 35.

(169) Minzari, D.; Jellesen, M. S.; Moller, P.; Wahlberg, P.; Ambat, R. Electrochemical migration on electronic chip resistors in chloride environments. *IEEE Trans. Device Mater. Reliab.* **2009**, *9* (3), 392–402.

(170) Ambat, R.; Møller, P. Corrosion investigation of material combinations in a mobile phone dome–key pad system. *Corros. Sci.* **2007**, *49* (7), 2866–2879.

(171) Morawska, L.; Jamriska, M.; Guo, H.; Jayaratne, E. R.; Cao, M.; Summerville, S. Variation in indoor particle number and PM2.5 concentrations in a radio station surrounded by busy roads before and after an upgrade of the HVAC system. *Build. Environ.* **2009**, *44* (1), 76–84.

(172) Pitz, M.; Cyrys, J.; Karg, E.; Wiedensohler, A.; Wichmann, H. E.; Heinrich, J. Variability of apparent particle density of an urban aerosol. *Environ. Sci. Technol.* **2003**, *37* (19), 4336–4342.

(173) Karg, E. The density of ambient particles from combined DMA and APS data. *J. Aerosol Sci.* **2000**, *31* (SUPPL.1).

(174) Hänel, G.; Thudium, J. Mean bulk densities of samples of dry atmospheric aerosol particles: A summary of measured data. *Pure Appl. Geophys. PAGEOPH* **1977**, *115* (4), 799–803.

(175) McMurry, P. H.; Wang, X.; Park, K.; Ehara, K. The Relationship between Mass and Mobility for Atmospheric Particles: A New Technique for Measuring Particle Density. *Aerosol Sci. Technol.* **2002**, *36* (2), 227–238.

(176) Gao, Y.; Chen, S. B.; Yu, L. E. Efflorescence relative humidity of airborne sodium chloride particles: A theoretical investigation. *Atmos. Environ.* **2007**, *41*, 2019–2023.

(177) Oatis, S.; Imre, D.; McGraw, R.; Xu, J. Heterogeneous nucleation of a common atmospheric aerosol: Ammonium sulfate. *Geophys. Res. Lett.* **1998**, *25* (24), 4469–4472.

(178) Muralidharan, S.; Kim, D.-K.; Ha, T.-H.; Bae, J.-H.; Ha, Y.-C.; Lee, H.-G.; Scantlebury, J. D. Influence of alternating, direct and superimposed alternating and direct current on the corrosion of mild steel in marine environments. *Desalination* **2007**, *216* (1-3), 103–115.

(179) Huang, H.; Pan, Z.; Guo, X.; Qiu, Y. Effect of an alternating electric field on the atmospheric corrosion behaviour of copper under a thin electrolyte layer. *Corros. Sci.* **2013**, *75*, 100–105.

(180) Kim, D.-K.; Muralidharan, S.; Ha, T.-H.; Bae, J.-H.; Ha, Y.-C.; Lee, H.-G.; Scantlebury, J. D. Electrochemical studies on the alternating current corrosion of mild steel under cathodic protection condition in marine environments. *Electrochim. Acta* **2006**, *51*, 5259–5267.

(181) Saltzman, E. S.; Savoie, D. L.; Zika, R. G.; Prospero, J. M. Methane sulfonic acid in the marine atmosphere. *J. Geophys. Res.* **1983**, *88* (C15), 10897–10902.

(182) Salma, I.; Ocskay, R.; Chi, X.; Maenhaut, W. Sampling artefacts, concentration and chemical composition of fine water-soluble organic carbon and humic-like substances in a continental urban atmospheric environment. *Atmos. Environ.* **2007**, *41* (19), 4106–4118.

(183) Sannigrahi, P.; Sullivan, A. P.; Weber, R. J.; Ingall, E. D. Characterization of water-soluble organic carbon in urban atmospheric aerosols using solid-state 13C NMR spectroscopy. *Environ. Sci. Technol.* **2006**, *40* (3), 666–672.

(184) Minzari, D.; Grumsen, F. B.; Jellesen, M. S.; Møller, P.; Ambat, R. Electrochemical migration of tin in electronics and microstructure of the dendrites. *Corros. Sci.* **2011**, *53* (5), 1659–1669.

(185) Verdingovas, V.; Jellesen, M. S.; Ambat, R. Influence of sodium chloride and weak organic acids (flux residues) on electrochemical migration of tin on surface mount chip components. *Corros. Eng. Sci. Technol.*

2013, *48* (6), 426–435.

(186) Wu, B. Y.; Chan, Y. C.; Alam, M. O. Electrochemical corrosion study of Pb-free solders. *J. Mater. ...* **2006**, *21* (1), 62–70.

(187) Farina, S.; Morando, C. Comparative corrosion behaviour of different Sn-based solder alloys. **2015**, 464–471.

(188) Verdingovas, V.; Jellesen, M. S.; Ambat, R. Effect of Ionic Contamination on Corrosion Reliability of Printed Circuit Board Assemblies. In *Eurocorr 2012*; 2012.

(189) Whitney, J.; Delforge, P. *Data Center Efficiency Assessment: Scaling Up Energy Efficiency Across the Data Center Industry : Evaluating Key Drivers and Barriers*; 2014.

(190) Greenpeace International. *Clicking Clean : How Companies are Creating the Green Internet*; 2014.

(191) Shehabi, A. Energy Demands and Efficiency Strategies in Data Center Buildings, Lawrence Berkeley National Laboratory, 2010.

(192) Oró, E.; Depoorter, V.; Pflugradt, N.; Salom, J. Overview of direct air free cooling and thermal energy storage potential energy savings in data centres. *Appl. Therm. Eng.* **2015**, *85*, 100–110.

(193) ASHRAE. *2011 Thermal Guidelines for Data Processing Environments – Expanded Data Center Classes and Usage Guidance*; 2011.

(194) ASHRAE. *Gaseous and Particulate Contamination Guidelines for Data Centers*; 2011.

(195) Nazaroff, W. W. Indoor particle dynamics. *Indoor Air, Suppl.* **2004**, *14* (SUPPL. 7), 175–183.

(196) Daher, N.; Ruprecht, A.; Invernizzi, G.; De Marco, C.; Miller-Schulze, J.; Heo, J. B.; Shafer, M. M.; Shelton, B. R.; Schauer, J. J.; Sioutas, C. Characterization, sources and redox activity of fine and coarse particulate matter in Milan, Italy. *Atmos. Environ.* **2012**, *49*, 130–141.

(197) Tzanis, C.; Varotsos, C.; Christodoulakis, J.; Tidblad, J.; Ferm, M.; Ionescu, a.; Lefevre, R. -a.; Theodorakopoulou, K.; Kreislova, K. On the corrosion and soiling effects on materials by air pollution in Athens, Greece. *Atmos. Chem. Phys.* **2011**, *11* (23), 12039–12048.

(198) Syed, S. Atmospheric corrosion of materials. *Emirates J. Eng. Res.* **2006**, *11* (1), 1–24.

(199) Knotkova, D.; Barton, K. Effects of acid deposizion on corrosion of metals. *Atmos. Environ.* **1992**, *26* (17), 3169–3177.

(200) Dogruoz, M. B.; Nagulapally, M. K. Effects of Trace Layers and Joule Heating on the Temperature Distribution of Printed Circuit Boards: A Computational Study. *J. Therm. Sci. Eng. Appl.* **2009**, *1* (2), 22003.

(201) Shankaran, G. V.; Dogruoz, M. B.; deAraujo, D. Orthotropic thermal conductivity and Joule heating effects on the temperature distribution of printed circuit boards. *2010 12th IEEE Intersoc. Conf. Therm. Thermomechanical Phenom. Electron. Syst.* **2010**, 1–9.